

Dissertation  
submitted to the  
Combined Faculties of the Natural Sciences and Mathematics  
of the Ruperto-Carola-University of Heidelberg, Germany  
for the degree of  
Doctor of Natural Sciences

Put forward by  
Dušan Budjáš  
from Bratislava  
Oral examination: 6.5.2009



**Germanium detector studies  
in the framework of the GERDA experiment**

Referees: Prof. Dr. Wolfgang Hampel  
Prof. Dr. Wolfgang Krätschmer



## Germanium-Detektor-Studien im Rahmen des GERDA-Experiments

Das "GERmanium Detector Array" (GERDA) ist ein Experiment mit extrem niedrigem Untergrund, das zur Zeit am "Laboratori Nazionali del Gran Sasso" aufgebaut wird. GERDA wird nach dem neutrinolosen Doppel-Beta-Zerfall von  $^{76}\text{Ge}$  suchen, mit dem Ziel die Untergrundeffekte um einen Faktor 100 gegenüber den Vorgänger-Experimenten zu unterdrücken. Dieses Bestreben macht innovative Design-Ansätze, strenge Auswahl an Materialien mit niedriger Eigenradioaktivität und neue Techniken zur aktiven Unterdrückung des Untergrundes notwendig. Das zentrale Element von GERDA ist ein Array mit  $^{76}\text{Ge}$ -angereicherte Germanium-Detektoren für ionisierende Strahlung. Germanium-Detektoren sind auch das zentrale Thema dieser Dissertation. Der erste Teil beschreibt die Implementierung, die Tests und die Optimierung der Monte Carlo-Simulationen von Germanium-Spektrometern, die für die Selektion von Materialien mit niedriger Eigenradioaktivität unabkömmlich sind. Die Simulationen sind wesentlich für die Auswertungen der Gamma-Strahlungs-Messungen. Der zweite Teil beschäftigt sich mit der Entwicklung und der Prüfung einer Methode zur aktiven Unterdrückung des Untergrundes, die auf einer Form-Analyse des Germanium-Detektor-Signals besteht. Dies wurde zum ersten Mal für einen Detektor des BEGe-Typs, der eine kleine Auslese-Elektrode beinhaltet, verwirklicht. Als Ergebnis dieser Arbeit ist BEGe nun als eine der beiden Detektor-Technologien in der Forschung und Entwicklung für die zweite Phase des GERDA-Experiments enthalten. Eine Unterdrückung des Hauptuntergrundes für GERDA wird aufgezeigt, mit einer  $(0.93 \pm 0.08)$ -prozentigen Überlebenswahrscheinlichkeit für  $^{60}\text{Co}$ -Ereignisse,  $(21 \pm 3)\%$  für  $^{226}\text{Ra}$  und  $(40 \pm 2)\%$  für  $^{228}\text{Th}$ . Die Akzeptanz von  $^{228}\text{Th}$  Doppel-Escape-Ereignissen, die analog zu Doppel-Beta-Zerfall sind, wurde auf  $(89,2 \pm 0,9)\%$  gehalten.

## Germanium detector studies in the framework of the GERDA experiment

The GERmanium Detector Array (GERDA) is an ultra-low background experiment under construction at Laboratori Nazionali del Gran Sasso. GERDA will search for  $^{76}\text{Ge}$  neutrinoless double beta decay with an aim for 100-fold reduction in background compared to predecessor experiments. This ambition necessitates innovative design approaches, strict selection of low-radioactivity materials, and novel techniques for active background suppression. The core feature of GERDA is its array of germanium detectors for ionizing radiation, which are enriched in  $^{76}\text{Ge}$ . Germanium detectors are the central theme of this dissertation. The first part describes the implementation, testing, and optimisation of Monte Carlo simulations of germanium spectrometers, intensively involved in the selection of low-radioactivity materials. The simulations are essential for evaluations of the gamma ray measurements. The second part concerns the development and validation of an active background suppression technique based on germanium detector signal shape analysis. This was performed for the first time using a BEGe-type detector, which features a small read-out electrode. As a result of this work, BEGe is now one of the two detector technologies included in research and development for the second phase of the GERDA experiment. A suppression of major GERDA backgrounds is demonstrated, with  $(0.93 \pm 0.08)\%$  survival probability for events from  $^{60}\text{Co}$ ,  $(21 \pm 3)\%$  for  $^{226}\text{Ra}$ , and  $(40 \pm 2)\%$  for  $^{228}\text{Th}$ . The acceptance of  $^{228}\text{Th}$  double escape events, which are analogous to double beta decay, was kept at  $(89 \pm 1)\%$ .



# Contents

<b>Introduction</b> .....	9
Motivation .....	9
1. Physics of neutrinos .....	10
1.1. Neutrinos and the Standard Model of particle physics .....	10
1.2. Open questions in the physics of neutrinos .....	11
1.3. Neutrinoless double-beta decay .....	12
2. Germanium detectors .....	14
2.1. Fundamental principles of semiconductor detectors .....	14
2.2. Radiation interaction .....	15
2.3. Signal development in a semiconductor detector .....	17
2.4. HPGe detector .....	18
2.5. Signal read out and resolution .....	19
3. The GERDA experiment .....	20
3.1. Data taking phases of GERDA .....	22
3.2. Low background materials selection and HPGe spectrometry .....	23
3.3. Background suppression using pulse-shape analysis .....	24
<b>I Germanium spectrometry: Monte Carlo simulations for low-level measurement evaluation</b> .....	27
4. Low-level gamma-ray spectrometry at MPIK .....	27
5. Evaluation of material screening measurements .....	27
6. Monte Carlo code .....	29
7. Monte Carlo simulations of material-screening detectors .....	30
8. Monte Carlo simulation validation with measurements .....	33
8.1. Environmental Radioactivity Comparison Exercise 2005 .....	33
8.1.1. Comparison of GERDA laboratories .....	33
8.1.2. Results .....	34
8.1.3. Additional investigation .....	35
8.1.4. Discussion .....	36
8.2. Environmental Radioactivity Proficiency Test Exercise 2007 .....	36
8.3. Assessment of Bruno and Dario software models .....	38
9. Optimisation of the software model of Corrado spectrometer .....	41
9.1. Experimental measurements .....	42
9.2. Dead layer thickness determination .....	42
9.3. Detector active volume determination .....	43
9.4. Results and discussion .....	45
10. Application of the Monte Carlo efficiency determination to material-screening measurements evaluation .....	45

<b>II Germanium detector signal analysis: BEGe detector study</b> .....	49
11. Detector setup .....	50
11.1. Detector read out and DAQ system.....	51
11.2. Detector characterisation and testing.....	54
11.2.1. DAQ system stability .....	54
11.2.2. Charge collection study .....	56
12. Pulse shape analysis .....	60
13. Experimental pulse shape discrimination .....	64
13.1. Pulse shape discrimination method .....	65
13.2. Cut function uncertainties and fluctuation .....	68
13.3. Validation measurements .....	71
13.3.1. Coincidence setup for single Compton scattering measurements .....	72
13.3.2. Coincidence measurements evaluation.....	77
13.3.3. Collimated beam measurements.....	80
13.3.4. Validation measurements discussion.....	82
13.4. Results and discussion.....	83
14. Feasibility of BEGe detectors for double beta decay experiments .....	87
<b>Appendix</b> .....	89
<b>Bibliography</b> .....	91
<b>Acknowledgements</b> .....	97

# Introduction

The aim of this thesis was to take part in the GERDA experiment [1] with the use of and by improvement of germanium spectrometry. At the beginning of the introductory part, a brief overview of neutrino physics and its history will be given, concluding with the summary of experimental search for some of its open questions. Before describing the details of the GERDA experiment, basics of germanium spectrometry will be recapitulated. Afterwards, the connections of individual parts of this work to various aspects of GERDA will be explained. The experimental work is divided into two main parts, each related to one aspect of germanium detector technology.

## Motivation

The experimental work presented in this thesis contributes to the development of technology for, and the implementation of GERDA, an experiment in fundamental neutrino physics. The rapidly evolving field of neutrino physics is gaining relevance in a wide range of subjects, from elementary particle physics, where it originated, all the way to possible applications in astronomy and geology.

Neutrinos represent the edge of our current knowledge of particle physics. The theoretical model describing neutrino oscillations is the first confirmed theory of physics beyond the Standard Model which has reigned particle physics for decades. This new physics is needed to solve questions of cosmology and astrophysics, such as the matter-antimatter asymmetry, the dark matter, and dark energy, which Standard Model cannot answer.

In astrophysics, neutrinos have already played a major role by verifying our understanding of the processes taking place inside the Sun. Other powerful sources of neutrinos in our Galaxy are supernovae, releasing approximately 99% of their energy in a rapid burst of neutrinos. Detecting them can improve our understanding of supernovae, and even provide an advance warning for follow-up astronomical observations. In addition, neutrinos themselves can be used as an observational tool, providing a new window to the Universe. They are the only known particles which are not significantly attenuated by their travel through the interstellar medium, and so can reveal sources hidden for other observational techniques. Projects like Ice Cube [2] and KM3NeT [3] are the first steps in the emerging field of neutrino astronomy.

On our home planet, neutrino physics is becoming equally important. Detecting geo-neutrinos (antineutrinos from the decays of uranium, thorium and potassium in rocks) can explore the total content of radioactive isotopes in the Earth's interior. This information will be an experimental validation of the geological model of the planet, with consequences on the understanding of planet formation and evolution. First results, although only rough, were already obtained by the KamLAND experiment [4]. Extended future possibilities include applications outside of science, e.g., neutrino detectors for remote monitoring of nuclear reactors, and even employing the matter effects on directed neutrino beams to search for mineral deposits in Earth's crust [5].

Experiments such as GERDA lead to enabling and expanding the wide spectrum of neutrino physics applications, by studying the fundamental properties of neutrinos. The underlying technol-

ogy of GERDA is the germanium spectrometry, a subject that is already well established in a broad range of applications. Germanium detectors are used, e.g., in nuclear industry, environmental monitoring, and in fundamental physics. The research and development involved in GERDA help also to push the limits of this technology. Even after several decades of their widespread employment, new significant improvements (such as, e.g., segmentation, or digital pulse-shape analysis) are continuously being applied to germanium detectors.

## 1. Physics of neutrinos

Neutrinos were postulated at the end of 1930 by Pauli as a solution to the problem of energy conservation in the  $\beta$ -decay. Energies of electrons emitted in  $\beta$ -decay have a continuous spectrum, which is in apparent contradiction with the law of energy conservation, unless another, unseen, particle carries away the lost energy. Fermi developed the theory further in the 1930's. His description of the massless, chargeless, weakly interacting lepton was successful in explaining the  $\beta$ -decay and other natural phenomena. However, the experimental confirmation of the existence of neutrinos was elusive until 1956, when Cowan and Reines observed reactor antineutrinos in the Savannah River experiment [6].

### 1.1. Neutrinos and the Standard Model of particle physics

The Standard Model (SM) of particle physics describes neutrinos as massless leptons, coming in three flavours:  $e$ ,  $\mu$ , and  $\tau$ , associated with their charged leptons: *electron*, *muon*, and *tau*. Neutrinos interact only via the weak force ( $W$  or  $Z$  boson exchange) and gravity. Neutrinos always have left-handed helicity and antineutrinos right-handed helicity. According to the SM, the *lepton number* is conserved for each flavour family (i.e. the number of leptons of a particular flavour is the same before and after any interaction).

Indications that the SM description of neutrinos might be incomplete first appeared in 1968, when the Homestake experiment [7] discovered a deficit in the measured solar neutrino flux compared to predictions from the astrophysical model of the Sun. This "solar neutrino problem" [8] was later reinforced by several experiments, including Kamiokande [9] and Gallex/GNO [10,11]. Later, atmospheric neutrino experiments, detecting neutrinos from interactions of cosmic rays with the Earth's atmosphere, observed similar anomalies (reported by IMB [12], Soudan 2 [13] and Kamiokande [14] collaborations).

The neutrino oscillation hypothesis was first suggested by Pontecorvo and developed by him in 1960's into its modern form [15]. Strong evidence for neutrino oscillations as a solution to the solar neutrino problem was presented by the Sudbury Neutrino Observatory [16], which was able to measure the solar flux of all neutrino flavours via elastic scattering and neutral-current interaction, while simultaneously monitoring the electron-only flavour flux via charge-current reaction. The Super-Kamiokande experiment provided further evidence for the atmospheric neutrino oscillations [17], later confirmed by accelerator experiments (K2K [18] and MINOS [19]). Finally, in 2004 the reactor neutrino oscillation parameters measured by the KamLAND experiment, confirmed that neutrino oscillations with large mixing angle are the solution to the solar neutrino problem [20].

The SM description of neutrino interactions, via their *flavour eigenstates*, is well confirmed. To account for neutrino oscillations, the SM must be extended by including non-zero neutrino masses, which can lead to lepton mixing. The relation between the flavour and the *mass eigenstates* is described by the unitary Pontecorvo-Maki-Nakagawa-Sakata (PMNS) mixing matrix  $U$ , analogous to the quark mixing matrix. The interaction between charged leptons and neutrinos happens via their coupling to the  $W$  boson (Figure 1).

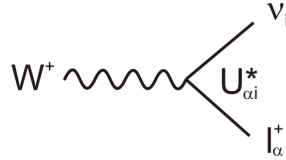


**Figure 1** A lepton –  $W$  boson vertex with a neutrino  $\nu_i$  ( $i = 1, 2, 3$ ).

A charged lepton  $l_\alpha$  (where  $\alpha$  is its flavour), produced at a  $W$  – lepton vertex, can be accompanied with a neutrino  $\nu_i$  of any mass eigenstate  $i$  ( $i = 1, 2, 3$ ). The probability that a particular mass eigenstate is produced in this vertex is given by the square of the corresponding element of the leptonic mixing matrix,  $|U_{\alpha i}|^2$ . The superposition of all possible mass eigenstates which can be produced in the  $W$  – lepton vertex is the neutrino flavour eigenstate  $\nu_\alpha$ :

$$|\nu_\alpha\rangle = \sum_i U_{\alpha i}^* |\nu_i\rangle \quad (1)$$

Thus, the neutrino is created as a specific superposition of mass eigenstates (namely as the flavour eigenstate  $\nu_\alpha$ ) and after propagating a certain distance it is also detected as a flavour eigenstate (the propagating  $\nu_i$  are not measured). At a particular energy, the velocities of the mass eigenstates are different due to the differences in their masses. The energy is given by the production process and is constant for all states in the superposition. Each mass eigenstate will have a different phase, related to the travelled distance  $L$ , the energy  $E$ , and a square of its mass  $m_i$ . The phase is given by:

$$m_i^2 \frac{L}{2E} \quad (2)$$

Since the final state is a superposition of the mass eigenstates (as long as they stay coherent), the individual contributions interfere. Their phase differences then give rise to flavour oscillations:

$$\text{Amp}(\nu_\alpha \rightarrow \nu_\beta) = \sum_i U_{\alpha i}^* e^{-im_i^2 \frac{L}{2E}} U_{\beta i} \quad (3)$$

When propagating through matter, the flavour oscillations are different. The forward scattering potential is different for electron neutrinos, because the charged leptons present in ordinary condensed matter are exclusively electrons. This effect changes the propagation of the electron neutrino compared to the other flavours, and thus significantly affects the oscillation amplitudes.

## 1.2. Open questions in the physics of neutrinos

Some parameters of the PMNS matrix have already been obtained from the detection of solar and atmospheric neutrinos. These known parameters are the *mixing angles*  $\theta_{12}$  and  $\theta_{23}$  related to the mass-square differences  $\Delta m_{21}^2$  and  $|\Delta m_{31}^2|$  of the neutrino mass eigenstates. The value of the mixing angle  $\theta_{13}$  is constrained by an upper limit, obtained from the reactor experiment Chooz [21]. The

unknown parameters of the PMNS matrix are the *charge-conjugation parity (CP) violating phases* (one or three, depending on the nature of the neutrino mass). Observing this CP violation could be a key to understanding the asymmetry between the amounts of matter and antimatter in the Universe.

Although the mass-squared differences are known, the absolute mass scale and the hierarchy of the neutrino masses are still unknown. Knowledge of the absolute neutrino mass could have important consequences on cosmology and the hierarchy is important for fundamental physics, like Grand Unified Theories (which relate leptons to quarks). There are also two separate possibilities of the mechanism by which neutrinos obtain their mass: the Dirac mass term (like with other leptons), the Majorana mass term (determining that neutrinos are their own antiparticles), or a mixture of both. The option realised in nature is still unknown.

### 1.3. Neutrinoless double-beta decay

Since neutrinos are chargeless, the only way to distinguish a neutrino from an antineutrino (and thus to test if  $\nu_i = \bar{\nu}_i$ ) is its helicity. However, the neutrino mass is very small and so they mostly travel near the speed of light. If we would attempt to experimentally change the helicity of neutrinos (e.g. by moving the observing frame of reference at a speed higher than the speed of the neutrino) to test if they would then interact as antineutrinos, the energy requirements would be prohibitively high ( $> 10^5$  TeV for  $\sim 0.05$  eV neutrinos produced by  $\pi^+$  decay [22]).

Currently, the only known experimental possibility to test the Majorana nature of neutrinos is to observe neutrinoless double beta ( $0\nu\beta\beta$ ) decay. Double beta decay is a second-order weak-interaction process observable for some even-even nuclei, for which the single beta decay is energetically forbidden (Figure 2). This process, in which two electrons and two antineutrinos are emitted simultaneously (Figure 3, left), is described adequately by the SM, and was observed in many nuclei (e.g.  $^{48}\text{Ca}$ ,  $^{76}\text{Ge}$ ,  $^{100}\text{Mo}$ ,  $^{130}\text{Te}$ ,  $^{150}\text{Nd}$  ...). In contrast, the  $0\nu\beta\beta$ -decay, in which only the two electrons are emitted (Figure 3, centre), is a lepton number violating process (violation by two units), which requires the existence of massive Majorana neutrinos [23].

Standard two-neutrino double beta decay creates electrons with continuous (beta decay like) energy spectrum, with the endpoint corresponding to the energy difference between initial and final state ( $Q$ -value). Since no neutrinos are emitted in the  $0\nu\beta\beta$ -decay, the two created electrons have a sharp total energy, equal to the  $Q$ -value. Typical double-beta decay spectrum is shown on the right part of Figure 3.

Observing the  $0\nu\beta\beta$ -decay would not only test the Majorana nature of neutrinos and the conservation of the lepton number, but its probability also depends on neutrino masses:

$$\left(T_{1/2}^{0\nu\beta\beta}\right)^{-1} = G_{0\nu}(Q, Z) \cdot |M_{0\nu}|^2 \cdot |m_{ee}|^2 \quad (4)$$

where  $G_{0\nu}$  is an integrated cinematic factor,  $M_{0\nu}$  a nuclear-matrix element, and

$$m_{ee} = \sum_i U_{ei}^2 m_i \quad (5)$$

is the *effective Majorana mass*, a coherent sum of electron-flavour neutrino mass eigenstates. By setting the neutrino mass scale, the measurement of the  $0\nu\beta\beta$ -decay half life could also decide on the hierarchy of neutrino masses (see Figure 4). In addition, the Majorana mass term allows for the existence of two extra CP-violating phases in the PMNS matrix. Detection of the  $0\nu\beta\beta$ -decay could therefore solve most of the open questions in the physics of neutrinos.

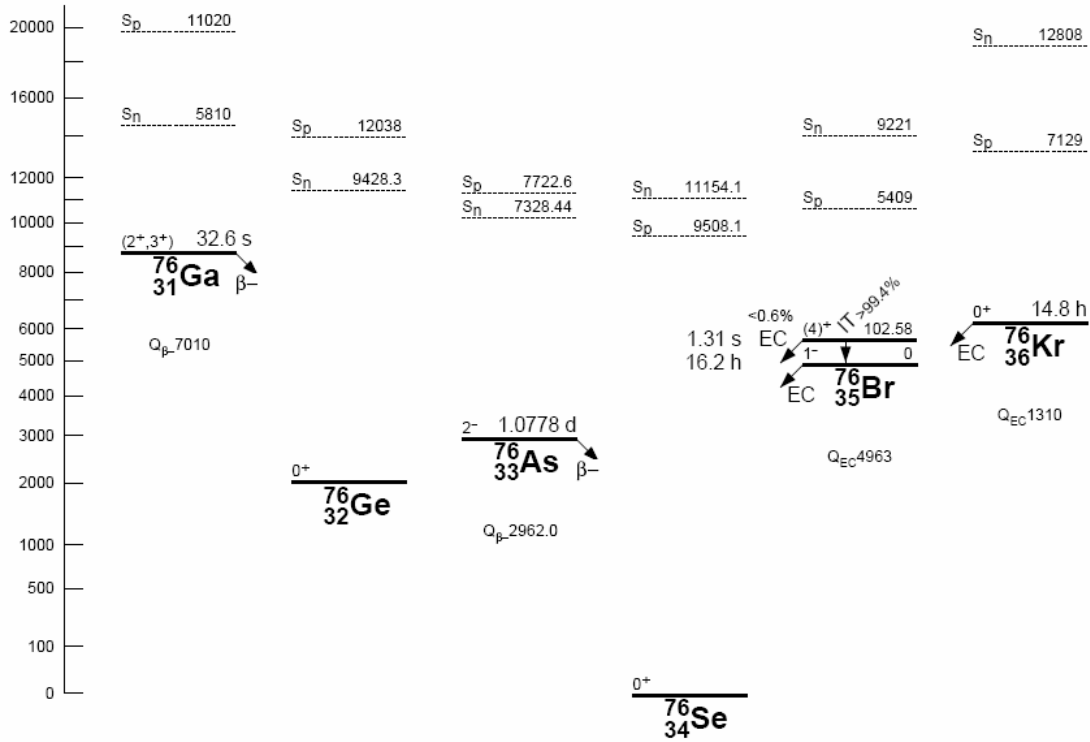


**Figure 2** A part of the summary drawing for isobar chain  $A = 76$ , adapted from [24]. The vertical energy scale is in keV. It is apparent that  $^{76}\text{Ge}$   $\beta$ -decay to  $^{76}\text{As}$  is energetically forbidden, but a double  $\beta$ -decay to  $^{76}\text{Se}$  is allowed.

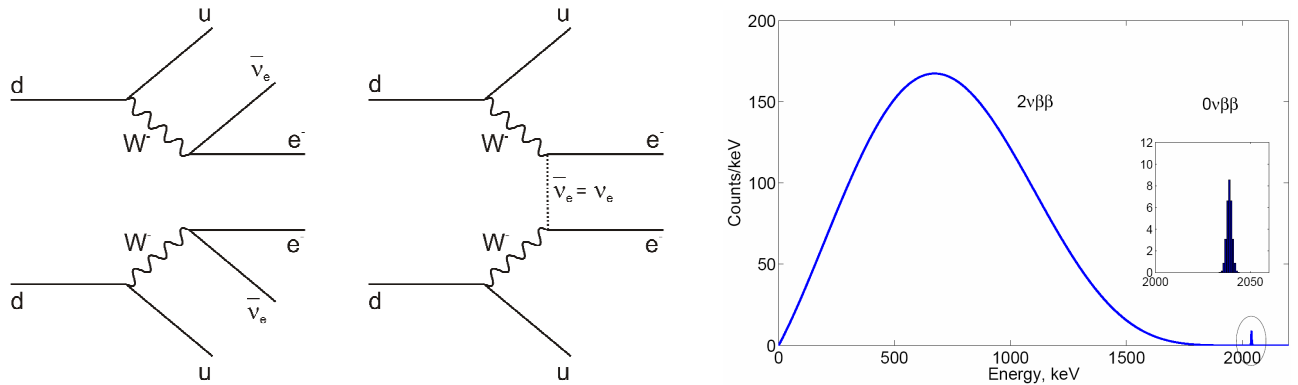


**Figure 3** **Left:** Feynman diagram of the Standard Model allowed two-neutrino double beta decay. **Centre:** Feynman diagram of neutrinoless double beta decay via an exchange of a massive Majorana neutrino. **Right:** Calculated double beta decay spectrum of  $^{76}\text{Ge}$  in an HPGe detector (from [25]), corresponding to an exposure of 72 kg·y. The  $2\nu\beta\beta$  continuum was calculated with  $T_{1/2}^{2\nu\beta\beta} = 1.7 \cdot 10^{21}$  years, and the  $0\nu\beta\beta$  peak with  $T_{1/2}^{0\nu\beta\beta} = 1.2 \cdot 10^{25}$  years and a resolution of 3 keV FWHM at 2 MeV.

Like GERDA, several experiments under preparation or already running, are aiming at the detection of the  $0\nu\beta\beta$ -decay using various detection techniques. Among them are: NEMO3 [26] / SuperNEMO [27] (a magnetic tracker and calorimeter using  $^{100}\text{Mo}$ ,  $^{150}\text{Nd}$ ); CUORICINO [28] / CUORE [29] (an array of  $\text{TeO}_2$  bolometers with natural 27%  $^{130}\text{Te}$  content); EXO [30] (80% enriched  $^{136}\text{Xe}$  liquid scintillator and TPC, with daughter nucleus detection via laser induced fluorescence). From past experiments, the best limits on the half life of  $0\nu\beta\beta$ -decay were obtained by the IGEX [31] and HdM [32] collaborations, both using low-background germanium spectrometers with crystals enriched in  $^{76}\text{Ge}$ . The 90% confidence level lower bound on  $^{76}\text{Ge}$  half life from the latter experiment

is  $T_{1/2}^{0\nu\beta\beta} > 1.9 \cdot 10^{25}$  years [33], corresponding to an upper limit on an effective Majorana mass of  $m_{\beta\beta} < 0.55$  eV [34] (using the nuclear matrix element from [35]). Klapdor-Kleingrothaus et al. published a claim of positive detection of  $^{76}\text{Ge}$   $0\nu\beta\beta$ -decay, at a level of  $T_{1/2}^{0\nu\beta\beta} = (2.23_{-0.31}^{+0.44}) \cdot 10^{25}$  years [36], using the data from the HdM experiment.

Germanium spectrometry continues to be the most sensitive probe of the  $0\nu\beta\beta$ -decay, with the GERDA experiment and the future Majorana experiment [37] (and a possible collaboration of the two) both employing this detector technology. The expected neutrino mass sensitivity of GERDA in its various phases is shown in Figure 4.

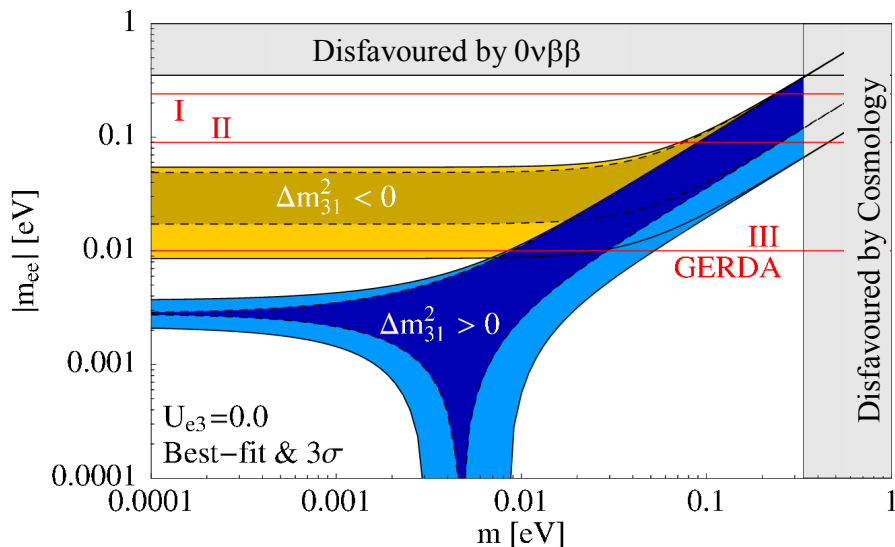


**Figure 4** Effective Majorana mass  $|m_{ee}|$  as a function of the smallest neutrino mass  $m$ , for the case of normal (blue area) and inverted (yellow area) mass hierarchy. Projected sensitivities of the first two phases of GERDA, as well as a hypothetical Phase 3 (1 t scale  $^{76}\text{Ge}$  experiment), are indicated with the red lines. Taken from [38].

## 2. Germanium detectors

As was stated in Section 1.3, germanium spectrometry is currently the leading technique used in the search for  $0\nu\beta\beta$ -decay. More specifically, the technology in the focus of this thesis is the spectrometry of ionizing radiation with high-purity germanium (HPGe) detectors. In this section, the basics principles behind HPGe spectrometry and its aspects, which are relevant to the GERDA experiment and to the experimental work presented in this thesis, will be given.

### 2.1. Fundamental principles of semiconductor detectors

Semiconductor detectors make use of the small energy gap between the valence and conduction bands of the semiconductors (0.67 eV in Ge). At low temperatures, most electrons are confined to the valence band – they are bound in a covalent bond between the atoms of the semiconductor crystal. Adding energy to the electrons (e.g. via interaction with ionizing radiation) puts them into the conduction band and they can move freely in the crystal. After the release of an electron from

the covalent bond, a positively charged ion is left at its place. By applying an electric potential difference to the semiconductor material, current flows via the conduction-band electrons and also by movement of the positive charges – called *holes*. A hole can move in the crystal by accepting a bound electron from a neighbouring atom.

In reality, semiconductor materials are never infinitely pure. *Acceptor* atoms are impurities with one fewer electron in their valence band. If they are inside a semiconductor crystal, this electron is missing in the covalent bond with the semiconductor atoms. An electron can be attracted to this covalent bond, thus a hole is created and can conduct current. Conversely, *donor* impurities have an extra electron, which is easily released into the conduction band. Therefore semiconductor materials always contain free charge carriers – electrons (*n*-type semiconductor) or holes (*p*-type semiconductor). Under normal conditions, the number of free charge carriers is completely dominated by the net difference between the number of acceptor and donor impurities. In the growth process of a semiconductor crystal, one type of impurities always prevails.

Combination of their relatively high density and small energy required to create an electron-hole pair (on average 2.9 eV in Ge), makes semiconductors useful materials for spectrometry of ionizing radiation. However, it is necessary to remove all free charge carriers from the material, otherwise the fluctuations in the electric currents created by them could overwhelm the signals from the radiation interactions. By joining *p* and *n*-type semiconductors (a diode), an area devoid of free charges is created at the junction – *depleted region*. This happens because the free electrons from the *n*-type material will diffuse into the *p*-type material and holes vice versa. Negative and positive immobile ions are left at the filled acceptor-sites and vacated donor-sites. This creates a space charge which suppresses further charge carrier diffusion. A net potential difference builds up across the *p-n* junction. The resulting electric field will force any electrons/holes created in this region to drift towards the positive/negative potential. This way an electric signal will be generated at the borders of the junction – the depleted region acts as a *sensitive volume* of a detector. The electric field inside the depleted region and consequently the region's width can be significantly increased by augmenting the potential difference across the *p-n* junction with a voltage applied externally. This external voltage is called *reverse bias*, because the potential difference is applied in the direction in which no current can flow across the diode. However, due to the small gap between the valence and conductive band energy levels, the temperature of the material can cause spontaneous appearance of charge carriers in the conduction band and thus a small leakage current is always present. To sufficiently deplete the *p-n* junction region it is therefore necessary to cool the material to cryogenic temperatures.

## 2.2. Radiation interaction

Practically all of the energy absorbed by  $\gamma$ -ray interactions (Compton scattering, photo-electric capture and pair production), as well as  $\alpha$  and  $\beta$  particle interactions in a semiconductor detector is ultimately transferred to electrons. Only a small fraction of energy transfer happens by interaction with nuclei (this fraction increases for interactions of neutrons and heavier ions).

Through the Compton scattering,  $\gamma$ -rays can transfer significant part of their energy directly to an electron. Since the detector active volume is depleted from free charge carriers, most likely it will be an electron from outer atomic shells, with insignificant binding energy. In a large volume detec-

tor, it is very likely that a  $\gamma$ -ray will undergo several Compton scatterings before it escapes or its energy falls into the range where photo-effect is dominant.

Photo-electric absorption of a  $\gamma$ -ray by the atomic electron cloud results in an emission of an electron from its shell. The electron gains the energy of the photon minus its binding energy. It is most often one from the K-shell, unless the  $\gamma$ -ray energy is too low. In that case an electron from higher shells is ejected. The atom is left in an excited state and an electron from a higher energy level falls into the vacancy. This is accompanied by X-ray fluorescence, or by Auger electron emission. If an X-ray is emitted, it can either escape the detector or undergo further photo-absorptions until the whole energy is transferred to electrons. The maximal energy of the X-ray is the K-shell binding energy (11.1 keV in germanium).

With higher energies of  $\gamma$ -rays, pair production becomes more probable. In this case the photon interacts with the Coulomb field of a nucleus and disintegrates into an electron and a positron. The leptons will equally share the energy of the photon minus the two electron rest masses. After the positron loses energy and thermalises, it annihilates with another electron (typically within 1 ns [39]). The two resulting annihilation  $\gamma$ -quanta then can undergo Compton or photo-electric interactions or escape the detector.

Consequently, most of the charge-carrier (free electrons and holes) production in  $\gamma$ -ray interactions in the detector is resulting from the energy losses of fast electrons (or positrons). The only difference from  $\beta$ -particle interaction is that  $\gamma$ -rays can create fast electrons simultaneously in several places throughout the crystal. The fast electrons lose energy by almost continuous and simultaneous interactions with many atoms in the crystal. This happens via an exchange of virtual photons (*Coulomb interactions*) or by emission of real photons (*bremstrahlung*). The Coulomb interactions, also called *collisional losses*, result directly in a creation of free charge carriers through ionisation or excitation (with subsequent deexcitation) of atoms. The bremstrahlung, or *radiative losses*, is an emission of electromagnetic radiation due to charge acceleration in the Coulomb field of a nucleus. The spectrum of the bremstrahlung radiation is continuous, with the maximal energy of the emitted photons equal to the incident electron energy. Typical electron bremstrahlung spectrum and its dependence on electron energy is shown in Figure 5. The ratio between average collisional and radiative specific energy losses is given approximately by [40]:

$$\frac{(dE/dx)_r}{(dE/dx)_c} \cong \frac{E \cdot Z}{700} \quad (6)$$

where  $E$  is in units of MeV.

The range of electrons in moderate density materials is roughly 1 mm per MeV [40]. The energy loss of positrons is equivalent to that of electrons, until their thermalisation, at which point they annihilate, most likely with one of the free electrons created near the end of their track. Compared to electrons,  $\alpha$ -particles lose energy much faster (range in germanium of a 5 MeV  $\alpha$  is  $\sim 2 \mu\text{m}$ ) and much less energy can be transferred per collision (about 0.055% of the total  $\alpha$  energy) [40], so no fast electrons are created in their interactions. Likewise, radiative losses are negligible for  $\alpha$ -particles. Neutrons are different from other radiations discussed in this section in that they can only interact with nuclei. They can be detected only indirectly through secondary radiations created by their reactions or by delayed decays of reaction products. Thus, unlike with  $\alpha$ ,  $\beta$  and  $\gamma$  interactions, signals induced by neutrons are usually not proportional to the energy they lose in the detector.

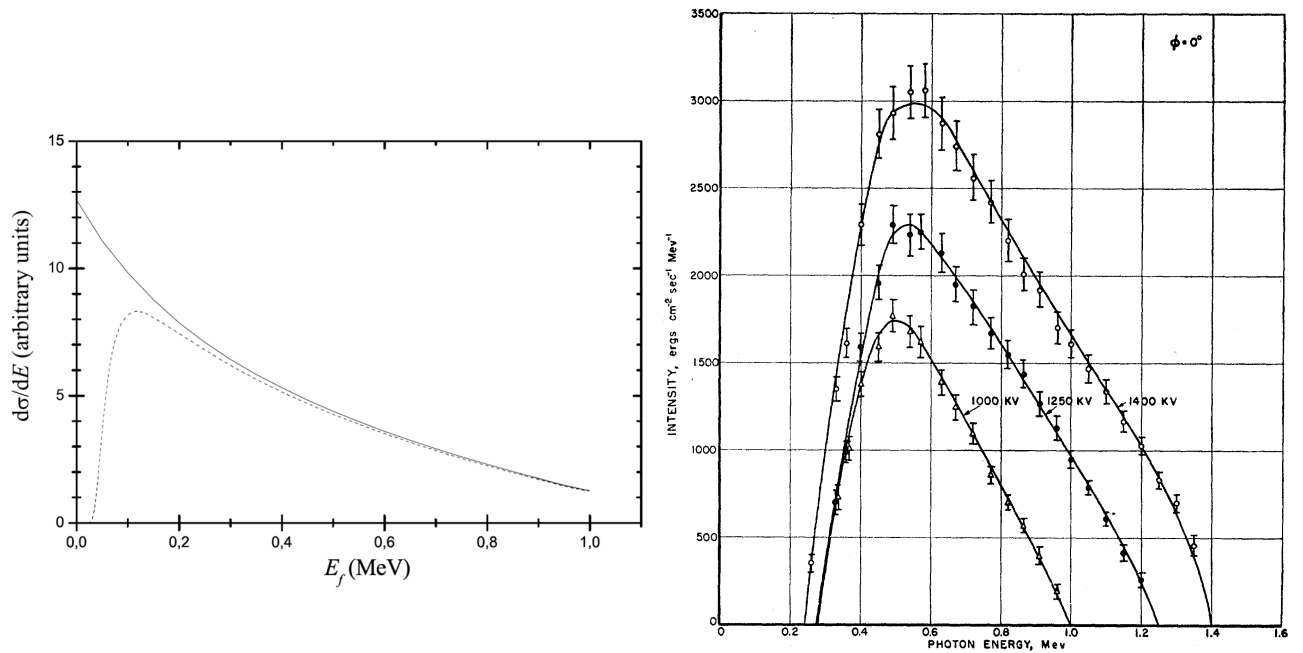


**Figure 5** **Left:** Calculated bremsstrahlung spectrum produced by 1 MeV electrons in the dead layer of a germanium detector (from [41]). The dashed line takes into account the bremsstrahlung photon absorption in the dead layer (the electrons reaching active volume are not considered). **Right:** Bremsstrahlung spectra in the forward direction from 1 MeV, 1.25 MeV and 1.4 MeV electrons passing through tungsten target, from [42].

### 2.3. Signal development in a semiconductor detector

The clusters of charge carriers created at the site of the interaction migrate with the electric field (electrons towards positive and holes towards negative potential). The speed of the migration (*drift velocity*) depends approximately linearly on the electric field, until at field values of  $\sim 1$  kV/cm saturation occurs. The saturated velocity in germanium at cryogenic temperatures is  $\sim 10^7$  cm/s for both electrons and holes [40]. The drift velocity also depends on the drift direction relative to the crystal axes [43].

The electrical signal at the contacts of the detector is generated by the movement of the charge carrier clusters with the electric field. Charge  $Q$  induced at the read-out electrode by a point charge  $q$  in between the electrodes is described by the Shockley–Ramo theorem [44]:

$$Q = -q \cdot W(x) \quad (7)$$

where  $W(x)$  is the *weighing potential* at the position  $x$  of the charge  $q$ . The dimensionless weighing potential is a measure of the electrostatic coupling between the charge  $q$  and the read-out electrode. It is equal to the electric potential that would exist at a given position inside the device if the read-out electrode would have a unitary voltage, the other electrode zero voltage, and no space charge present in the detector volume.

The total induced charge will then be the sum of the charges induced by the hole clusters and the electron clusters. As the two charge carrier types move in opposite directions, the clusters will separate and a net charge will be induced at the electrodes. When a cluster of charge carriers reaches an electrode, the charges stop moving and do not contribute any more to the increase. The induced charge will continue increasing until all charge carriers are collected at the electrodes. Since  $W = 1$

at the signal electrode and  $W = 0$  at the other electrode, according to equation (7) the final  $Q$  will be equal to the total charge of the carriers collected at the signal electrode. If no losses of charge carriers happen during their drift through the active volume, this charge will be directly proportional to the absorbed energy from radiation interaction.

Losses can occur when the time required to collect all charge carriers at the electrodes becomes comparable to the charge carrier lifetime. The average lifetime of charge carriers can be as large as a second in a pure semiconductor, however it is reduced by several orders of magnitude in the presence of even the lowest achieved impurity concentrations, and if crystal lattice defects occur [40]. These imperfections can either retain charge carriers until they are released again due to thermal excitation (*charge traps*), or encourage recombination by trapping both electrons and holes (*recombination centres*). Charge traps have the effect of increasing the charge collection time, while the recombination centres cause signal losses.

## 2.4. HPGe detector

With impurity concentrations at levels as low as  $10^9 \text{ cm}^{-3}$ , which is the best routinely achieved material purity, the semiconducting germanium is an ideal material for  $\gamma$ -ray detectors. The thickness of the depleted region is given by [40]:

$$d \cong \left( \frac{2\varepsilon V}{eN} \right)^{\frac{1}{2}} \quad (8)$$

where  $\varepsilon$  is the static permittivity of the material,  $e$  the elementary charge,  $V$  the reverse bias voltage and  $N$  the impurity concentration (equivalent to charge carrier concentration). For high-purity germanium (HPGe),  $\varepsilon = 16 \cdot \varepsilon_0$ ,  $N \approx 10^9 \text{ cm}^{-3}$ , and typical bias voltages reach maximally  $\sim 5 \text{ kV}$  (at higher voltages the risk of a breakdown increases). With these limiting parameters, the equation (8) predicts achievable depletion depth as large as  $d \approx 10 \text{ cm}$ , enabling the fabrication of detectors with useful active volumes. The free charge carrier concentration in the depleted volume drops to the order of  $\sim 100 \text{ cm}^{-3}$ . High density of germanium and its relatively high atomic number ( $Z = 32$ ), combined with the good intrinsic energy resolution and the possibility of large active volumes make HPGe the preferred material for  $\gamma$ -ray spectrometry.

HPGe crystals of  $\gamma$ -ray spectrometers are most often built in a closed-end coaxial geometry (Figure 6). For a  $p$ -type material, the junction is made by creating an  $n+$  (high donor concentration) layer on the outer surface, by doping the germanium with interstitial lithium donor atoms. This creates a conductive contact, but simultaneously a  $\sim 1 \text{ mm}$  thick inactive layer that can not be depleted (*dead layer*). The inner conductive contact is made by implanting the surface of the crystal borehole with acceptor atoms (usually boron), creating a thin  $p+$  layer. The inner contact, which collects holes, acts as a read-out electrode. In  $n$ -type materials the doped layers are built inversely, but the read-out electrode is typically also in this case at the inner contact (collecting electrons). In both  $p$ - and  $n$ -type diodes, the depleted region grows from the outer surface inwards when applying the reverse bias voltage.

The thick outer electrode of  $p$ -type HPGe detectors effectively absorbs external  $\alpha$ - and  $\beta$ -radiation, as well as low energy  $\gamma$ -rays (below  $\sim 10 \text{ keV}$ ). This can be disadvantageous for spectrometry of those radiations, but helps at eliminating background components from external  $\alpha$ - and  $\beta$ -sources in high-energy  $\gamma$ -ray spectrometry.

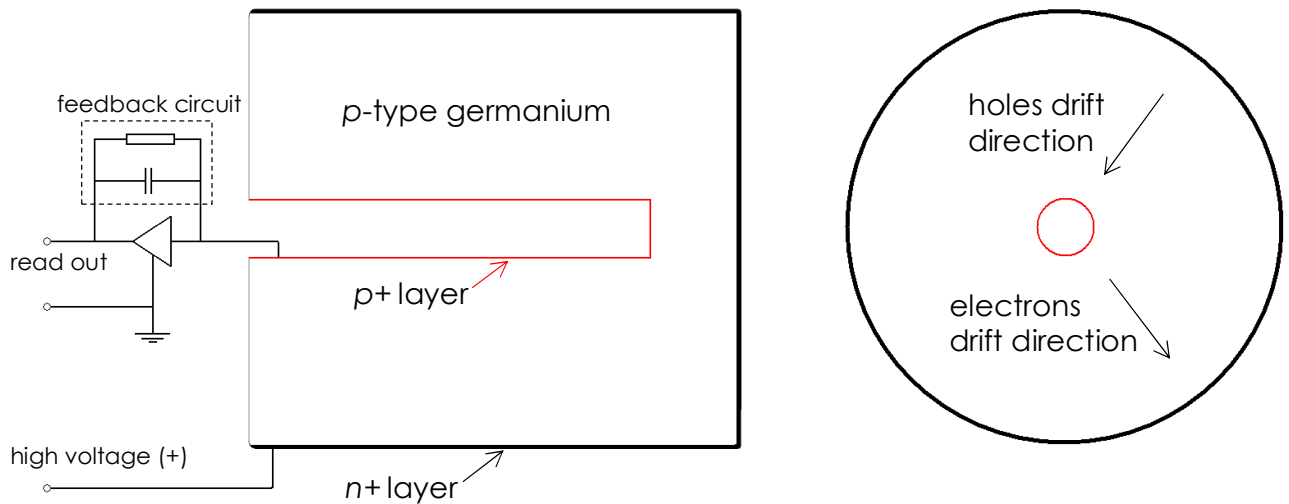


**Figure 6** Schematic drawing of a closed-end coaxial germanium detector from a  $p$ -type material, with a DC-coupled charge sensitive preamplifier using RC feedback.

## 2.5. Signal read out and resolution

Front-end electronics act as an interface between the detector and the system for data acquisition (DAQ). Due to stability and low noise requirements, DC-coupled charge sensitive preamplifiers (see Figure 6) are most often used in high-resolution HPGe spectrometry. The preamplifier converts the collected charge pulse into a voltage pulse, and provides feedback to the capacitance of the detector to remove the collected charge. In applications without too high count rate, this is done using a feedback resistor, which introduces a decay time to the voltage signal. The decay time should be long compared to the signal rise time (which is determined by the charge collection time, typically several 100 ns in HPGe detectors), to avoid *ballistic deficit* – a situation when the short decay time prevents the pulse from reaching its maximal amplitude. Therefore decay times are often on the order of 100 times larger than rise times. However, if the decay time becomes comparable to the average time between radiation-induced signals it can cause an overlay of signals (*pile up*), negatively affecting the measurement of pulse amplitudes.

In addition to the fluctuations in the number of collected charge carriers, the electronics in the read-out circuit can add further noise to the signal. This can be sorted into three groups: parallel, series and flicker noise. The contributions to parallel noise include the leakage currents in the detector diode and the thermal noise in the preamplifier feedback resistor. The noise grows with the increase in count rate and the temperature of the feedback resistor, and decreases with the increase in feedback resistance [39]. The flicker noise also increases with the count rate and is caused by DC current variations in all active devices. The series noise comes mostly from the FET of the preamplifier. It is caused by the statistical variation in the DC current from a diode (shot noise). It decreases with the increase of FET gain, and grows with FET temperature and the total capacitance of the preamplifier input [39]. The capacitance of the detector is a significant part of the input capacitance, along with the feedback capacitor and other components of the preamplifier circuit. As well as the electronic noises and the charge carrier fluctuations, the ballistic deficit also worsens the detector resolution.

The differences between the three components of electronic noise are in their response to integration and differentiation (*signal shaping*) by frequency filters. With the increase of the integration and differentiation constant, the parallel noise grows, and the series noise falls (as well as the effect of the ballistic deficit). The flicker noise is independent on the shaping. Therefore by applying an optimal frequency filter, the resolution of the output pulse amplitude can be optimised.

An important consideration for optimising the signal read-out is the cabling between the detector and the electronic components. The signals from preamplifier are normally transmitted by coaxial cables, which shield the connection from pick up of noise from stray electric and magnetic fields. Transmitting impulses with short rise times along significant distances can cause signal distortions due to frequency dependent attenuation and reflections. The magnitude of these effects is determined by the properties of the cables, especially their resistivity, capacitance, and their impedance match with the electrical components.

### 3. The GERDA experiment

The GERmanium Detector Array (GERDA) experiment [45] aims to search for the  $0\nu\beta\beta$ -decay of  $^{76}\text{Ge}$ . As discussed in Section 1.3, germanium detector experiments are presently the most sensitive probe of  $0\nu\beta\beta$ -decay. This is because they have several advantages:

1. The source of  $\beta\beta$ -decay is the detector material itself, and the  $\beta$ -particles have a short absorption length in germanium. Therefore the detection efficiency approaches 100%.
2. HPGe crystals are among the purest solid materials available. The purification removes also radioactive contaminations so the intrinsic radioactive background is extremely low (the only significant sources are the cosmogenically produced  $^{60}\text{Co}$  and  $^{68}\text{Ge}$ , with activities on  $\sim\mu\text{Bq/kg}$  level expected in the detectors made for GERDA [45]).
3. High isotopic enrichment in  $^{76}\text{Ge}$  is possible and was achieved in past [31,32]. This further improves the ratio of signal to background by increasing the relative amount of source material. The enrichment level of germanium used in GERDA is 86% to 87%.
4. HPGe spectrometers have a very good energy resolution (on the order of 0.1% at the  $^{76}\text{Ge}$   $Q_{\beta\beta}$  energy of 2039 keV). This is advantageous for better separation of the sharp  $0\nu\beta\beta$ -decay peak from background: the  $2\nu\beta\beta$ -decay continuum (see Figure 3, right),  $\gamma$ -lines and Compton continuum.
5. Substantial expertise exists with HPGe detector production and spectrometry, therefore no significant development is necessary to enable their use as well as their performance stability over several years long measurement times with high duty cycle.

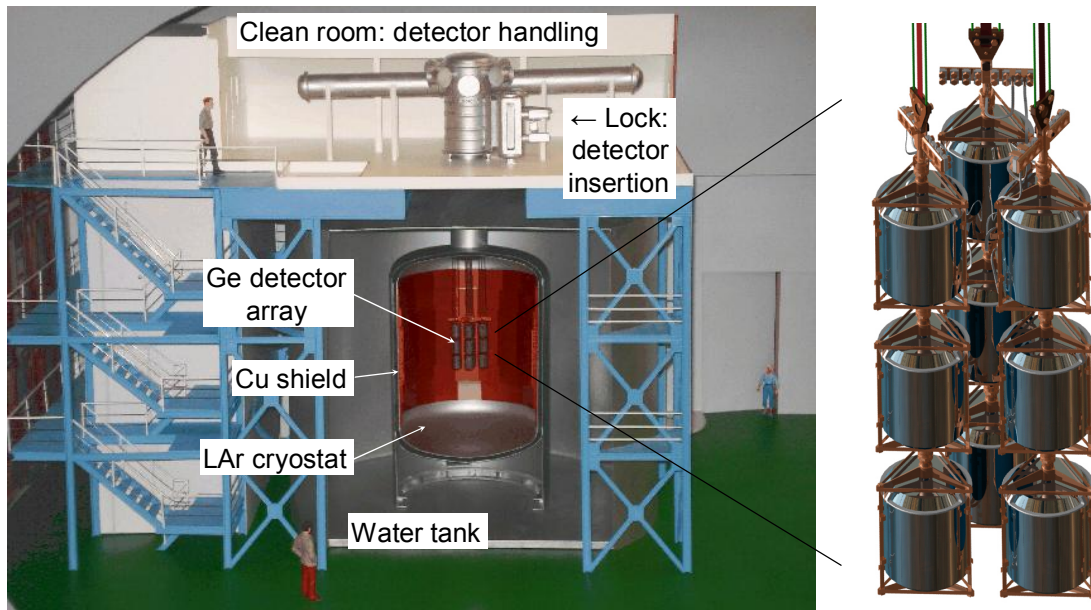


**Figure 7** An artistic model of the GERDA experiment (left) and the Phase 1 array of enriched HPGe detectors (right).

One disadvantage of  $^{76}\text{Ge}$  is that its  $Q$ -value ( $Q_{\beta\beta} = 2039 \text{ keV}$ ) lies below the energy of the radiation from some natural background sources. Most notable backgrounds are the isotopes  $^{208}\text{Tl}$  and  $^{214}\text{Bi}$  from the primordial decay chains of  $^{232}\text{Th}$  and  $^{238}\text{U}$ , respectively. The design of the GERDA experiment is therefore focused on minimising the radioactive background. The overview of GERDA is shown in Figure 7.

To minimise the amount of radioactive contamination close to the detectors, their support structure and electrical connections are made of ultra-pure materials (selected low-background copper, silicon and PTFE), and their mass is minimised. The detectors are immersed in liquid argon, which serves as a shield against gamma radiation and as a cooling medium for the HPGe detectors. The radioactive contamination in liquid argon (LAr) is very low<sup>1</sup>, and if required it can be further purified [46]. The cryogenic liquid fills a  $70 \text{ m}^3$  cryostat from a very low-activity stainless steel ( $^{232}\text{Th}$  and  $^{238}\text{U}$  activity concentrations of  $\sim 1 \text{ mBq/kg}$  or lower [47]), with an additional internal copper shield. The cryostat is placed inside a tank filled with water, providing further background protection against  $\gamma$ -rays and neutrons from the surrounding environment. The water tank also functions as an active veto against high-energy muons from cosmic rays. For this purpose it is instrumented with photomultipliers detecting Cherenkov radiation induced in the water by fast charged particles. The whole setup is situated in the underground Laboratori Nazionali del Gran Sasso (LNGS),  $\sim 1400 \text{ m}$  below surface (3800 m of water equivalent). The cosmic-ray muon flux at these depths is reduced by a factor of  $\sim 10^6$ .

The most significant background sources are expected to be located in the detector material and in the materials of the closest components. Above the surface of Earth, the ultra-pure germanium can be activated by interactions with the hadronic component of cosmic rays. The most important cosmogenic backgrounds are  $^{60}\text{Co}$  and  $^{68}\text{Ge}$ . Their respective production rates at the sea level are

<sup>1</sup> The only significant radioactive background in LAr is  $^{222}\text{Rn}$  [48], which is present at  $\sim \text{mBq/kg}$  levels at production [46]. However, with its 3.8 day half life, after some time the  $^{222}\text{Rn}$  concentration in LAr is dominated by emanation from the walls of the container used.

4 atoms/(kg·d) and 1 atom/(kg·d) [48]. The  $\beta$ -decay of  $^{60}\text{Co}$  can produce events at the energy of  $Q_{\beta\beta}$  via summation of its two  $\gamma$ -rays. The  $^{68}\text{Ge}$  decays via electron capture, with an 86% probability of an X-ray or Auger electron emission, into  $^{68}\text{Ga}$ .  $^{68}\text{Ga}$   $\beta^+$ -decay can deposit energy around the  $Q_{\beta\beta}$  due to its Q-value of 2.9 MeV.

Since the  $\alpha$  and  $\beta$  particles from materials surrounding the detectors are quickly absorbed by the thick LAr and the dead layers of the detectors, they do not pose a significant background risk. The  $\gamma$ -ray emitting thorium and uranium concentrations in these materials, a possible contamination on their surfaces, and  $^{222}\text{Rn}$  (a gaseous daughter of  $^{238}\text{U}$ ) dissolved in the LAr are the most important background sources in GERDA. This background can be reduced by seeking the materials with the highest radiopurity and the lowest emanation of  $^{222}\text{Rn}$ .



**Figure 8** Left: The rocky shielding of GERDA – the Gran Sasso massif. Right: The construction of the basic structure of GERDA nearing completion on 9<sup>th</sup> February 2009.

### 3.1. Data taking phases of GERDA

In the first phase of the experiment eight HPGe detectors, which were previously operated by the Heidelberg-Moscow [32] and IGEX [31] collaborations, will be redeployed. This amounts to 18 kg of germanium enriched to 86% in  $^{76}\text{Ge}$ . The background level in the germanium diodes is envisioned to be  $<10^{-2}$  counts/(keV·kg·y) in the region of interest ( $Q_{\beta\beta} \pm 2$  keV), more than one order of magnitude lower than in previous  $0\nu\beta\beta$ -decay experiments. The major contribution to the background in the previous experiments was from the materials of the conventional vacuum cryostats of the detectors and their internal parts [25]. This will be largely eliminated in GERDA, through the technique of bare detectors immersed in cryogenic liquid [49]. The limiting background in the first phase of GERDA is expected to be the intrinsic  $^{60}\text{Co}$  background of the HPGe detectors, which were exposed to activation by cosmic rays during their time spent above ground [48]. The aim of the first phase is to surpass the state-of-art in  $0\nu\beta\beta$  sensitivity during only a year of data-taking (exposure 15 kg·y), and to confirm or refute the existing claim of  $0\nu\beta\beta$ -decay detection [36]. The

expected sensitivity in  $^{76}\text{Ge}$   $0\nu\beta\beta$  half-life is  $3\cdot 10^{25}$  years, corresponding to the effective Majorana neutrino mass of (0.3-0.9) eV (depending on the choice of matrix elements).

The second phase, for which new enriched HPGe detectors (additional  $\sim 20$  kg, 87%  $^{76}\text{Ge}$ ) will be custom made, aims at another order of magnitude reduction in background to a level of  $<10^{-3}$  cts/(keV $\cdot$ kg $\cdot$ y). The detectors will be manufactured with special emphasis on reducing the cosmogenic activation. This will be achieved by minimising their time spent above ground during production. However, to reach the intended low background levels, active background-suppression methods are necessary in addition to the low-background design of the experiment:

1. the water tank serving as an active Cherenkov  $\mu$ -veto,
2. time-delayed coincidences between some background decays and their short lived daughters (e.g. a correlation between a 10 keV X-ray from  $^{68}\text{Ge}$  decay into  $^{68}\text{Ga}$ , followed by  $^{68}\text{Ga}$   $\beta^+$  decay with a half-life of 68 min),
3. anticoincidence between the detectors in the array,
4. analysis of germanium detector signal time-structure (pulse shape) – discussed in Section 3.3,
5. detector segmentation,
6. anticoincidence with LAr scintillation light.

The first four techniques will be used or tested already in the GERDA Phase 1. The latter two are novel techniques considered for use in Phase 2, and require dedicated detector designs [50] respectively instrumentation of the LAr cryostat with photomultipliers [51]. Aside from the first two techniques which reject cosmic muons and cosmogenic  $^{68}\text{Ga}$ -decays, the other active background-suppression methods make use of the fact that most of the background events are produced by  $\gamma$ -rays from the radioactive contaminations in the materials around the detectors. Photons with energies  $\leq Q_{\beta\beta}$  are likely to lose energy in multiple scatterings (see Section 2.2), with a range of several cm, thus can deposit parts of their energy in multiple detectors or in the LAr volume. On the other hand, the  $\beta\beta$ -decay results in localised interactions of the emitted electrons.

With the expected background level and an exposure of 100 kg $\cdot$ y, the sensitivity of the second phase of GERDA is  $\sim 2\cdot 10^{26}$  years in terms of the  $^{76}\text{Ge}$   $0\nu\beta\beta$  half-life, or (0.1-0.3) eV in terms of the effective Majorana mass. The expected sensitivities of the Phase 1 and Phase 2 (along with a hypothetical Phase 3 with  $10^3$  kg $\cdot$ y exposure) to neutrino masses are shown in Figure 4.

### 3.2. Low background materials selection and HPGe spectrometry

To achieve the intended background index of GERDA,  $<10^{-2}$  and  $<10^{-3}$  counts/(keV $\cdot$ kg $\cdot$ y) respectively in Phase 1 and 2, every component of background has to be kept under control. A comprehensive list of maximally allowable activity concentrations of the individual components of GERDA can be found in [52]. The limits were obtained by means of Monte Carlo simulations and analytical calculations. The strongest requirements are on the germanium diodes themselves and on the cryogenic liquid – on the level of  $\sim 1$   $\mu\text{Bq/kg}$ . The purity level of refined HPGe crystals is identified with measurements of electrically active impurities [53]. The  $^{222}\text{Rn}$  concentration in LAr is obtained via preconcentration on the basis of gas chromatography, and subsequent measurement in

ultra-low background proportional counters [54]. On the second place in terms of radiopurity requirements are the copper shielding and detector-support parts, with maximal tolerable activities on the  $\sim 100 \mu\text{Bq/kg}$  level (corresponding to concentrations of  $\sim 10^{-11} \text{ g/g}$  of the primordial mother isotopes of U and Th).

The three most sensitive techniques for detecting activity concentrations in materials are the mentioned proportional counters, the inductively-coupled plasma mass-spectrometry (ICP-MS) and the HPGe  $\gamma$ -ray spectrometry. All of these methods are used for the material selection for GERDA. The laboratories involved in these measurements (generally called material screening) reach state-of-art sensitivities to radioactive content in materials. The gas proportional counters are used for measurements of  $^{222}\text{Rn}$  concentration in liquids and gases, as well as its emanation from the surfaces of various materials [55]. The ICP-MS technique measures concentrations of the primordial mother isotopes of the natural radioactive nuclides (U, Th and K) in solids [56]. The HPGe spectrometry is sensitive to  $\gamma$ -ray emitting contaminants. Using these methods, all materials in the GERDA experiment have been checked and selected to conform to the predetermined background requirements.

As explained in Section 3,  $\gamma$ -ray emitters from the primordial decay chains, especially  $^{208}\text{Tl}$  and  $^{214}\text{Bi}$ , are the most important backgrounds for the Ge detector array of GERDA. These isotopes are found at the end stages of the  $^{232}\text{Th}$  respectively the  $^{238}\text{U}$  decay chain. Material processing often disturbs the secular equilibrium in the activities of natural decay chains isotopes. The HPGe spectrometry is the most relevant material screening technique for GERDA because it detects these isotopes directly. Furthermore it is capable of reaching sensitivities down to  $\sim 10 \mu\text{Bq/kg}$ .

Requirements on ultra-low level HPGe spectrometry are similar to those on the GERDA experiment itself. Most important is an efficient shielding against external radiation and reduction of radioactive contamination inside the detector and its surrounding parts. The most sensitive HPGe detector worldwide used routinely for material screening is the GeMPI [57], is located 1400 m under ground at LNGS and operated in a collaboration of LNGS and Max-Planck-Institut für Kernphysik (MPIK). A summary of the GERDA material screening laboratories was published in [58], and a compilation of selected results of HPGe spectrometry for GERDA can be found in [52]. Part I of this thesis will deal with aspects of the evaluation of low level HPGe spectrometry measurements performed at MPIK.

### **3.3. Background suppression using pulse-shape analysis**

In ionizing radiation spectrometry, pulse-shape analysis refers to the investigation of the time structure (shape) of electrical signals from the detector. Pulse-shape analysis techniques have already been used in HPGe spectrometry, e.g. for improvement of the peak-to-Compton ratio, timing and energy resolution, for event localisation, and for discrimination of  $\gamma$ -ray events from nuclear recoils and beta-particle interactions [59,60]. The latter has been applied as a background suppression technique also in previous  $^{76}\text{Ge}$   $0\nu\beta\beta$ -decay experiments [61-65].

As explained in Section 2.2, the signals created by radiation in germanium detectors in principle do not depend on the type of the responsible particle (for  $\alpha$ ,  $\beta$ , and  $\gamma$  interactions). This is because the ionising particle interactions ultimately result in energy transfer to electrons, and afterwards the signal generation always follows the same processes. However,  $\gamma$ -rays with energies above a few

hundred keV have a range in dense materials significantly higher than charged particles. Additionally, the cross section of Compton scattering becomes dominant compared to the photo-electric effect. Therefore, in large HPGe detectors there is a high probability that these photons will undergo more than one interaction and deposit energy in several spots across the detector volume. Compared to that, electrons will most probably lose energy along a path on the order of 1 mm long. This difference is the basis for discrimination between  $\gamma$ -ray and electron interactions.

For  $\beta\beta$ -decay experiments it is especially useful to distinguish highly localised energy depositions induced by electrons from  $\gamma$ -ray events distributing their energy over large volumes. Events from  $\beta\beta$ -decay are pure electron interactions (generally called *single site events*, SSE), while significant part of the background signals are induced by multiple-scattered  $\gamma$ -rays (*multi site events*, MSE). However, if a  $\gamma$ -ray scatters only once inside the detector, the signal will be generated by the single scattered electron and thus most likely single-site. On the other hand, always a fraction of electron interactions are MSE. From equation (6) in Section 2.2, it is apparent that for electrons with energies on  $\sim 1$  MeV scale, on average  $\sim 5\%$  of their energy loss in germanium happens via bremsstrahlung radiation. Hard X-rays with a substantial range in germanium can therefore be emitted and subsequently absorbed at another location inside the crystal. Nevertheless, the probability of an emission of a low-energy X-ray with a small range is higher (see Figure 5).

Equation (II-1) in Section 2.3 predicts that the charge induced on the collecting electrode by charge-carrier clusters depends on their positions within the crystal. Thus, by analysing the time development of the charge signal as the charge carriers move towards the electrodes, it is possible to resolve the spatial structure of the interaction. To achieve a good discrimination of MSE and SSE, observable differences must exist between signals from energy depositions at different locations within the detector. From the process of charge collection inside Ge detectors, described in Section 2.3, it is apparent that signals depend strongly on the weighing potential in equation (7). The efficiency of signal discrimination thus crucially depends on the weighing potential shape, which in turn depends on the detector configuration. It is apparent that better discrimination power is achieved with stronger position-dependence of the weighing potential. A pulse-shape analysis on a HPGe detector with a favourable weighing potential will be explored in greater detail in Part II.

For an efficient pulse-shape analysis, the charge pulse must be resolved to fractions of the total charge-collection time. For a typical germanium detector this means that the time resolution of the recorded signal must be on the scale of  $\sim 10$  ns. The time resolution of the recorded pulses is determined by the frequency bandwidth of the preamplifier and other components of the DAQ system. Increasing the charge-collection time can improve the resolution of signal features at a given bandwidth of the DAQ. This can be achieved by reducing the strength of the electric field inside the detector, so it can be advantageous to operate the detector at lower bias voltages (close to the minimum required for the active volume depletion). But too long charge-collection times can sometimes cause ballistic deficit in the signal amplitude, or signal loss due to trapping and recombination, as discussed in Section 2.3.



# I Germanium spectrometry: Monte Carlo simulations for low-level measurement evaluation

## 4. Low-level gamma-ray spectrometry at MPIK

The main goal of low-level  $\gamma$ -ray spectrometry performed at MPIK is the assessment of radiopurity of materials (material screening). Measured samples are mostly candidates for the construction materials to be used in experiments searching for rare events, like the double beta decay experiment GERDA (see Section 3 in the Introduction). The MPIK Low-Level Laboratory (LLL) is located under soil and concrete overburden, corresponding approximately to 15 m of water equivalent. It contains four low-background Ge-spectrometers, each with a coaxial p-type crystal,  $N_2$ -filled sample chamber, active  $\mu$ -veto system and a  $\sim 20$  cm thick shield consisting of Pb, Fe and Cu layers (a description of the newest detector, Corrado, can be found in [66,67]). Two of the detectors can be used for large samples (20 cm x 20 cm x 27 cm). The data-acquisition system used for the measurements consists of charge-sensitive preamplifiers, Canberra model 2022 spectroscopy amplifiers and ND 575 analogue-digital converters with Canberra AIM 556 Ethernet card connected to a PC. Spectra are recorded using the Genie2K<sup>TM</sup> software.

The best obtained sensitivities reach  $< 1$  mBq/kg [47,68]. In cases when a material with even better radiopurity is required, the spectrometers are used for a preliminary selection of candidate samples. A comparison of the laboratory with other GERDA-associated material-screening laboratories can be found in [69].

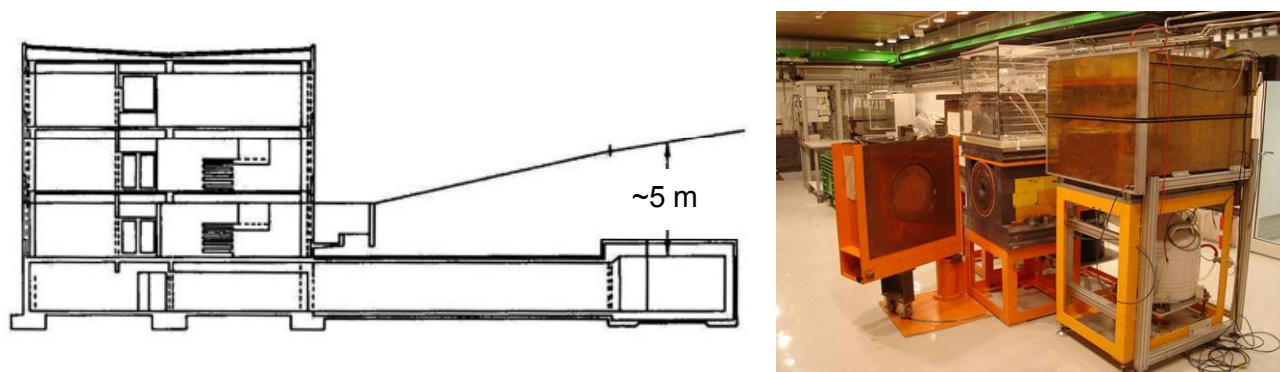


**Figure I-1** Underground location of the Low-Level Laboratory of MPIK (left) and the low-level material screening spectrometers Bruno and Corrado (right).

## 5. Evaluation of material screening measurements

The radioactive content of a sample is determined from the energy spectrum of detected  $\gamma$ -rays using the peaks created by total absorption (full-energy peaks – FEP). Using the count rates in the

regions of interest around the energy of investigated  $\gamma$ -lines, the following equation is used to calculate the activity of the mother isotope:

$$A_{spec.} = \frac{1}{m \cdot \varepsilon} (R_{ROI} - R_{cont.BG} - R_{lineBG}) \quad (I-1)$$

where  $A_{spec.}$  is the specific activity of the sample,  $m$  sample mass,  $\varepsilon$  the FEP detection efficiency and  $R$  the count rate in region of interest ( $R_{ROI}$ ), in continuum background ( $R_{cont.BG}$ ) and line background ( $R_{lineBG}$ ). The count rates in the peak and the continuum background are determined from the measured spectrum as explained in Figure I-2. The second component of the background – the line background, comes from the radiation emitted from nuclides present in the neighbourhood of the detector: mainly the  $^{232}\text{Th}$  and  $^{238}\text{U}$  decay chains and  $^{40}\text{K}$  contamination in shielding materials. To identify this line background for a given sample, a clean material with undetectable contamination and identical properties as the sample (density, shape) has to be measured. This is necessary in order to take into account the effect of the additional background shielding by the sample itself. However, in usual cases such a clean sample is not available. The line background is therefore estimated from measurements of a limited selection of available clean materials (e.g. copper, lead), approximately similar to the sample in terms of density and shape.

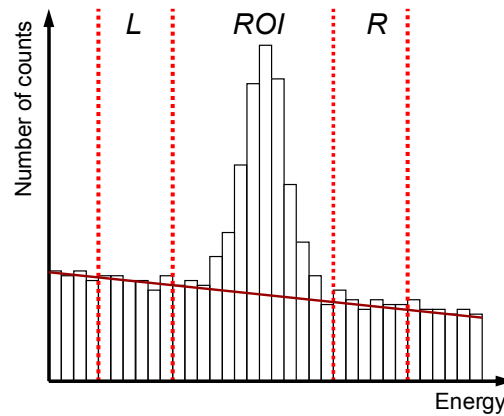


**Figure I-2** Region-of-interest method of determining number of events in a FEP corresponding to a  $\gamma$ -line of interest. Number of counts in the region of interest ( $ROI$ ) normalised to the duration of measurement corresponds to  $R_{ROI}$  in equation (I-1), with  $R_{cont.BG}$  corresponding to the continuum background calculated from the regions  $L$  and  $R$  (normalised to the width of  $ROI$ ).

Monte Carlo (MC) simulations are performed to evaluate the detection efficiency  $\varepsilon$ . The accuracy of efficiency evaluation should give negligible contribution to the overall uncertainty of the measurements. Since the purpose of low-level material-screening measurements is mainly to judge the suitability of materials for low-background applications, high accuracy of results is of less importance than detection sensitivity. The main factor limiting the uncertainty of these measurements is the low event rates, which are often comparable or lower than background rates. Under these circumstances, the requirement on the accuracy of MC simulation is fairly soft. The goal is to keep the relative deviation of the simulated results below  $\sim 10\%$ .

## 6. Monte Carlo code

The MC code used for the efficiency determination is MaGe [70,71], a Geant4-based code [72] developed for the Majorana [37] and GERDA experiments. Geant4 versions 6.02, 8.2p01 and 9.01p02 were used in this work. MaGe uses the low-energy physics package of Geant4. Past studies [73,74] have shown that the simulation of particle transfer through matter by the Geant4 code can be sufficiently accurate, if the available physics models are selected appropriately to the intended application.

However, Geant4 is being continuously developed and minor errors can sometimes be found in the code. In the course of this work, the  $\gamma$ -line intensities in nuclear decays of some isotopes generated by Geant4 version 8.2.p01 were found to differ from the ToRI database [24]. The discrepancy was initially encountered in the decay of  $^{133}\text{Ba}$ . Consequently I have conducted a survey of a range of isotopes, which are of interest for  $\gamma$ -spectrometry, and found more discrepancies. Luciano Pandola of INFN LNGS traced the problem back to the nuclear deexcitation code of Geant4. Three separate bugs were found, which he then formally reported, including the fixes, to the Geant4 Collaboration as bugs # 952, 968 and 970. The fixes were implemented in Geant4.9.1. Table I-1 shows the example of  $^{133}\text{Ba}$   $\gamma$ -line intensities, as generated by Geant4 versions 7.0 and 8.2, and by the latter version after applying the fix. Complete description of the issue and a table of  $\gamma$ -line intensities of 17 radionuclides before and after the fix can be found in [75]. However, some discrepancies still remained unresolved, most notably in the decay of  $^{241}\text{Am}$ .

**Table I-1** Intensities of selected  $\gamma$ -lines of  $^{133}\text{Ba}$ , as provided by the ToRI database [24] and as generated by the radioactive decay module of Geant4.7.0, Geant4.8.2.p01 and the latter code with a fix. Columns labelled *ratio* list ratios between the respective code-generated intensities and the values from ToRI.

E[keV]	ToRI	Geant4.7.0	ratio	Geant4.8.2.p01	ratio	Geant4.8.2.p01 + fix	ratio
79.6	2.62%	2.53%	0.97	2.96%	1.13	2.59%	0.99
81	34.06%	33.71%	0.99	42.87%	1.26	33.36%	0.98
302.9	18.33%	18.01%	0.98	18.39%	1.00	17.97%	0.98
356	62.05%	59.96%	0.97	59.79%	0.96	59.83%	0.96

To further validate the suitability of Geant4 for performing Ge spectrometry simulations, I have participated in a comparison exercise organized by the Gamma-Ray Spectrometry Working Group of the International Committee for Radionuclide Metrology (I.C.R.M.) [76]. This exercise included users of several MC codes commonly used in  $\gamma$ -spectrometry. I have used a Geant4.6.2-based code with the low-energy physics module. The results of participants'  $\gamma$ -ray simulations in simple Ge-detector/sample geometries were compared against each other, without referencing any experimental data.

Good agreement was found between the results from participants using Geant4, PENELOPE [77] and EGS4 [78]. The relative differences between these codes were within 1% at energies above 60 keV and < 1.5% at lower energies. However, the results of Geant3 and MCNP users at energies below 120 keV were significantly deviating from the rest (> 10% at 45 keV). The main reason is thought to be the differences between cross-section data used by these codes developed in 1980's and those used by the more modern codes, like Geant4 and PENELOPE. At energies above

120 keV the results of most of the participants were in good agreement, with relative deviations within a 2%. Overall, the outcomes of this exercise reinforced the confidence in the Geant4-based MaGe as an appropriate MC-simulation tool for use in the evaluation of material-screening measurements.

## 7. Monte Carlo simulations of material-screening detectors

The Geant4 default G4ParticleGun generator was used to produce  $\gamma$ -rays in the simulations. In cases of sources with  $\gamma$ -ray cascades, the Geant4 native radioactive decay module (RDM) was used to generate the unstable nuclei to correctly simulate the coincidence-summing effect. The  $\gamma$ -ray branching ratios in nuclear decays were obtained from the ToRI database and the DDEP database [79]. Most commonly simulated  $\gamma$ -lines in low-background material screening are from the nuclides of the primordial decay chains ( $^{208}\text{Tl}$ ,  $^{212}\text{Pb}$ ,  $^{214}\text{Bi}$ ,  $^{214}\text{Pb}$ ,  $^{228}\text{Ac}$ ) and other natural or man made radioactive contaminants ( $^{40}\text{K}$ ,  $^{54}\text{Mn}$ ,  $^{60}\text{Co}$ ).

MaGe can be run via macros while maintaining high flexibility. Geometries, physics processes, output schemes, etc. are individually adjustable without the need to recompile the code. The efficiency determination simulations make use of a dedicated output class implemented in MaGe, which produces a spectrum of energy deposited in the sensitive volume of a detector during the simulation run, in 1 keV bins. This spectrum is used to calculate the FEP efficiency for the required gamma-lines. The finite resolution of the detector is not reproduced, but the same width of the *ROI* and the background regions (see Figure I-2) as in the measured spectra is used also in evaluating the MC spectra. This helps to counteract possible systematic errors arising from a non-linear continuum background under the peak. Such background can come from the Compton events of the examined  $\gamma$ -line or from other  $\gamma$ -lines from the same isotope, thus it can be reproduced in the MC spectrum.

The geometries of three LLL spectrometers (Bruno, Dario and Corrado) were included in the MaGe code. The models included complete shields, in order to correctly simulate the shape of the Compton-continuum background. Having the full detector shielding in the simulation offers as well the opportunity to further improve the measurement evaluation with the possibility of MC-based determination of the line background. Examples of the software visualisation of Bruno and Corrado are shown in Figure I-3. The software codes for Bruno, Dario and Corrado were written respectively by the author, Michael Hissmann [81] and Werner Maneschg [66].

The basis for the detailed models of the detector structure in close neighbourhood of the crystal was manufacturer information and the design drawings of the crystals and their housings. However, the design drawings of these detectors were more than a decade old, and the detectors underwent several modifications and improvements at the time of their construction. For these reasons the technical information relevant for creating suitable software models was sometimes incomplete or even conflicting. In addition, design drawings and specifications often significantly differ from the real detector [80,82,83] due to:

- 1) limited accuracy of the mounting procedure (causing errors in the distance of crystal to front window and misalignment of the axes of crystal and housing), and
- 2) changes of the sizes of detector components after cooling to cryogenic temperatures.

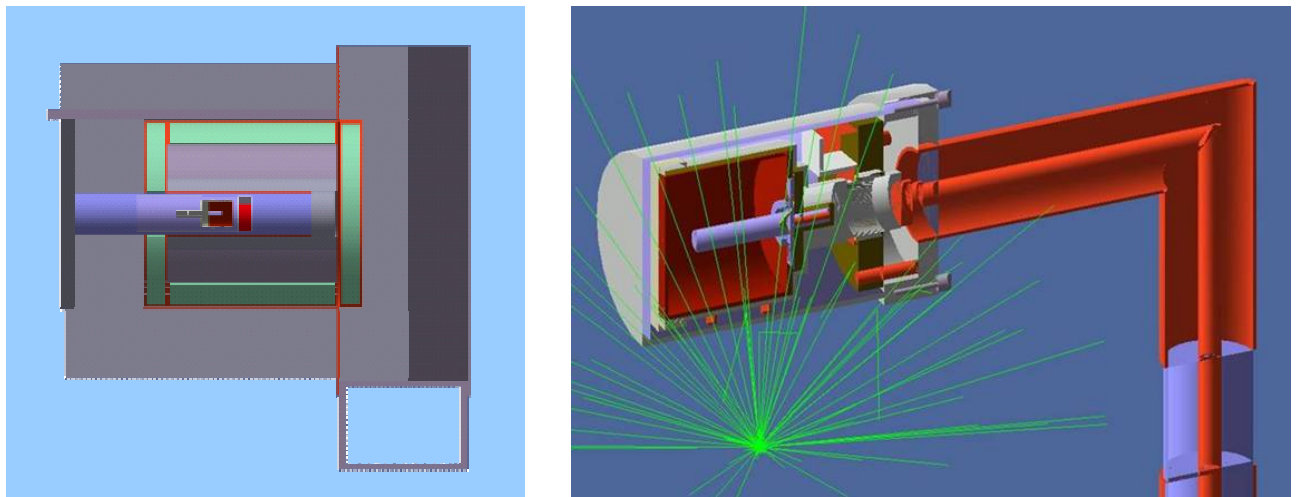


**Figure I-3** Software model cutaway view of the Bruno detector with shielding in MaGe (left) and the cryostat of the Corrado detector model with simulated  $\gamma$ -ray tracks from a low-energy point-like source (right). The software model of Corrado was originally created as a part of this work: [66].

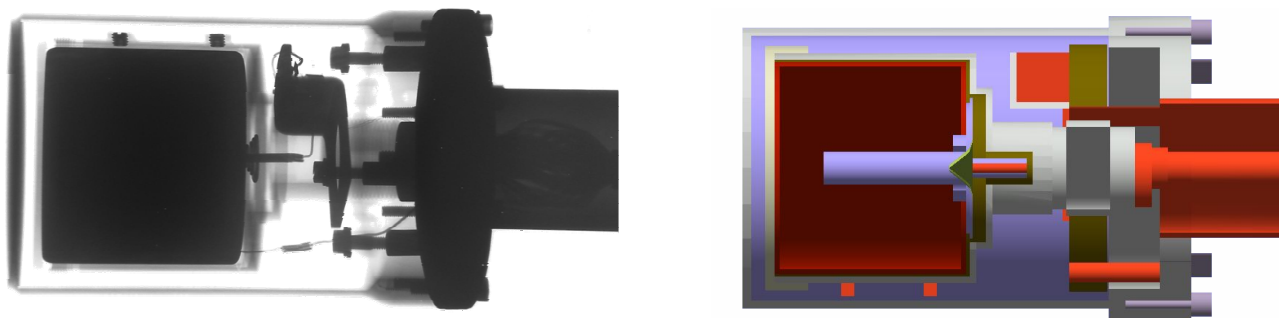


**Figure I-4** A comparison of an X-ray image of the Corrado detector's housing (left) to a cutaway view from the visualisation of the MC software geometry (right). The X-raying was performed with the detector cooled to the operating temperature, and allowed to measure the dimensions and placement of the detector components. However, the dimensions of the inner borehole could not be obtained, as it is barely discernible in the X-ray images.

In case of the newest detector (Corrado), X-ray imaging was done by Hardy Simgen and Mark Heisel. It was performed at the Schweisstechnische Lehr- und Versuchsanstalt Mannheim GmbH. The X-raying allowed to obtain more accurate information on the actual dimensions and placement of the detector components, while cooled to the operating temperature. No misalignment or tilting of the axes of the components was discovered and the rounding of the crystal edges was considered insignificant at our targeted level of accuracy. The X-ray image is compared to the resulting software model in Figure I-4.

Further uncertainties are associated with the insensitive volumes of the Ge diode. The outer dead layer (Li-diffused n+ contact) is typically on the order of 1 mm thick in p-type crystals. The detector geometry parameters supplied by the manufacturer generally don't include accurate measurements of dead layers. Moreover, if the crystal is not cooled to cryogenic temperatures for prolonged periods, the Li diffusion continues and the dead layer grows.

An additional uncertainty is commonly coming from the incomplete charge collection within the Ge crystal [80,84], which is usually not included in MC simulations. This can be important especially in older crystals, which can develop volumes with increased charge-trap concentrations (see

Section 2.3). This can happen due to radiation damage (although this is unlikely in low-background spectrometry) or due to crystal lattice defects, caused e.g. by repeated warming and cooling of the detector. The incomplete charge collection can change the shape of the spectral peaks, which in turn can affect the detector efficiency, depending on the method used for the peak area determination.

Tuning of the dimensions of the detector software model can be performed to determine the unknown geometrical parameters, but also to compensate for any imperfections of MC-simulations (e.g., adjusting active volume can also compensate for small deviations in the interaction cross-sections of germanium, and for charge-collection defects). Hurtado et al. [84], using an n-type Ge crystal, have achieved an accuracy of evaluated efficiencies on the order of 1% with Geant4. A similar optimisation procedure, adapted for a p-type crystal and for a less demanding accuracy requirement, is described in Section 9.

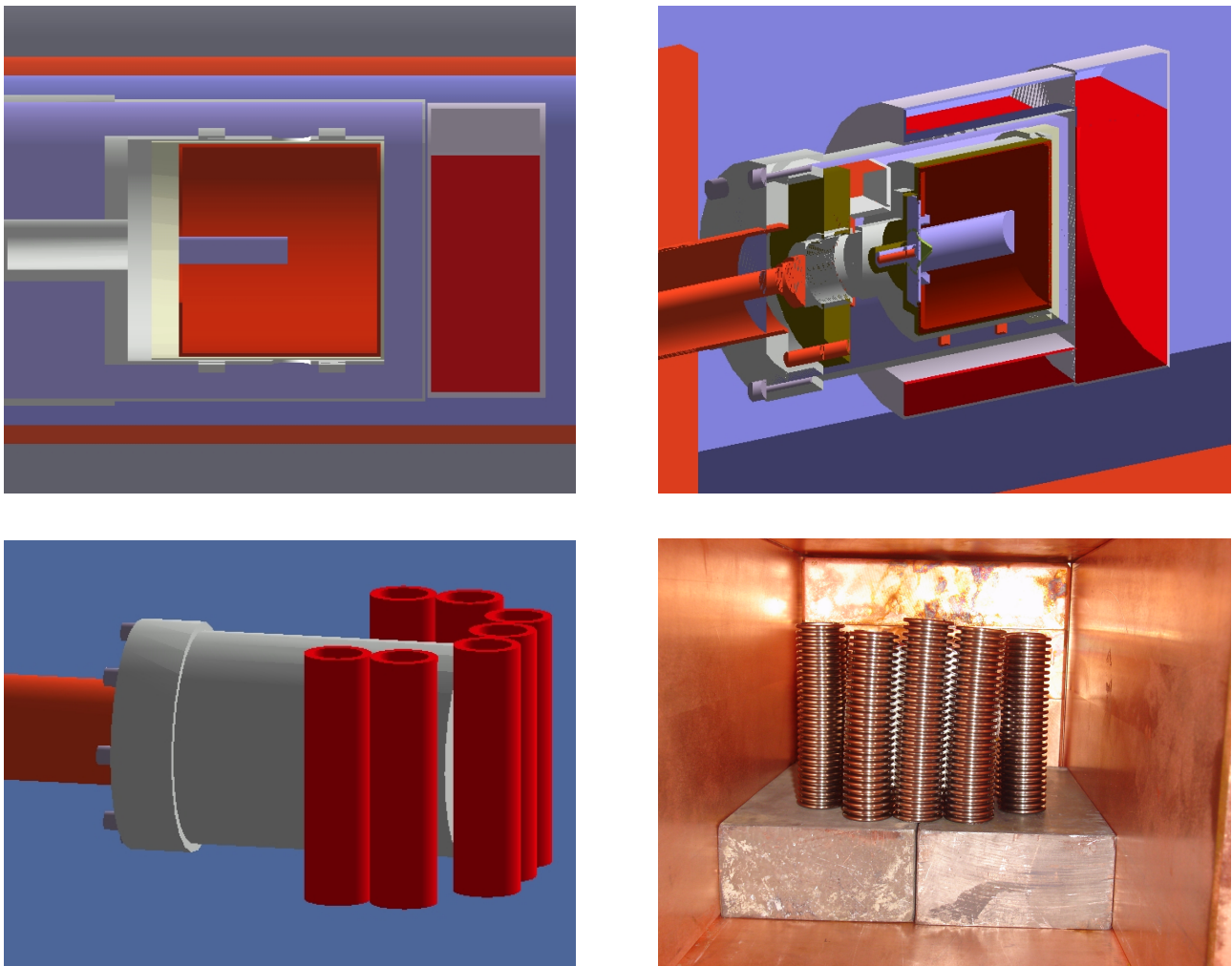


**Figure I-5** **Top:** standard sample geometries selectable in the MaGe macro control system without recompiling the code: a liquid-filled acrylic cylindrical container in front of the Bruno detector (left) and a liquid-filled round Marinelli container placed on the Corrado detector (right). **Bottom:** MaGe model of a non-standard sample shape (left) and a the real sample inside Corrado sample chamber – flexible stainless steel vacuum tubes for the Double Chooz experiment [85] (right).

A set of sample geometries most commonly used in material screening measurements was implemented in MaGe in the course of this work. The macro-based control system of MaGe can be employed to allow simple selection of a specific sample shape and alteration of its material, average density, dimensions and position inside the detector chamber, without recompiling the code. The MaGe simulation tools allow distributing decays randomly in the sample volume of any shape. Examples of some sample geometries are shown in Figure I-5. More sample-specific geometries not included in the standard set can be added in the MaGe, requiring the user to recompile the code.

## **8. Monte Carlo simulation validation with measurements**

This section summarises inter-laboratory comparison exercises and other measurements that were undertaken to test the accuracy of our measurement evaluation, and to validate the use of MC simulations in the evaluation process.

### **8.1. Environmental Radioactivity Comparison Exercise 2005**

This intercomparison study was designed and conducted by the National Physical Laboratory of UK (NPL). Each participant received a sample provided by NPL, and returned the measured radioactivity concentrations of the initially unknown radionuclide content of the sample, within the given deadline. MPIK ordered the low-level  $\gamma$ -emitting sample designated 'GL', which contained radionuclides with activities on  $\sim$ Bq/kg level. NPL analysed and compared the results of all participants, against the reference values determined by NPL with uncertainties ranging from 0.3% to 1% (for the GL sample). More information about the exercise and the general results can be found in the NPL report [86].

#### **8.1.1. Comparison of GERDA laboratories**

MPIK Heidelberg, as well as the Institute for Reference Materials and Measurements (IRMM), Geel, participated in the NPL exercise. IRMM participated also in the high activity part of the study ('GH' sample with activities on  $\sim$ Bq/g level). Additional comparison was performed within the GERDA collaboration, which included also the Joint Institute for Nuclear Research (JINR), Dubna, and the Laboratori Nazionali del Gran Sasso (LNGS), Assergi. The samples used in this comparison were those received by the two institutes that participated in the NPL exercise. None of the laboratories involved had a prior knowledge of the radioisotopic content of the sample. The measurements and evaluations were performed by the material screening teams of the individual institutes.

IRMM received from NPL two low-activity (GL) samples (B05221 and B05223) and a high-activity (GH) sample (B05146). The measurements were performed in an above-ground low-level laboratory in Geel, Belgium, using a low-background coaxial p-type crystal. The GL sample number B05221 was measured in its original container with 500 g of liquid, and the GH sample in a standard container used for screening at IRMM.

JINR received from IRMM sample B05223 with a mass of 500 g (in the original container). The measurement was performed in an above-ground laboratory in Dubna with a passively shielded n-type coaxial crystal. The same sample was later measured also by the IGEX/Baksan detector setup

(with two p-type crystals), located at a depth of 660 m of water equivalent in the Baksan Neutrino Observatory (BNO).

MPIK received from NPL a GL sample number B05200. For the measurement, a part of the sample solution was refilled into an acrylic measurement container with a content of 109 g ('Fraction 1'). It was then measured with two detectors in LLL (Bruno and Dario). Apart from that, 127 g of the solution was refilled into a small PTFE bottle ('Fraction 2').

The leftover of the sample solution number B05200, in its original bottle, was then sent to LNGS. At LNGS, 124 g of the solution was refilled into an acrylic measurement container ('Fraction 3') and measured with a coaxial p-type crystal (GeMI detector).

### 8.1.2. Results

All four laboratories correctly identified all 10 isotopes present in the sample without any false identification. From the measured activities of individual isotopes, relative deviations with respect to the reference values were calculated. The results from MPIK are shown in Figure I-6 and the average results from each laboratory are listed in Table I-2, along with the MC codes used in the evaluation. A complete report of the comparison of GERDA Laboratories can be found in [58].

**Table I-2** Mean results of a comparison of GERDA laboratories. The values were calculated for each isotope and  $\gamma$ -line using the formula:  $Deviation = (A - A_{REF}) / A_{REF}$ , and then averaged for each laboratory. The uncertainty of *Mean Deviation* is represented by the RMS deviation of obtained values.

Institute	Efficiency Calculation	Sample	Mean Deviation [%]
IRMM	EGS4	B05221 <sup>a</sup>	1.7 (16) <sup>a</sup>
		B05146	1.3 (11)
JINR	Geant4.7.0	B05223	-19.9 (35)
BNO	Geant4.7.0	B05223	-17.6 (34)
MPIK	MaGe (Geant4.6.02)	B05200 Fraction 1	-19.2 (65) <sup>b</sup>
			-18.9 (73)
LNGS	Geant4.7.0	B05200 Fraction 3	-2.0 (68) <sup>c</sup>

<sup>a</sup> top value is for the GL sample; bottom value is for the GH sample

<sup>b</sup> top value is for the Dario detector; bottom value is for the Bruno detector

<sup>c</sup> excluding the value for <sup>95</sup>Nb

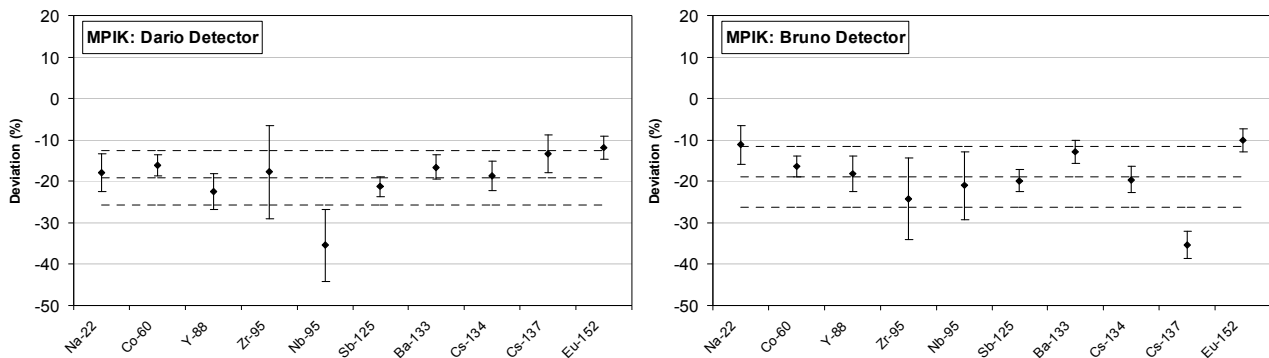


**Figure I-6** Relative deviations of measured activities with respect to the NPL reference, calculated with the formula:  $Deviation = (A - A_{REF}) / A_{REF}$ . Error bars represent the statistical uncertainty. The dashed lines are the mean of the deviations with the corresponding standard deviation.

As can be seen from the table, the results from MPIK as well as those from JINR and BNO exhibited differences of almost 20%, relative to the reference values provided by NPL. This discrepancy was similar for both detectors at MPIK. The results from IRMM and LNGS on the other hand were essentially consistent with the reference activity, except for an anomalous result for  $^{95}\text{Nb}$  in LNGS.

### 8.1.3. Additional investigation

Further measurements were performed to search for the cause of these discrepancies. A measurement of the Fraction 1 of the sample B05200, which was measured earlier at MPIK, was carried out at LNGS. The evaluation at LNGS was done in the same way as with the previous measurement of the Fraction 3 of the sample. The results, displayed in Figure I-7, show good agreement with the results previously measured at MPIK, with mean relative difference between them equal  $(-2.0 \pm 3.9)\%$  and  $(-0.2 \pm 6.2)\%$ , respectively for Dario and Bruno detectors. This result thereby confirms the previous evaluation done at MPIK. The different results from measurements of Fraction 1 and Fraction 3 suggest that the two fractions did indeed have different activity contents.

I have continued the investigation with additional measurements of other parts of the 500 g B05200 sample. This included the 127 g Fraction 3 in a small PTFE bottle, and the remainder of the sample (135 g, 'Fraction 4'), left in the original polyethylene bottle. This was measured in the two detectors at MPIK. The summary of all measurements of this sample is given in the plot on Figure I-7.

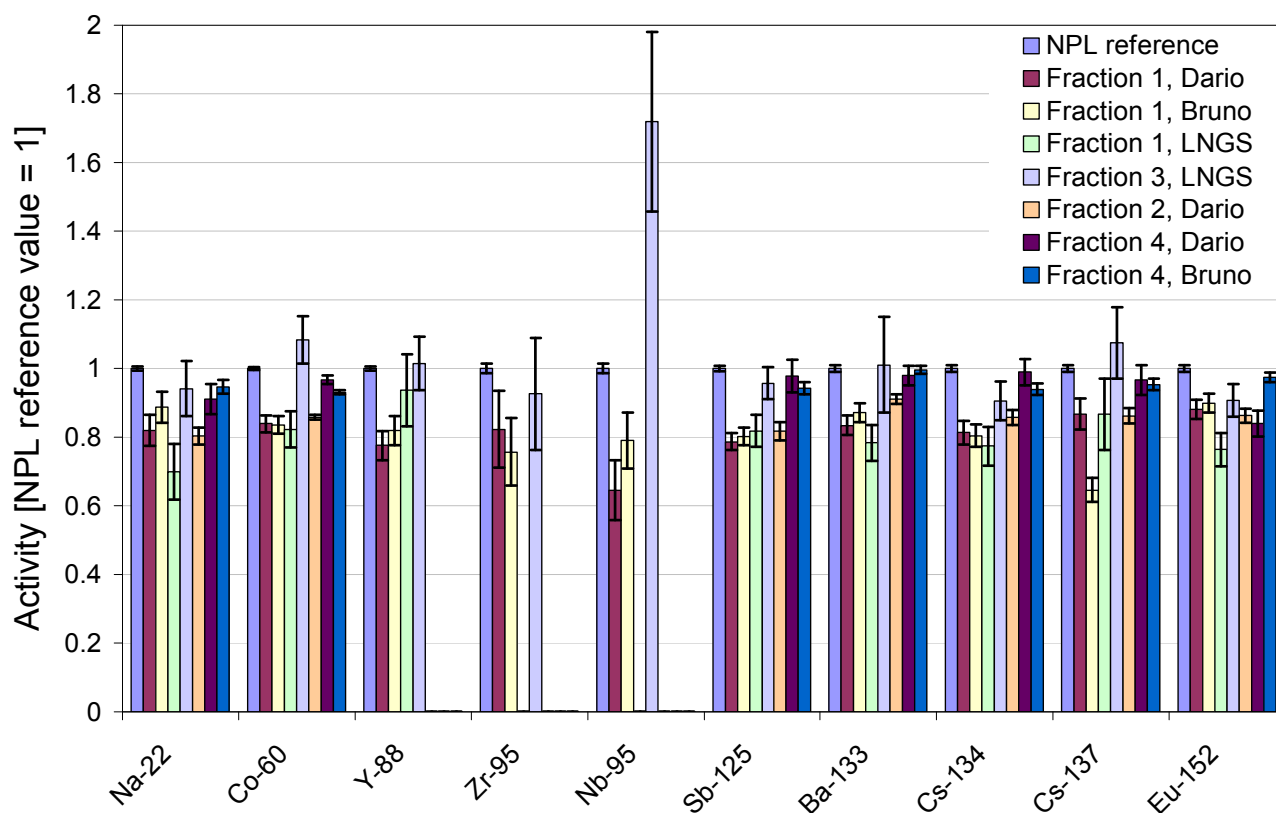


**Figure I-7** Summary of the measurements of all fractions taken from the sample B05200, compared to the NPL reference value. The measurement of Fraction 1 in Dario was done and evaluated by Mark Heisel. The measurements of Fractions 1 and 3 performed at LNGS were done and evaluated by Matthias Laubenstein.

In addition, I measured the emptied polyethylene bottle, in which the sample was originally delivered, to test the hypothesis that metal ions of the radioactive isotopes could stick to the walls. The consequent inhomogeneous distribution after refilling of the liquid was viewed as a potential explanation of the observed discrepancies of the measurements. However, only  $^{22}\text{Na}$  was detected in the empty bottle, on level of  $(1.3 \pm 0.7)\%$  of the reference activity. This is not sufficient to be the only cause for the disagreements.

#### 8.1.4. Discussion

It is difficult to draw specific conclusions about each of these measurements, but the comparison of all results allows some general observations. From the presented plot it can be seen that measuring the same identical sample on different detectors gave matching results. This applies also in the case of the Fraction 1, measured and evaluated (including independent MC simulations) in two different laboratories. On the other hand the measurements of different fractions taken from the original sample were in disagreement with each other. In addition, further simulations of various  $\gamma$ -ray sources, which will be presented in Section 8.3, show that the software models of both detectors employed in this study most likely did not significantly contribute to the deviations of the results. When the comprehensive consistency and homogeneity checks, claimed to be performed by NPL in preparation of the sample solutions [86], are taken into consideration, the dominant source of the discrepancy can only be related to the refilling of the samples into different bottles.

Still, it is intriguing to note that also the results from the sample B05223 measured in Dubna and Baksan hold discrepancy similar to the measurements of Fraction 1. This is more complicated to explain, because these two samples are independent from each other. However, the investigation of the causes of this discrepancy was not pursued further, since the material-screening team of BNO and JINR considered the MC results with 20% deviation as sufficiently accurate.

## 8.2. Environmental Radioactivity Proficiency Test Exercise 2007

In the first half of 2007 we participated in another intercomparison organized by the National Physical Laboratory. The layout of the exercise was the same as with the comparison from 2005. A new feature was the availability of a neutron activated crushed concrete sample. It contained a variety of radionuclides with concentrations up to 1 Bq/g. The MPIK ordered the low-activity liquid sample containing gamma emitters (GL) and the concrete sample. The concrete contained as well beta emitters, which were not evaluated due to the lack of appropriate detectors in LLL.

The newest spectrometer in LLL, Corrado, was used for the measurements. Several steps were taken in order to improve on the results submitted in the previous NPL exercise. The samples (Figure I-8) were first measured in their original containers, to exclude any uncertainties associated with the refilling process. However, the concrete sample had to be later refilled into a cylindrical acrylic container, due to difficulties to accurately model the geometry of the powder in the original bottle. The shape of the liquid-sample bottle was reproduced in detail in the MC-simulation code. The detector geometry was modelled with added information from the X-ray scans and a preliminary detector-model optimisation was performed (finalised version of the optimisation method is presented in Section 9). The evaluation procedure was adjusted to account for the different binning and resolution of data in the ADC output of the detector and the output of MC simulation, by

selecting always the same width of the peak and background regions both in the measured and simulated spectra.

Comparison of the submitted results to the NPL reference values is displayed in the Figure I-9. The full results of the exercise were reported in [87]. Compared to the 2005 exercise, our results have improved, although the discrepancies were still larger than 10%. The preliminary optimisation performed before evaluating the results of this exercise gave only a very crude estimation of the dead layer and borehole of the crystal. As is shown in the Section 9, these parameters have a great impact on the detection efficiency. Therefore it can be inferred that the inexact geometry of the detector software model is responsible for large part of the discrepancy in this case, as opposed to the deviations in the 2005 results, which were attributed to sample-handling difficulties, as discussed in the Section 8.1.4.



**Figure I-8** Samples measured at LLL in the Corrado detector as part of the Environmental Radioactivity Proficiency Test Exercise 2007. The crushed concrete sample in a small acrylic box (left), the low-activity  $\gamma$ -emitters solution (GL sample) in it's original bottle (middle) and geometrical model of the bottled sample implemented in MC code (right).

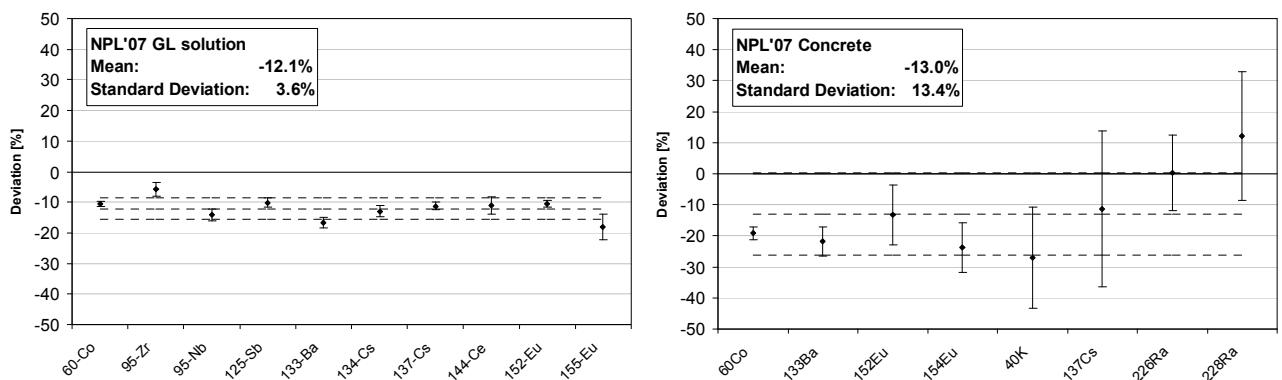


**Figure I-9** Relative deviations of measured activities with respect to the NPL reference. The values are calculated as  $Deviation = (A - A_{REF}) / A_{REF}$ . Error bars represent the statistical uncertainty. The dashed lines are the mean of the deviations with corresponding standard deviation. Both samples were measured with the Corrado detector.

### 8.3. Assessment of Bruno and Dario software models

To assess how accurately the MaGe simulations of the LLL detectors are able to reproduce spectrometric measurements, several point-like and extended  $\gamma$ -ray calibration standards were simulated. This sub-section summarises the comparisons performed with the Bruno and Dario detectors. Certificates of the point-like sources produced around the year 1970 are not available anymore. Comparing two old  $^{137}\text{Cs}$  sources measured at the same position, the corresponding efficiencies were found to differ by  $\sim 6\%$ , which exceeds the expected 3% nominal uncertainty of their activities (68% confidence). To take into account the reduced trust in the nominal source activities, 6% relative uncertainty was assigned to the activity of these sources. In the case of an IAEA set from 1970, information about the source housings is missing. These sources are encased in aluminium covers with unknown thickness, which had to be considered in the MC simulations.

The extended sources included in the comparisons were the  $^{226}\text{Ra}$  and  $^{228}\text{Th}$  samples, prepared in-house from purchased standard solutions, and samples from the IAEA Proficiency Test 2006 [88]. The latter ones included a water solution, grass and soil sample. The grass and soil samples were difficult to model due to complicated composition and incoherent shape.

The relative differences between FEP efficiencies calculated by the MC simulations and efficiencies derived from the known activity of measured point-like standards are listed in Table I-3. Table I-4 contains the results of extended sources measurements. In the calculation of the deviations, the daughters of  $^{226}\text{Ra}$  ( $^{214}\text{Pb}$  and  $^{214}\text{Bi}$ ) were assumed to be in a secular equilibrium with the parent isotope.

In addition to comparing the FEP efficiencies, I performed also comparisons of the Compton continua of the measured and simulated data. Example spectra are shown in Figure I-10. The agreement between the data from the detector ADC and the MC simulation is very good in most of the Compton continuum for the point like  $^{60}\text{Co}$  source as well as for the extended  $^{228}\text{Th}$  sample. For MC simulations with completely reproduced measurement geometry, average deviations between the Compton continua of the measured and simulated spectra were within 10%.

From the Tables I-3 and I-4, it can be seen that deviations greater than 10% occurred in the results. The largest deviations occurred in the simulations of low-energy gamma sources, like  $^{241}\text{Am}$ ,  $^{109}\text{Cd}$  and  $^{210}\text{Pb}$ . This probably resulted from inaccurate knowledge of the thickness of the dead-layer or other components of the detectors. The relatively small difference between the two  $^{241}\text{Am}$  sources from different IAEA sets suggests that the Al housing thickness of the 1970 source was deduced reasonably correctly.

The results in the energy range above  $\sim 100$  keV agree mostly within the required precision limits. The measurements of  $^{22}\text{Na}$  and  $^{54}\text{Mn}$  point-like sources show a distance dependence of the deviation, well above the statistical uncertainty. This leads to a suspicion that the position of the crystal inside the Bruno detector is not represented exactly in the simulation, but the effect is within reasonable limits. The large discrepancies in the results of  $^{214}\text{Pb}$  and  $^{214}\text{Bi}$  in the Ra-solution and Cu-gel samples are most likely caused by the commonly occurring problem of  $^{222}\text{Rn}$  gas escaping from the sample. The assumption that the daughters of  $^{226}\text{Ra}$  in the solutions are in secular equilibrium is thus probably false.

**Table I-3** Simulation to measurement comparisons of point-like sources. The values were calculated for each isotope and  $\gamma$ -line as  $RD = (\varepsilon_{MC} - \varepsilon_{exp}) / \varepsilon_{exp}$ . Uncertainties include the source activity errors and the statistical uncertainties.

Detector	Source	Geometry Description	Energy [keV]	RD [%]
Bruno	<sup>241</sup> Am, IAEA 1966	at detector window	59.5	-54.6 (27)
		3 cm from detector	59.5	-46.9 (32)
	<sup>241</sup> Am, IAEA 1970	at detector window	59.5	-51.2 (29)
		3 cm from detector	59.5	-43.9 (34)
	<sup>137</sup> Cs, IAEA 1966	6 cm from detector	662	-0.8 (60)
	<sup>54</sup> Mn, QSA 1999	at detector window	835	-8.4 (29)
		6 cm from detector	835	2.7 (32)
	<sup>22</sup> Na, IAEA 1970	at detector window	1275	-1.7 (61)
		3 cm from detector	1275	4.7 (66)
	<sup>60</sup> Co, IAEA 1970	6 cm from detector	1172	0.6 (62)
1333			5.2 (64)	
<sup>228</sup> Th, QSA 2006	16 cm from detector	2615	7.6 (20)	
Dario	<sup>137</sup> Cs, IAEA 1966	3 cm from detector	662	2.7 (62)
		7 cm from detector	662	1.3 (61)

**Table I-4** Simulation to measurement comparisons of extended sources performed with the Bruno and Dario detectors. The values were calculated for each isotope and  $\gamma$ -line as  $RD = (\varepsilon_{MC} - \varepsilon_{exp}) / \varepsilon_{exp}$ . Uncertainties include the source activity errors and the statistical uncertainties. Measurements and simulations of the IAEA samples were carried out under the supervision of the author by Sarah Heim as a part of her internship at MPIK.

Detector	Sample Description	Isotope	Energy [keV]	RD [%]
Bruno	<sup>226</sup> Ra solution in a cylindrical container	<sup>226</sup> Ra	186	-5.9 (49)
		<sup>214</sup> Pb	242 - 352	25.0 (41) <sup>a</sup>
		<sup>214</sup> Bi	609 - 2204	29.8 (95) <sup>a</sup>
	Mixture of Cu and gel with dissolved Ra in a cylindrical container	<sup>226</sup> Ra	186	-7.9 (13)
		<sup>214</sup> Pb	242 - 352	36.2 (13) <sup>a</sup>
		<sup>214</sup> Bi	609 - 2204	35.9 (67) <sup>a</sup>
		<sup>212</sup> Pb	239 - 300	6.0 (39) <sup>a,b</sup>
		<sup>212</sup> Bi	727	10.4 (52) <sup>b</sup>
	<sup>228</sup> Th solution in a cylindrical container		277	10.2 (44) <sup>b</sup>
		<sup>208</sup> Tl	583	8.7 (29) <sup>b</sup>
			861	9.4 (18) <sup>b</sup>
			2615	15.1 (15) <sup>b</sup>
		<sup>210</sup> Pb	46.5	-30 (44)
		<sup>241</sup> Am	59.5	-39.7 (23)
	IAEA Proficiency Test 2006 soil sample in a cylindrical container	<sup>109</sup> Cd	88	-48.1 (29)
		<sup>137</sup> Cs	662	2.6 (23)
		<sup>134</sup> Cs	796	-1.9 (30)
		<sup>54</sup> Mn	835	1.0 (24)
		<sup>65</sup> Zn	1116	6.2 (39)
<sup>60</sup> Co		1172 - 1333	5.17 (17) <sup>a</sup>	
<sup>137</sup> Cs		662	6.9 (18)	
IAEA Proficiency Test 2006 grass sample in a cylindrical container	<sup>40</sup> K	1461	10.2 (34)	
	<sup>241</sup> Am	59.5	-55.3 (43)	
Dario	IAEA Proficiency Test 2006 water solution in a PE bottle	<sup>109</sup> Cd	88	-9.6 (97)
		<sup>137</sup> Cs	662	-3.05 (92)
		<sup>134</sup> Cs	605 - 1365	-3.5 (29) <sup>a</sup>
		<sup>54</sup> Mn	835	1.0 (21)
		<sup>65</sup> Zn	1116	-1.9 (31)
		<sup>60</sup> Co	1172 - 1333	2.2 (15) <sup>a</sup>

<sup>a</sup> weighted average of the deviations of individual  $\gamma$ -lines of the isotope, with RMS uncertainty. The average is reported only in those cases where the individual  $\gamma$ -line deviations did not exhibit any noticeable dependence on  $\gamma$ -ray energy.

<sup>b</sup> the values for the <sup>228</sup>Th sample are the weighted averages of results from two independent measurements, with RMS uncertainty.

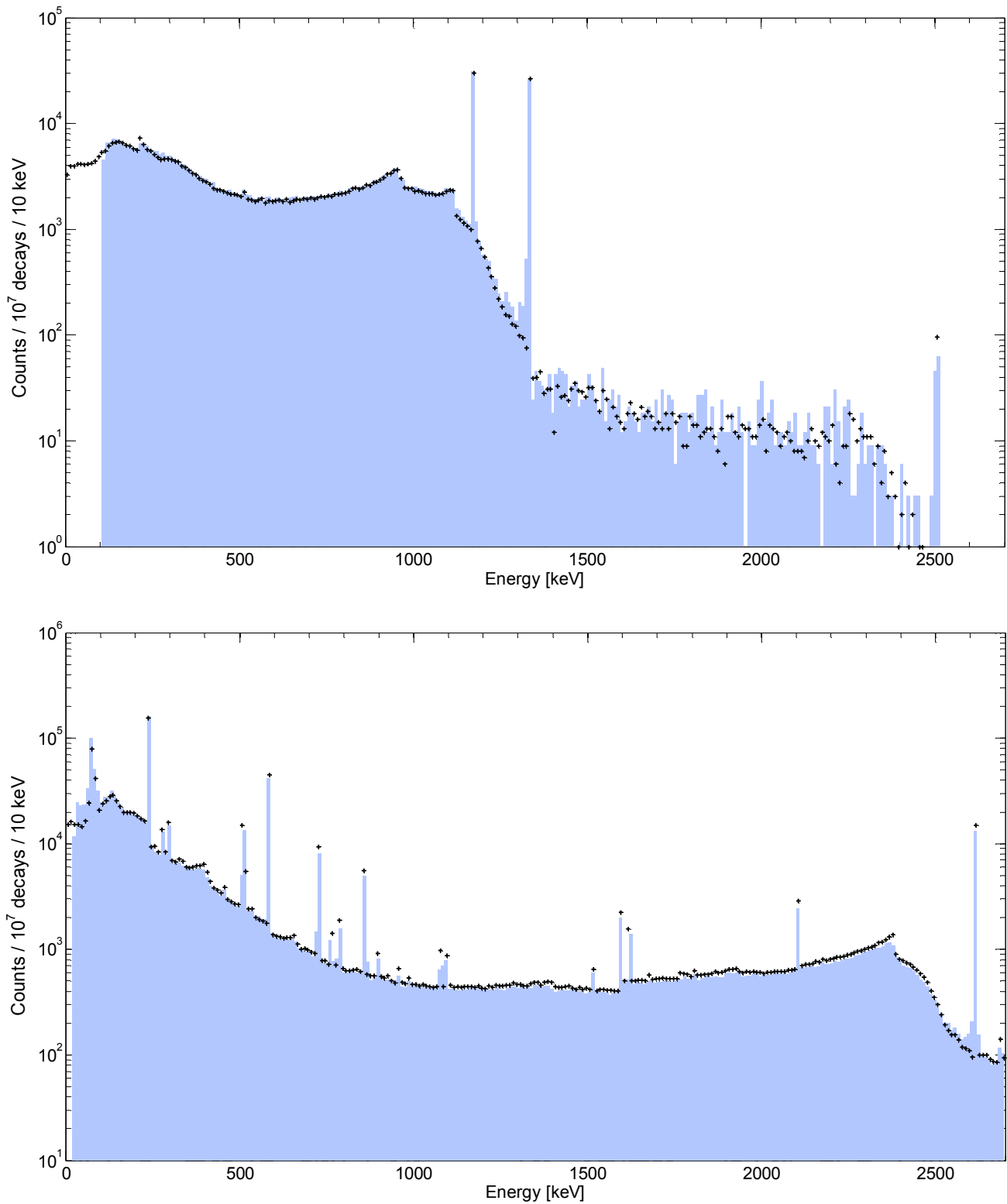


**Figure I-10** A comparison of measured and simulated spectra of a <sup>60</sup>Co point-like source (top) and an extended <sup>228</sup>Th sample (bottom), measured with the Bruno detector. The measured data are indicated by the blue area, and the MC simulated spectra by the black points.

Both in point-like and extended source comparisons performed with Bruno, the results from the highest energy  $\gamma$ -line measured (2.6 MeV from <sup>208</sup>Tl) show a higher discrepancy, as compared to the results in lower energies. The detection efficiency of higher-energy gammas is more sensitive to

errors in the size of active volume of the detector. This could indicate that the inner hole or outer dimensions of the Bruno crystal are not modelled accurately.

The results from both point-like and extended sources are mostly in agreement with each other, implying that the extended sources were modelled with sufficient accuracy. Among the most difficult sources to model was the grass sample from IAEA. Its geometry was greatly simplified, represented in simulation by a homogeneous material. Nevertheless, even in this case the result shows discrepancy only on the order of  $\sim 10\%$  or less.

Except for the very low energy lines, the results of the performed simulations show rather good agreement with the results of measurements. It applies both to count rates in peaks, as well as in the Compton continua (see Figure I-10). This demonstrates that careful modelling of the detector and sample geometries can ensure reliable outcomes of MC-based efficiency determination. Detector dead-layer and active-volume optimisation, similar to that described in following section, could be performed to further improve the results also in the lowest and highest parts of the energy spectrum.

## 9. Optimisation of the software model of Corrado spectrometer

The purpose of this effort was to reach an accuracy of efficiency evaluation that would give a negligible contribution to the overall uncertainty of the measurements. In Section 5, this requirement was estimated to be approximately  $< 10\%$ . A report of this optimisation study is given in [89]. The optimization procedure was defined specifically for a p-type crystal configuration. The Corrado detector was used for this study, and X-ray imaging was performed to obtain information on the actual dimensions and placement of detector components, while cooled to the operating temperature. The information that couldn't be verified from the X-raying was the thickness of the dead layer and the dimensions of the inner borehole, which is barely discernible in the X-ray images. A drawing of the detector with the relevant geometry parameters is shown on Figure I-11. The outer dimensions of the Ge crystal obtained from X-ray images were considered sufficiently accurate. Only the outer dead layer and the detector borehole were refined by matching the MC simulations to the  $\gamma$ -ray source measurements.

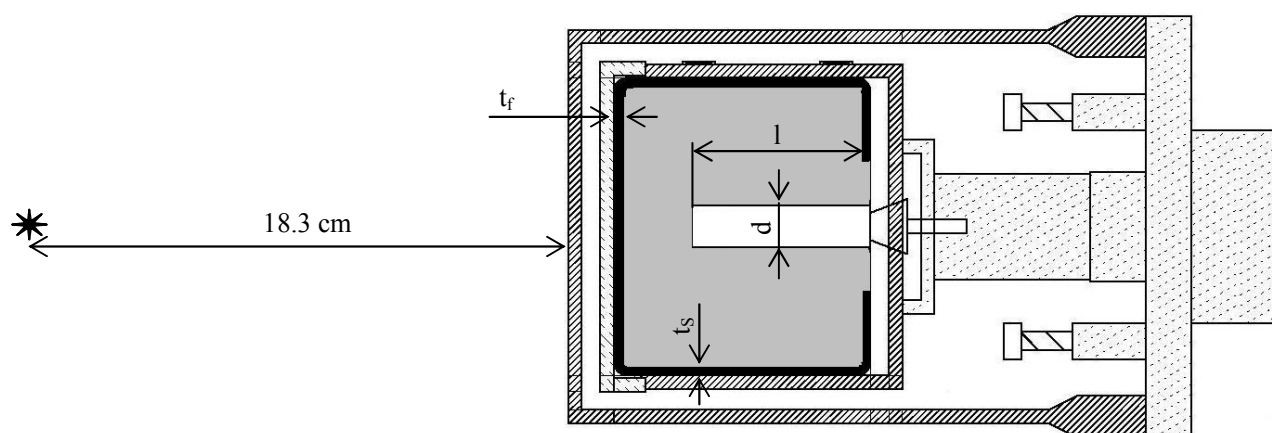


**Figure I-11** Schematic drawing of the detector geometry. The relevant dimensions subjected to optimisation are: front dead-layer thickness  $t_f$ , side dead-layer thickness  $t_s$ , borehole length  $l$  and borehole radius  $d$ . Reference source position used in the final comparison in Table I-6 is indicated by the star.

## 9.1. Experimental measurements

To provide experimental reference for the MC simulations, I measured several point like  $\gamma$ -ray calibration standards, including following sources (reference time 24.5.2007):  $^{241}\text{Am}$ , Buchler 1969,  $(310 \pm 19)$  kBq;  $^{133}\text{Ba}$ , IPE / PTB 2007,  $(101 \pm 1.5)$  kBq;  $^{137}\text{Cs}$ , Buchler 1969,  $(166 \pm 10)$  kBq;  $^{54}\text{Mn}$ , QSA 1999,  $(960 \pm 30)$  Bq;  $^{60}\text{Co}$ , IAEA 1970,  $(2872 \pm 172)$  Bq;  $^{228}\text{Th}$ , QSA 2006,  $(8.71 \pm 0.13)$  kBq. The sources were placed at distances ranging between  $(3 - 18)$  cm in front of and below the detector housing. Radiation from the sources was not collimated, in order to obtain information about the average value of the dead layer and borehole. The uncertainty in positioning the sources was estimated to be approximately 1 mm in distance from the detector, and about 2 mm to 5 mm in lateral position (increasing with distance from the detector). The count-rate variation corresponding to the position uncertainties was computed using MC simulations, and taken into account in the uncertainty budget of the results. In case of sources close to the detector the position uncertainty could create up to 3% change in count rate, in case of sources in greater distances it had a smaller effect ( $< 1\%$  at 18.3 cm from detector). The dead times in the measurements of the high-activity  $^{241}\text{Am}$  and  $^{133}\text{Ba}$  reached sometimes values of up to 4%, respectively 8%. At such high rates, the automatic dead-time correction of the data acquisition system might deviate from the true dead-time value. However, this did not affect the final dead-layer evaluation, as explained in the next section.

## 9.2. Dead layer thickness determination

The first step of the evaluation was to determine thickness of the dead layer at the front side of the Ge diode. The procedure included the measurements of 59.5 keV, 99 keV and 103 keV lines of  $^{241}\text{Am}$ . The source was positioned on the detector axis, 18.3 cm in front of the detector end-cap. The 99 keV and 103 keV  $\gamma$ -lines have very low intensity (0.0203% and 0.0195% emission probabilities respectively), but with a several-hour measurement of the 300 kBq  $^{241}\text{Am}$  source, sufficient statistics were acquired ( $> 10^5$  net counts in each peak) to allow their use in the evaluation. The separation of these two  $\gamma$ -lines was comparable to the energy resolution of the detector, thus all calculations were done with the sum of the counts in the two peaks.

MC simulations with varying dead layer values were performed and the full-energy-peak (FEP) efficiencies were calculated in each case for each of the three  $\gamma$ -ray energies. From the simulated and measured FEP efficiencies, the following ratio was calculated:

$$R = \varepsilon_{59} / (\varepsilon_{99} + \varepsilon_{103}) \quad (\text{I-2})$$

where  $\varepsilon$  represents the FEP efficiency at the energy specified in the subscript. As illustrated in Figure I-12, the MC-derived ratio  $R$  is an exponential function of the dead layer thickness (indicated in the plot by the black line connecting the red MC data points). By interpolating the acquired exponential dependency to the ratio  $R$  obtained from the measurement (blue horizontal line), the thickness of the dead layer was determined (blue vertical line).

The same procedure was used to determine the dead layer at the cylindrical side of the crystal. The source was placed 5.6 cm below the detector housing. A comparison of the nominal and optimised values is shown in Table I-5. The statistical uncertainty of the measurement, the uncertainties arising from FEP fitting and from the exponential fit to the MC data were taken into account in calculating the uncertainty of the optimised dead layer thickness.

This method of determination came out to be very sensitive, mostly due to the low energy of the involved  $\gamma$ -lines, and due to the fact that it uses the ratio  $R$  instead of the absolute detection efficiency. This eliminates the uncertainties arising from the source activity and position, and from the measurement time (which can be affected by an imperfect dead-time correction). In addition, due to their short range in Ge, these low-energy gammas are not affected by the dimensions of the crystal borehole (which were unknown at this stage of the optimisation). The outer dimensions of the detector were fixed from the X-ray imaging, and their uncertainty was not taken into account in the dead layer evaluation. The thickness of the dead layer was assumed to be uniform along the circumference of the cylinder. However, the optimised dead layer does not necessarily reflect the real dead layer of the detector, but rather a parameter of the MC-software representation of the detector geometry. By optimising this parameter, one compensates also for the errors in the thicknesses of the detector end-cap and other layers of material between the crystal and the surface of the housing.

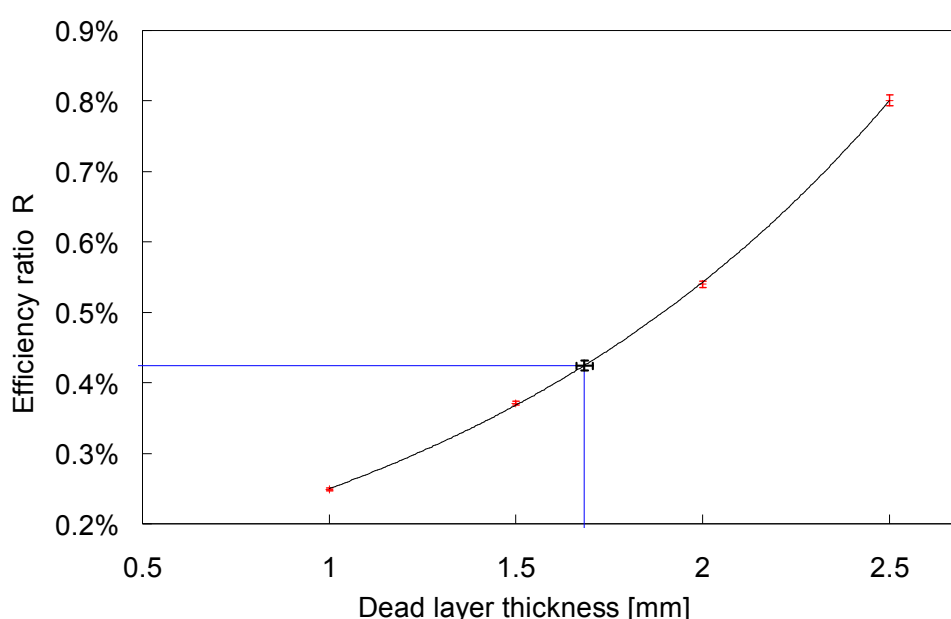


**Figure I-12** Front dead-layer thickness interpolation from the results of MC simulations (red data points). The vertical error bars of the MC values and of the measurement result (black) include statistical and FEP-fitting uncertainties. The interpolated dead-layer thickness (black horizontal error bar) additionally includes the uncertainty of the exponential fit.

### 9.3. Detector active volume determination

In the next step of the optimisation process, the active volume of the detector model was adjusted by changing the dimensions of the crystal borehole. After the dead layer thickness was fixed, the borehole dimensions remained the only undetermined parameters affecting the  $\gamma$ -line efficiencies at energies of a few hundreds keV and higher. FEP efficiencies were calculated from measurements of  $^{137}\text{Cs}$ ,  $^{54}\text{Mn}$ , and  $^{60}\text{Co}$  at several positions around the crystal. Subsequently, MC simulations were performed with varying dimensions of the hole. Starting points were the nominal values from design drawings and in each step both the radius and the length were incremented by 1 mm. For each isotope and source position, the optimal active volume was obtained by linear interpolation of the MC results. An example of the active volume determination performed with a  $^{54}\text{Mn}$  source

placed at 18.3 cm distance in front of the detector end-cap is shown in Figure I-13. The black line is the linear fit applied to the MC results. The experimentally measured efficiency is indicated by the blue horizontal line and the corresponding interpolated active volume by the blue vertical line.

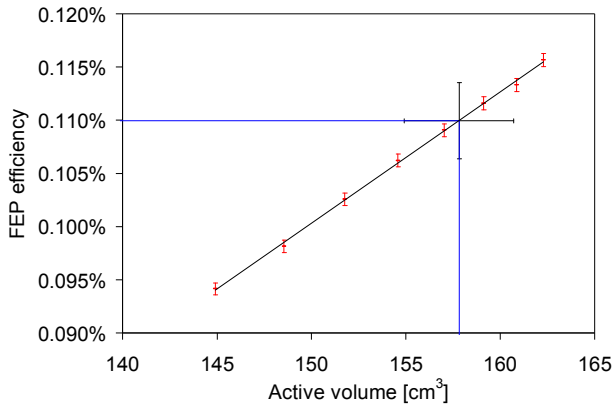


**Figure I-13** An example of active volume interpolation from the FEP efficiency of the 835 keV  $\gamma$ -line of  $^{54}\text{Mn}$ . The vertical error bars of the MC data points (red) represent statistical uncertainties, the measured FEP efficiency includes also the uncertainty of the source activity and the source position (black vertical error bar). The interpolated active volume additionally includes the uncertainty of the linear fit (black horizontal error bar).

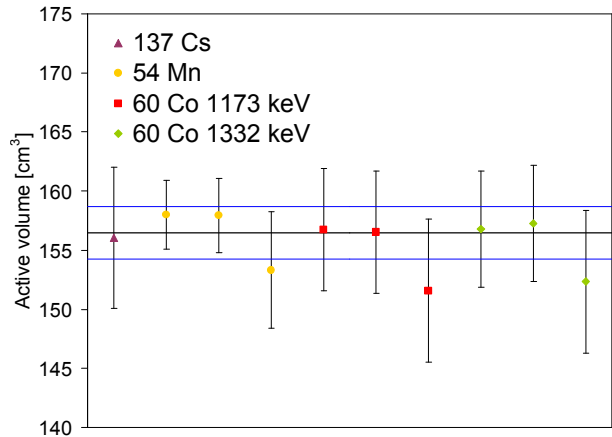


**Figure I-14** A summary of active volume results from different measurements, each obtained analogously to the method depicted in Figure I-13. The error bars include statistical as well as activity, position and fitting uncertainties. The horizontal line is the weighted average of the results and the blue lines represents the interval corresponding to the RMS deviation of the results.

The resulting active volumes obtained from the  $^{137}\text{Cs}$ ,  $^{54}\text{Mn}$ , and  $^{60}\text{Co}$  measurements, shown in Figure I-14, were dominantly affected by the systematic uncertainties of the source positions and activities. In Table I-5 the final optimised active volume and the corresponding borehole parameters are compared to their nominal values before the optimisation. The final value of the active volume was obtained as a weighted average from the results of the  $^{137}\text{Cs}$ ,  $^{54}\text{Mn}$ , and  $^{60}\text{Co}$  measurements. Since the systematic uncertainties were dominant, the final value represents a compromise of the measurement results. The uncertainty of the optimised active volume is the root-mean-square (RMS) deviation of the measurements results. Also in this case the optimised dimensions do not necessarily represent a realistic borehole, but can compensate for various geometrical or physical errors affecting the active volume of the detector in the MC simulation (including e.g. the effects of variation in the charge collection properties within the crystal).

**Table I-5** Detector geometry parameters before and after optimisation.

Parameter	Nominal value	Optimised value
Front dead layer [mm]	0.7	1.684 (22)
Side dead layer [mm]	0.7	1.582 (18)
Active volume [cm <sup>3</sup> ]	162.3	156.5 (22)
Borehole length [mm]	38.0	41.24 (96)
Borehole radius [mm]	5.0	8.24 (96)

## 9.4. Results and discussion

As can be seen from Table I-6, the accuracy of our MC-based efficiency determination was greatly improved throughout the energy range with the help of the optimisation. The large deviations in energies below ~100 keV prior to the optimisation are a clear indication that the thickness of the dead layer was significantly underestimated. At higher energies (above 103 keV), the mean deviation of the nominal results was 22.6 % (RMS uncertainty 2.4 %), which is much larger than what can be explained by source activity or position uncertainties and was most likely caused by the inaccurate size of the active volume in the detector MC model.

**Table I-6** Relative deviations between FEP efficiencies obtained experimentally, and from MC simulations using nominal and optimised detector parameters. The values were calculated using the formula  $RD = (\epsilon_{MC} - \epsilon_{exp}) / \epsilon_{exp}$ . The reference geometry is depicted in Figure I-11. The uncertainties include contributions from statistics, source activity and position.

Source	Energy [keV]	RD <sub>nominal</sub> [%]	RD <sub>optimised</sub> [%]
<sup>241</sup> Am, Buchler 1969	59.5	159 (16)	-13.1 (53)
	99 & 103 <sup>a</sup>	22.5 (77)	3.3 (21)
<sup>133</sup> Ba, IPE / PTB 2007	81.0	68.7 (33)	-11.5 (55)
	276.4	23.5 (31)	4.9 (27)
	302.9	25.0 (26)	4.7 (22)
	356.0	22.9 (24)	2.8 (20)
	383.9	19.4 (28)	5.7 (25)
<sup>137</sup> Cs, Buchler 1969	661.7	21.0 (74)	-0.5 (61)
<sup>54</sup> Mn, QSA 1999	834.8	19.3 (39)	-1.5 (33)
<sup>60</sup> Co, IAEA 1970	1173.2	22.9 (76)	0.0 (62)
	1332.5	22.5 (76)	-1.6 (61)
<sup>228</sup> Th, QSA 2006	2614.5 <sup>b</sup>	27.1 (22)	2.2 (19)

<sup>a</sup> energy resolution of the detector prevented separation of the two low-intensity  $\gamma$ -lines of <sup>241</sup>Am, therefore all calculations were done with the sum of the counts in the two peaks

<sup>b</sup> in the case of <sup>228</sup>Th the source housing was not modelled, but the effect was considered negligible at this energy

The improved results exhibit accuracy well compatible with the needs of efficiency determination for material-screening measurements. The mean deviation was -0.4 % with 5.8 % RMS dispersion, respectively 1.9 % with 2.7 % RMS when considering only energies above 103 keV. The remaining deviations can be attributed mostly to the relatively high uncertainties in the activity and position of the radioactive standards used. Should a better accuracy be needed than that achieved in this work, using more accurate calibration standards and a more precise positioning system would significantly improve the results.

## 10. Application of the Monte Carlo efficiency determination to material-screening measurements evaluation

Optimised detector-model geometry is only one part of improving the accuracy of MC-based detection-efficiency evaluation. Since practically all of the samples measured in low-level material screening detectors have volumes larger than what can be approximated by a point-like source, it is necessary to reproduce also the sample geometry with very good accuracy. With these steps taken, the contribution of MC-based efficiency to the overall uncertainty of the reported measurement

results can be made negligible.

To test the accuracy of sample-geometry reproduction in the simulation, two extended-volume standards (a  $\text{K}_2\text{CO}_3$  powder and a  $^{228}\text{Th}$  solution) were measured in the Corrado detector. The geometry of the detector itself had been already optimised, so any remaining significant discrepancies could only be related to the samples. The  $\text{K}_2\text{CO}_3$  powder has a natural isotopic content, therefore the activity of  $^{40}\text{K}$  was calculated from the weight of the sample. The  $^{228}\text{Th}$  was prepared from a purchased standard solution.

The Table I-7 shows a comparison between FEP efficiencies obtained from MC simulations and those calculated from the known activity of the sources. The mean deviation of the results is 2.4% with 2.6% RMS dispersion. These results demonstrate the achieved accuracy of MC-based efficiency determination for material-screening samples.

**Table I-7** Simulation to measurement comparisons of extended sources performed with the Corrado detector. The values were calculated for each isotope and  $\gamma$ -line using the formula  $RD = (\epsilon_{MC} - \epsilon_{exp})/\epsilon_{exp}$ . Uncertainties include the source activity uncertainties,  $\gamma$ -line intensity uncertainties and the statistical uncertainties.

Sample Description	Isotope	Energy [keV]	RD [%]
$^{228}\text{Th}$ solution in a cylindrical container	$^{212}\text{Pb}$	239	4.6 (33)
		300	-0.4 (55)
	$^{212}\text{Bi}$	727	2.7 (35)
		277	5.2 (65)
	$^{208}\text{Tl}$	583	2.7 (32)
		861	-1.1 (37)
2615		-0.7 (32)	
$\text{K}_2\text{CO}_3$ powder in a cylindrical container	$^{40}\text{K}$	1461	5.9 (22)

It is remarkable that the MC simulations of Bruno and Dario detectors exhibit accuracy satisfactory for the purposes of low-level material screening (as discussed in Section 5) even without performing geometry optimisation, as was necessary with Corrado. The remaining deviations in the results from Bruno and Dario are mainly significant only in the lowest part of energy range, which does not affect the evaluation of most  $\gamma$ -ray contaminants important to low background experiments (the primordial isotope decay chains, man-made and cosmogenic isotopes).

The software models of the three MPIK low-level detectors, presented and validated in this chapter, have already been used in the evaluation of a number of material-screening measurements. The results of these measurements were used for selecting construction materials for a range of components of the GERDA experiment (e.g. steel and welding materials for the LAr cryostat vessel and water tank, superinsulation for the cryostat, copper for inner shielding, Kapton material for detector cabling, etc.). Evaluations of various samples were also performed for the Double Chooz (DC) experiment [85]. A summary of the results is shown in Table I-8. Furthermore, the presented MC simulations were also used in a survey of steel samples for the construction of GERDA cryostat, reported in [47].

For new measurements that will be performed with the Corrado detector, the systematic relative uncertainty of the MC-determined detection efficiency can be assumed  $\sim 7\%$ , thanks to the optimised software model of the detector. This was already the case for the "bis-MSB wavelength shifter" sample in Table I-8 (the sample geometry is shown in Figure I-5, top right). For samples with difficult geometry, such as e.g. the "Flexible stainless steel vacuum tubes" (Figure I-5,

bottom), and for measurements performed with detectors without the optimised geometry (Bruno and Dario), 12% is a conservative estimation of the systematic MC uncertainty. Still, this is for the results reported in Table I-8 only a small contribution to the upper limits and to the uncertainty of the activity concentrations.

**Table I-8** Results of material-screening measurements performed at LLL. The measurements were performed by the low-level  $\gamma$ -spectrometry group of MPIK, comprising Hardy Simgen, Mark Heisel, Werner Maneschg and the author. The upper limits are expressed with 95% confidence. The uncertainty intervals include the systematic uncertainties of the line background for some samples.

Sample description	Mass [kg]	Measuring time [d]	$^{238}\text{U}$ [mBq·kg <sup>-1</sup> ]	$^{226}\text{Ra}$ [mBq·kg <sup>-1</sup> ]	$^{228}\text{Ra}$ [mBq·kg <sup>-1</sup> ]	$^{228}\text{Th}$ [mBq·kg <sup>-1</sup> ]	$^{40}\text{K}$ [mBq·kg <sup>-1</sup> ]	$^{60}\text{Co}$ [mBq·kg <sup>-1</sup> ]
Stainless steel (Dillinger Hütte GTS)	55.7	13.91	–	2.04 ± 0.33	1.63 ± 0.41	5.34 ± 0.69	2.29 ± 1.14	0.20 ± 0.09
Stainless steel for GERDA PMT encapsulation DIN 1.4301	63.7	20.91	–	0.69 ± 0.31	< 1.8	1.73 ± 0.40	< 2.2	17.6 ± 1.3
Stainless steel DIN 1.4429	43.9	11.6	84 ± 24	1.36 ± 0.35	1.65 ± 0.63	5.85 ± 0.68	< 2.1	4.78 ± 0.52
Discs for Double Chooz (DC), stainless steel 304 L	1.19	10.69	< 285	< 7.4	< 17	22.7 ± 6.2	43 ± 25	12.9 ± 2.2
Steel welding rods Thermanit GE316L (Thyssen Böhler)	19.76	9.55	–	3.18 ± 0.55	2.20 ± 0.86	7.2 ± 1.1	10.3 ± 2.5	1.78 ± 0.28
Steel welding rods (SIMIC)	1.95	1.04	–	< 8.4	< 17	< 16	< 43	23.6 ± 4.1
Cu-Sn welding wire (Pützschler & Weiler)	4.81	12.95	–	< 31	< 27	< 14	< 39	< 2.0
Erosion wire HBZ V 25	4.96	8.85	–	< 8.3	< 4.8	< 4.3	< 11	< 0.5
Kapton <sup>®</sup> flat cable (with Cu) KCL 2-17/50FR (Krempel)	3.4	5.15	–	< 34	< 15	< 11	20 ± 11	< 1.5
Kapton <sup>®</sup> rolls (DuPont <sup>™</sup> )	0.44	21.01	–	13.2 ± 7.3	< 21	< 21	< 105	–
IGLIDUR <sup>®</sup> sliding plastics (IGUS <sup>®</sup> )	1.9	18.93	–	< 15	< 18	< 15	37 ± 16	–
Superinsulation foil (Austrian Aerospace)	0.95	14.26	–	< 52	54 ± 33	< 48	168 ± 43	–
Superinsulation foil (Jehier <sup>®</sup> Insulray IR 305)	0.5	12.68	–	132 ± 42	< 95	< 54	(1.31 ± 0.19)×10 <sup>3</sup>	–
Al tape for superinsulation	0.58	10.04	–	84 ± 38	< 47	< 39	77 ± 26	–
Makrolon <sup>®</sup> insulation	12.96	2.49	< 302	< 2.9	< 7.2	< 3.5	< 31	< 1.6
Polyethylene PE HWST for LENS [90] and LArGe [91] (Simona AG)	8.72	11.27	–	< 5.8	< 12.8	< 4.7	< 22	–
Laminated epoxy resin EP GC 203 (Hippe KG HGW 2372.4)	0.14	8.14	(4.4 ± 1.7)×10 <sup>3</sup>	(3.00 ± 0.17)×10 <sup>3</sup>	(1.49 ± 0.15)×10 <sup>3</sup>	(1.27 ± 0.13)×10 <sup>3</sup>	(10.2 ± 1.2)×10 <sup>3</sup>	< 28
Gd(NO <sub>3</sub> ) <sub>3</sub> for DC	0.08	9.82	–	–	–	–	392 ± 103 *	–
Residual from Gd(thd) <sub>3</sub> sublimation	0.05	5.25	–	–	–	–	(23.5 ± 2.9)×10 <sup>3</sup> *	–
PPO wavelength shifter for DC	0.5	3.14	–	< 47	< 54	146 ± 27	< 127	–
bis-MSB wavelength shifter for DC (Sigma Aldrich)	0.27	13.15	< 2150	< 32	< 27	< 38	< 102	< 11
Flexible stainless steel vacuum tubes for DC	0.2	8.78	< 3180	< 32	< 62	< 28	132 ± 67	< 30

\* results of atomic-absorption spectrometry were  $\sim 7\times$  higher in case of Gd(NO<sub>3</sub>)<sub>3</sub> and  $\sim 2\times$  lower for Gd(thd)<sub>3</sub>. It is hypothesized that sample inhomogeneity is the cause.

## II Germanium detector signal analysis: BEGe detector study

In Section 3.1 of the Introduction the advantages were pointed out, that multiple-site interactions recognition and rejection have on  $\beta\beta$ -decay sensitivity. From the discussed techniques based on this principle, the pulse-shape analysis (PSA) and the detector segmentation have the potential to discriminate between different interaction patterns contained within the volume of one detector. With detector segmentation one has additionally the ability to locate interaction points in individual detector segments. When combined with PSA, as good as sub-millimetre position sensitivity is possible [92].

PSA on unsegmented Ge-detectors can usually provide only the information that an interaction was either local (single-site event – SSE) or consisting of several energy depositions separated in space (multi-site event – MSE). On one hand, it is limited information compared to the three-dimensional position sensitivity of a segmented detector. On the other hand, this information is sufficient to reject background events in a  $^{76}\text{Ge}$   $0\nu\beta\beta$ -decay experiment. With regards to the ultra-low background requirements of such experiments, unsegmented detectors have a significant advantage relative to segmented, thanks to their much lower demands on the amount of detector contacts and signal readouts. In addition to the high voltage (HV) contact, segmented detectors require a signal contact with front end electronics for each segment, while unsegmented detectors need only one. This reduces potential background sources around the detectors.

In past double-beta decay experiments, PSA techniques were applied to coaxial unsegmented detectors [63,93]. However, as discussed in properties of the Ge-detector, especially the shape of the weighing potential of the read-out electrode, significantly affect the efficiency of PSA discrimination. For an efficient pulse shape discrimination (PSD), the shape of the weighing potential must allow an easy identification of MSE and SSE. The discrimination must not be affected significantly by electronic noise present in read-out systems. The differences between MSE and SSE in coaxial detectors are relatively subtle, requiring complex analysis methods, such as e.g. neural networks [62], to achieve any significant discrimination power.

As follows from the process of signal development, described briefly in Section 2.3, improved signal discrimination can be achieved when the weighing potential has a strong position dependence. In practice, this can be achieved by making the signal read-out electrode small. In that case the electrical fields and in turn the weighing potential near the small electrode sharply increase. A comparison of such favourable weighing potential function to a weighing potential of a typical coaxial HPGe detector will be presented in Section 12 (Figure II-17).

Detectors with a minimal size of the signal electrode have been built in past. Very good pulse-shape discrimination properties were found for point-contact, or modified electrode detectors (with  $\text{Ø}2\text{ mm} \times 0.5\text{ mm}$  electrode) [94,95]. An additional advantage of such detectors is that due to the small area of the read-out electrode, their capacitance is very small and thus the serial component of the electronic noise can be greatly reduced. Besides the positive influence the low noise has on

PSA, improvements in energy resolution and low-energy threshold<sup>2</sup> are themselves very useful, especially for  $0\nu\beta\beta$ -decay experiments. To improve charge collection characteristics of these detectors, they are manufactured from a germanium material with an impurity gradient along the detector axis. This provides additional space charge in the volume of the detector after depletion, improving the axial drift of charge carriers towards the electrodes. The relatively low strength of the electric field in most of the crystal volume, combined with the longer charge carrier drift distance as compared to similarly sized coaxial crystals, cause typically longer charge collection times in point-contact detectors. This provides another benefit for the PSA, as explained in Section 3.3.

One standard type of detector offered by Canberra Semiconductor N.V. Olen has a similar configuration like the point-contact detector [96]. The Broad-Energy Germanium detector (BEGe) [97] has a small collecting electrode, and is used for applications demanding a good energy resolution and a detection efficiency in the energy range of 3 keV to 3 MeV. The difference between BEGe and point-contact detectors is mainly in their shape and the read-out electrode size. While point-contact detectors are built like traditional coaxials with their diameter approximately equal to their height, BEGe has a more flat shape (Figure II-1). The read-out electrode is larger in BEGe, to minimise mechanical difficulties associated with a small electrical contact.

A custom modified BEGe was purchased by MPIK and, for the first time, an investigation of this detector type's potential for active background suppression with PSA was performed. Initial results of the investigation were reported in [98]. Here, a comprehensive description of the detector characterisation and PSA investigation is given, and improved results are presented.

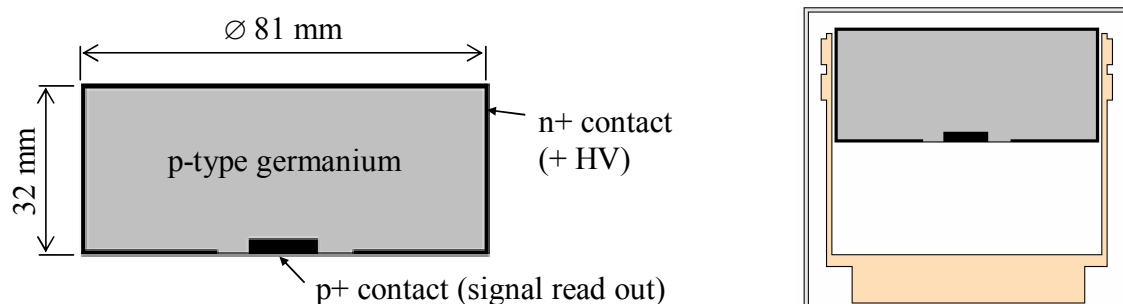


**Figure II-1** Left: Schematic drawing of the studied 878 g p-type crystal of a broad-energy Ge-detector, manufactured by Canberra Semiconductor, N.V. Olen [97]. The signal read-out electrode is not to scale. Right: Schematic drawing of the detector mounted in its copper holder inside an aluminium cryostat.

## 11. Detector setup

The detector is a modified model BE5030 with a mass of  $\sim 880$  g, the largest BEGe conventionally available from Canberra. A schematic depiction of the crystal along with its dimensions can be found in Figure II-1. The crystal is made of  $p$ -type HPGe, with the Li-drifted  $n+$  contact covering the whole outer surface, including most of the bottom part. A passivated groove separates the elec-

<sup>2</sup> As discussed in Section 3, low energy threshold is required in GERDA for  $^{68}\text{Ga}$  background suppression by time-delayed coincidence with the detection of its mother isotope's  $^{68}\text{Ge}$  10 keV X-ray emission.

trical contacts. The size of the small  $p+$  contact, as well as the profile of the impurity gradient was not disclosed by the manufacturer. Typically the manufactured BEGe detectors have the top  $n+$  contact thickness reduced by machining to minimise low-energy  $\gamma$ -ray absorption in the inactive layer. This was omitted in case of the MPIK purchased diode, because it is of no advantage for  $\beta\beta$ -decay experiments. In GERDA, thick dead layers are desirable as a protection from  $\alpha$ 's,  $\beta$ 's and low energy  $\gamma$ 's from potential surface contaminations of the detectors. As well, the detector housing has a standard-thickness aluminium window as opposed to the low-absorption entrance windows normally supplied with BEGe detectors. The company-specified performance characteristics are listed in Table II-1. The detector was installed in the Low Level Laboratory of MPIK (a photo of the setup is on Figure II-2), and tested with both analogue and digital DAQ systems.

**Table II-1** Company specifications of the supplied BEGe detector. A shaping constant of 4  $\mu$ s was used for the resolution measurement at the company.

Depletion voltage [V]	4000
Front dead layer thickness [mm]	0.5
FWHM at 122 keV [eV]	632
FWTM at 122 keV [eV]	1184
FWHM at 1332.5 keV [eV]	1801
FWTM at 1332.5 keV [eV]	3322

### 11.1. Detector read out and DAQ system

The front-end read out is performed with a Canberra 2002CSL RC-feedback preamplifier with a cooled FET. It has a specified noise of 570 eV (at 0 pF input capacitance) and a rise time of 20 ns (at 30 pF input capacitance). The measured conversion gain was  $\sim 300$  mV/MeV. The decay constant of the preamplifier signal was 47  $\mu$ s.

An analogue spectroscopy amplifier with an ADC system was used for early detector characterisation measurements and for measurements sensitive to dead time (as this was an issue with the FADC).

A digital DAQ system was used for recording pulse shapes with 10 ns sampling. It consisted of a universal variable amplifier built in-house, used for signal amplification without shaping and a Struck SIS 3301 14-bit, 100 MHz flash ADC (FADC) with an internal trigger. A scheme of the digital DAQ system is depicted in Figure II-3. The FADC data-acquisition software was based on the one developed for the GENIUS-TF experiment [99]. Besides recording signal traces, it uses integration and differentiation filtering to shape signals and produce energy spectra.

The DAQ system contribution to the energy resolution, measured with a pulser, was  $(0.6 \pm 0.1)$  keV, dominated by the preamplifier (0.57 keV company specification). The shaping constant used for spectroscopic measurements was 14  $\mu$ s. However, an optimal spectroscopic resolution is achieved with 8  $\mu$ s shaping, when a proper rise-time compensation is used [100]. Such long shaping constants are required due to the long charge collection times and consequently long signal rise times of the BEGe detector, increasing the effect of ballistic deficit. The best achieved energy resolution of the system at 59.5 keV and 1332.5 keV is shown in Figure II-4. Normally the energy resolution was around (0.1-0.2) keV higher, mainly due to a high-frequency noise pick-up (coming

mostly from the VME processor and other digital devices in the laboratory), and due to a non-operational rise-time compensation in our DAQ software. As shown in Figure II-5, the time resolution of the DAQ was  $\sim 20$  ns. This was dominated equally by the preamplifier and the FADC, both having an analogue bandwidth of  $\sim 50$  MHz.



**Figure II-2** The BEGe test setup in MPIK Low Level Laboratory. The detector (at the middle right) is covered with a copper and lead shield.

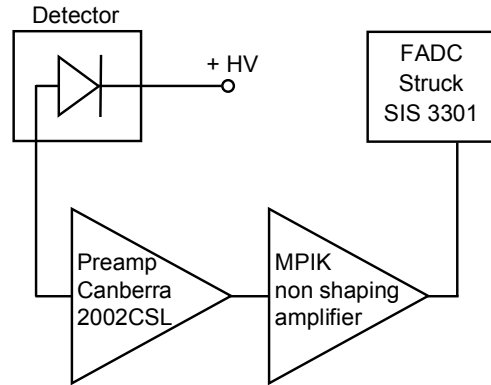


**Figure II-3** A scheme of the BEGe digital DAQ system. The non-shaping amplifier is used to match the preamplifier output to the input range of the FADC.

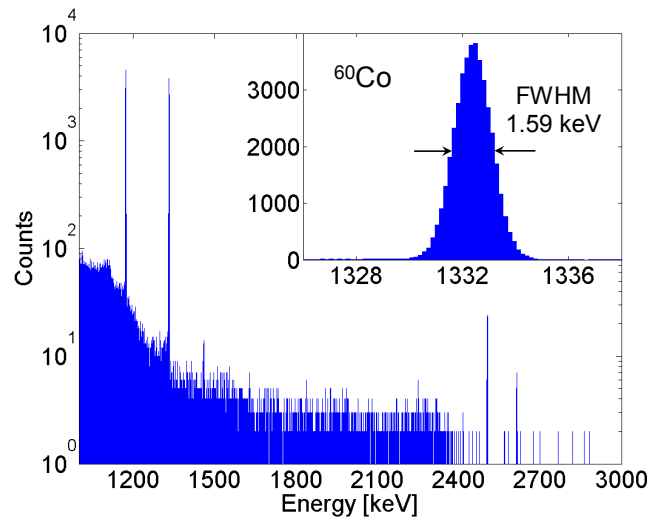
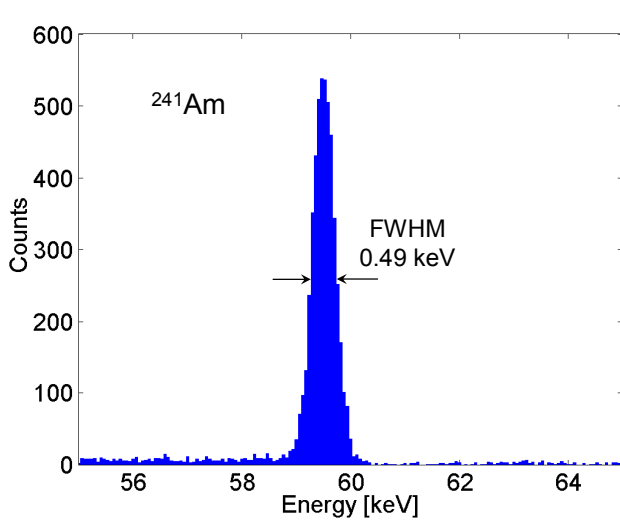


**Figure II-4** The best energy resolution achieved with the BEGe detector, with cabling and electrical connections optimised for minimal noise pick-up, using  $8 \mu\text{s}$  shaping with rise-time compensation [100].

Due to the  $47 \mu\text{s}$  long decay time of the preamplifier and the requirement of long shaping constants, the BEGe has an elevated susceptibility to signal pile-up. If an event occurs within a few multiples of the decay time after another pulse, the recorded signal will be imposed on top of an exponentially decaying baseline. Since the baseline measured in front of the pulse is always subtracted to obtain the net amplitude of the signal, a slope in the baseline can cause noticeable distortion to the calculated energy of the event. An uncorrected exponentially decreasing baseline measurement will result in underestimation of the energy. To account for this, a pile-up rejection was applied off-line to the signals recorded by the FADC. The slope of the baseline was calculated,

and events with baseline slope higher than the average fluctuation were rejected. An example histogram of the baseline slopes of recorded events from a high-rate  $^{60}\text{Co}$  measurement is shown in the left-hand part of Figure II-6. The extent of the normal noise-induced baseline slope fluctuation is visible. The pile-up rejection was achieved by cutting the extended tail to negative slopes. The 1332.5 keV peak before and after the pile-up cut is shown in the right-hand part of Figure II-6.

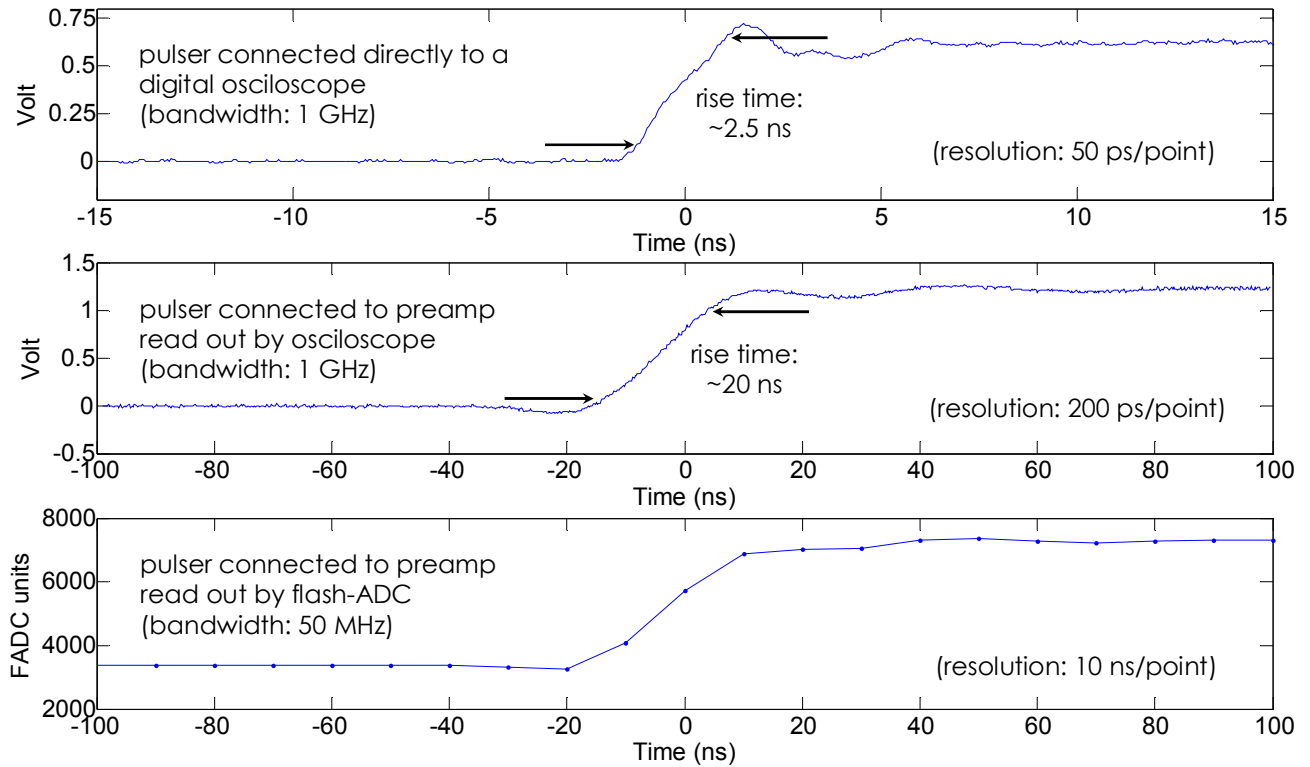


**Figure II-5** Measurement of time resolution of the DAQ with a fast pulser. The pulser rise time, measured with a fast digital oscilloscope (top plot) is ~2.5 ns. The signal generated by the preamplifier (middle plot) has ~20 ns rise time, in agreement with the manufacturer specification. The rise time of the signal trace recorded by the FADC is practically unchanged.

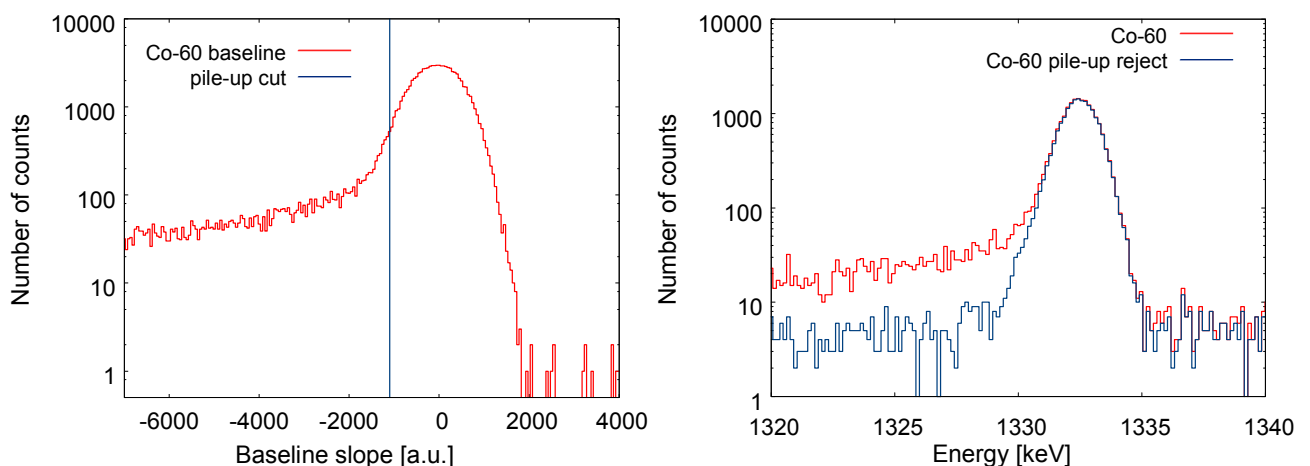


**Figure II-6** **Left:** Histogram of the baseline slope from a  $^{60}\text{Co}$  spectrum with a total rate of 209 counts per second. The broad peak represents the noise-induced fluctuation of the baseline and the tail to negative slopes corresponds to events imposed on a decaying signal from a previous event. The pile-up rejection cut was applied at a point where the tail becomes more significant than the noise fluctuation. **Right:** 1332.5 keV peak from the same spectrum, before and after pile-up rejection.

## 11.2. Detector characterisation and testing

A measurement of the detector counting characteristics in dependence on the high voltage (HV) is shown in Figure II-7. As can be deduced from the plots, a relatively high bias voltage is required to fully deplete the BEGe detector. Large deviations are visible in the counting characteristics shortly before reaching full depletion. The peak intensity and positions are highly instable at values of HV between  $\sim 3$  kV and 3.5 kV. Since with increasing HV, the depletion region grows from the  $p$ - $n$  junction (at the outer  $n$ + electrode) inwards, these deviations seem to occur when the volume near the  $p$ + electrode begins to deplete. The effects of partial depletion of this region with a high gradient of potential likely cause the observed instabilities. Full depletion and stable operation are reached at 3.6 kV bias voltage, which is lower than the company specified depletion voltage of 4 kV. Based on these measurements, the operating voltage was chosen at 3.8 kV.

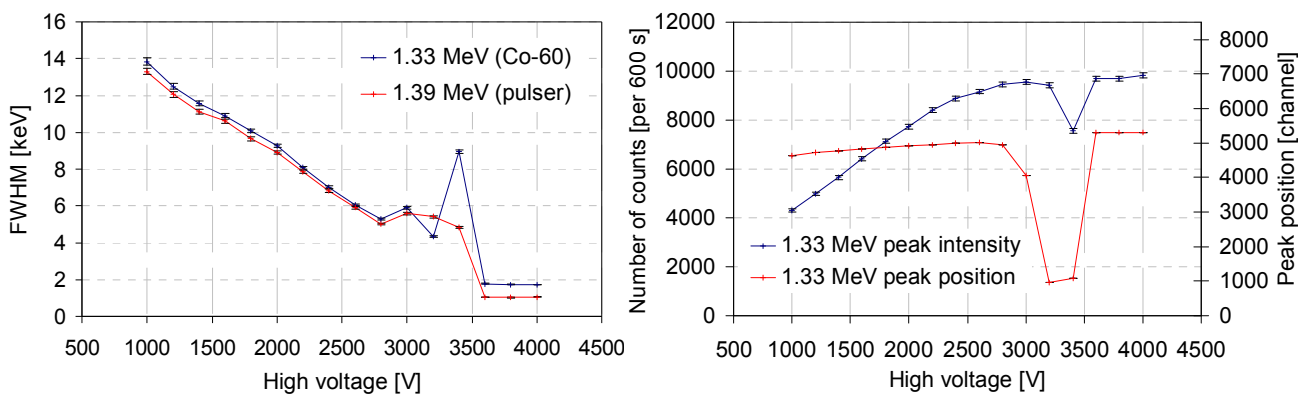


**Figure II-7** Measurement of energy resolution (left), peak intensity and position (right) in dependence of bias voltage applied to the  $n$ + contact of the detector. The measurement was performed by K. Gusev.

### 11.2.1. DAQ system stability

The digital DAQ system of the BEGe detector was set up in a temporary arrangement, intended for short-term testing. The setup had shortcomings in its electrical stability and a fluctuation of the signal gain was observed. The left part of Figure II-8 shows the 2614.5 keV peak position variation during a series of measurements (this was the  $40^\circ$  Compton scattering coincidence run, which will be analysed in Section 13.3). It can be seen that significant gain jumps have occurred. This variability was taken into account in data evaluation, and with frequent recalibrations its effects on the results were minimised. However, to improve stability for future measurements and to test whether the detector itself had any contribution to this variability, comprehensive stability testing was performed.

The test included a seven week series of 3 hr measurements with  $^{241}\text{Am}$  and  $^{60}\text{Co}$   $\gamma$ -ray sources, and a pulse generator on the preamplifier test input. A modest optimisation of the setup cabling and grounding scheme was performed before the test. The peak position variation in this stability test is shown in the right part of Figure II-8. It is evident that the amount of fluctuation was significantly reduced with the modest improvement of the setup, with the maximal peak difference dropping from  $\sim 10$  keV at 2614.5 keV (0.4%) to  $\sim 0.5$  keV at 1332.5 keV (0.04%).

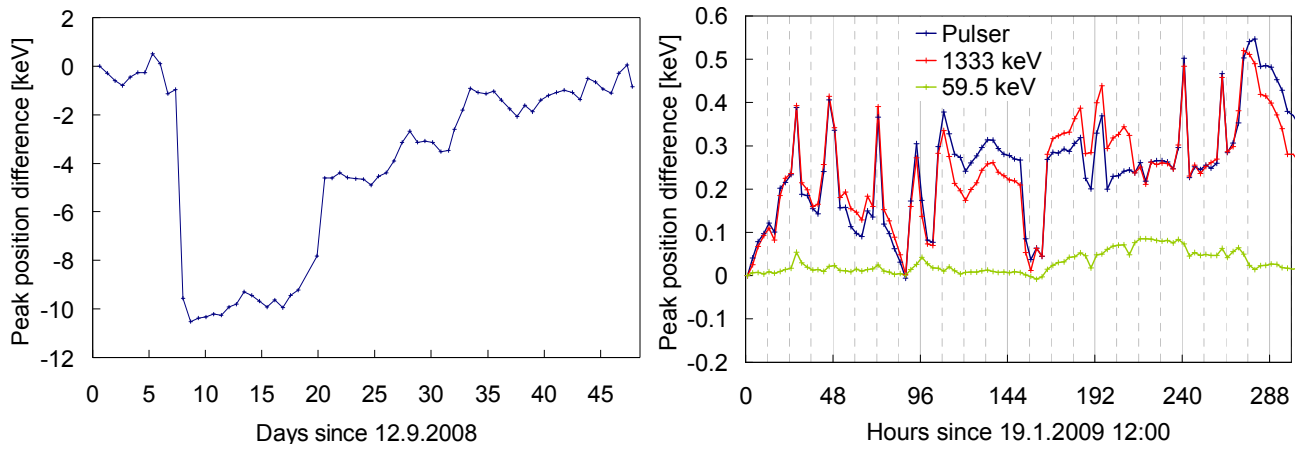


**Figure II-8** **Left:** Fluctuation of the 2614.5 keV peak position in a series of measurements, taken on average every 17 hours (40° coincidence scattering data set, see Appendix). The position difference with respect to the first measurement is plotted. The average FWHM resolution of the peak was 2.3 keV. **Right:** Peak fluctuations of the 59.5 keV peak, 1332.5 keV peak and a pulser peak at 1406 keV in a stability test, with 3 hour measurements. The position difference with respect to the first measurement is plotted. Only a subset of the measurements is shown for better visibility.

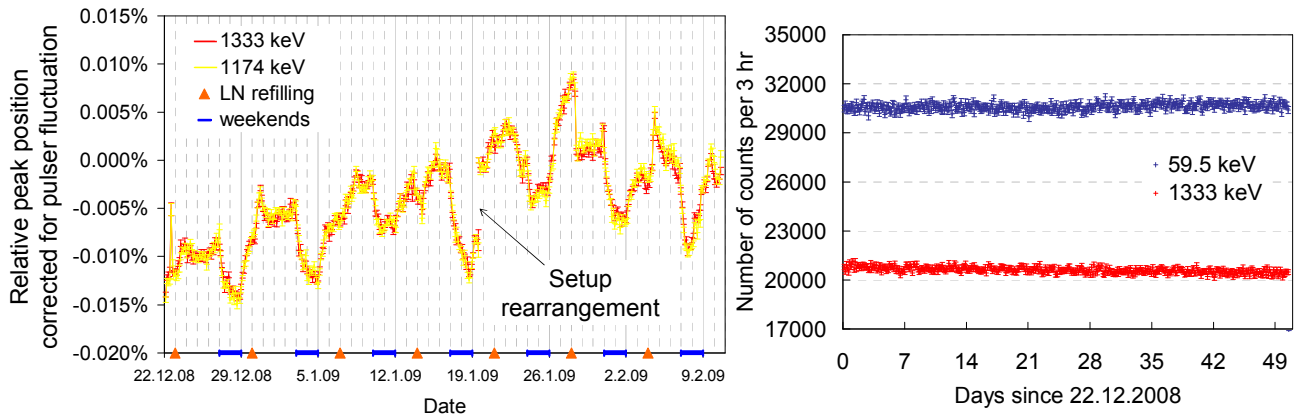


**Figure II-9** **Left:** Relative fluctuation (position difference relative to first measurement) of the 1173.2 keV and 1332.5 keV peaks, after subtracting the relative fluctuation of the pulser peak. Correlations with LN refilling and with the working week are indicated. **Right:** Count rate of the 59.5 keV and 1332.5 keV peaks during the stability test.

The remaining fluctuation is still significantly higher than statistical errors. As can be seen from the right part of Figure II-8, the most obvious variation is between day and night. To correct for DAQ system fluctuation, the pulser-line fluctuation was subtracted from the  $\gamma$ -line fluctuation. The result is plotted in the left-hand side of Figure II-9. The maximal remaining relative deviation between the pulser peak and the  $\gamma$ -lines is  $\sim 0.015\%$ , corresponding to about 0.2 keV. Correlations with the liquid nitrogen (LN) refillings of the detector's dewar and with the course of the working week are highlighted. These correlations are an indication that the remaining deviation is caused by activities in the laboratory disturbing the pulser amplitude. No long-term trend was observed during the measurements.

The right-hand side of Figure II-9 shows the count rate in the 59.5 keV and 1332.5 keV peaks during the test. The slight decrease of the number of counts in the 1332.5 keV peak is consistent with the  $^{60}\text{Co}$  half life of 5.27 years. No fluctuation in BEGe charge collection or deterioration of the detector characteristics was observed in the stability test. The energy resolution of the 59.5 keV, 1332.5 keV  $\gamma$ -lines and the pulser peak was stable at  $(0.60 \pm 0.01)$  keV,  $(1.62 \pm 0.02)$  keV and

( $0.54 \pm 0.04$ ) keV, respectively, during the stability test. It is expected that a better isolation of the digital DAQ electronics from electromagnetic and microphonic interferences can further reduce the electronic gain and bandwidth variability.

### 11.2.2. Charge collection study

The BEGe has a relatively low electric field in its depleted region, and the charge collection times reach up to 1  $\mu$ s (see e.g. Figure II-16), compared to the few 100 ns that are usual in coaxial HPGe detectors. As examined in Section 2.3, at long charge collection times charge trapping and recombination losses can become a concern. Various material impurities can cause trapping. These can be expected to be distributed homogeneously throughout the detector volume. Observable effects of a deep trapping would be a shift of peak positions to higher energies and an improvement of energy resolution when increasing the bias voltage beyond full depletion. No such effects were observed in the characterisation measurements presented at the beginning of Section 11.2. Shallow trapping could cause an increase in charge collection time, (inducing ballistic deficit) and possibly a worsening of the energy resolution due to the larger variation in the collected charge. The ballistic deficit itself can negatively affect the resolution, and also cause an asymmetrical shape of the peaks. As was shown in Figure II-4, the measured energy resolution was very good. Any charge trapping by homogeneous impurities is found to be insignificant.

Crystal lattice defects can also act as traps and recombination centres. Such defects can occur due to imperfections in Ge-crystal growth or due to damage. These can be distributed inhomogeneously within the crystal. Due to the low intrinsic electric field, they could create regions of reduced, or completely absent charge collection. This would be a significant concern for GERDA, because it could lead to losses of effective target mass and detection efficiency, worsening the sensitivity. Therefore a comprehensive study was undertaken to characterise the efficiency of charge collection in BEGe detector.

Most visible effects of inhomogeneous trapping and loss of signal in parts of the crystal volume are low energy tails of full energy peaks. However, similar tails can be created as a result of signal pile-up. The pile-up tails were indeed observed in some high count rate spectra taken with BEGe. The pile-up effects in BEGe and a method for their removal were described in Section 11.1. Figure II-10 shows that after applying pile-up rejection to a high count rate peak, its shape becomes similar as in a low-rate spectrum. The tail is removed, hence it is evident that it was composed of piled-up events and not by incomplete charge collection. However, the pile-up rejection is not 100% effective and a small tail still remains.

Another tailing effect happens during the detection of low energy  $\gamma$ -rays. Due to their low range in germanium, significant part of their energy can be lost in the detector dead layer. As shown on Figure II-11, the same effect is observed also in Monte Carlo simulations (the simulation was done with a standard  $p$ -type coaxial detector). It is not related to the process of charge collection in the active volume of the detector.

Possible inhomogeneities in charge collection were further investigated by performing several scans with a collimated low energy  $\gamma$ -ray beam along the surfaces of the detector. The 59.5 keV line of  $^{241}\text{Am}$  and the 122 keV line of  $^{152}\text{Eu}$  were used for the measurements. A drawing and a photo of the experimental setup are displayed on Figure II-14. Three scans of the top surface along different

axes, and two scans at different positions along the side of the cylinder were performed. Analysed quantities were the position, energy resolution and count rate in the full energy peak.

The maximal variation of the peak position in one scan was 0.075%, measured along the top surface. This is less than 0.15% as was reported for a custom built point-contact detector [95]. Furthermore, no obvious trend can be noticed in the peak position and the FWHM variation along the scans. The peak position variation is in agreement with the observed gain fluctuation caused by the noise of the DAQ system, discussed earlier in Section 11.2.1. The peak position and FWHM in function of the beam position in a top and a side scan are summarised in Figure II-12.

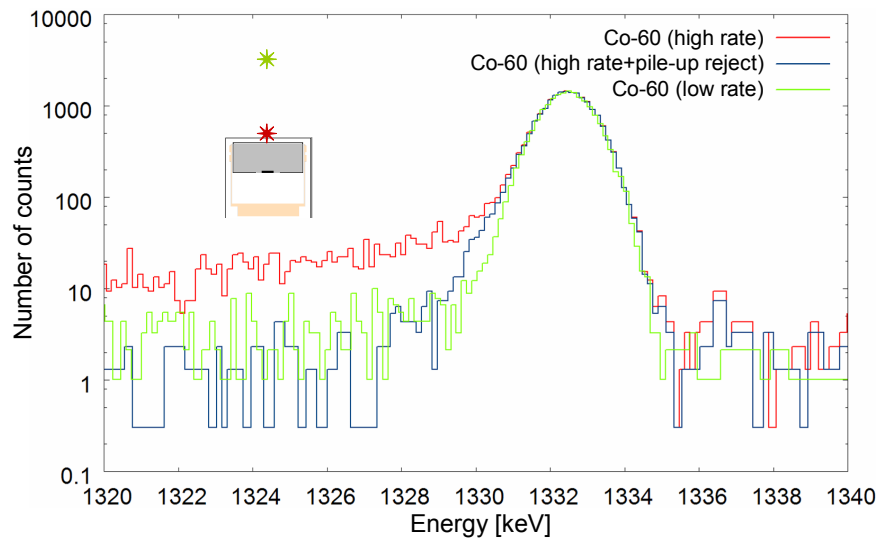


**Figure II-10** The full energy peak of the 1.33 MeV line in  $^{60}\text{Co}$  spectra. The red spectrum was measured in close source geometry, and is showing a significant tail to lower energies caused by signal pile-ups. The blue spectrum was obtained by applying offline software pile-up rejection to the latter. The green spectrum was measured with the source further away, thus with a lower count rate. No tailing is observed in this case. The spectra are normalised to the same peak height. The relative positions of the source and the detector are indicated in the inset by the colour-coded stars.

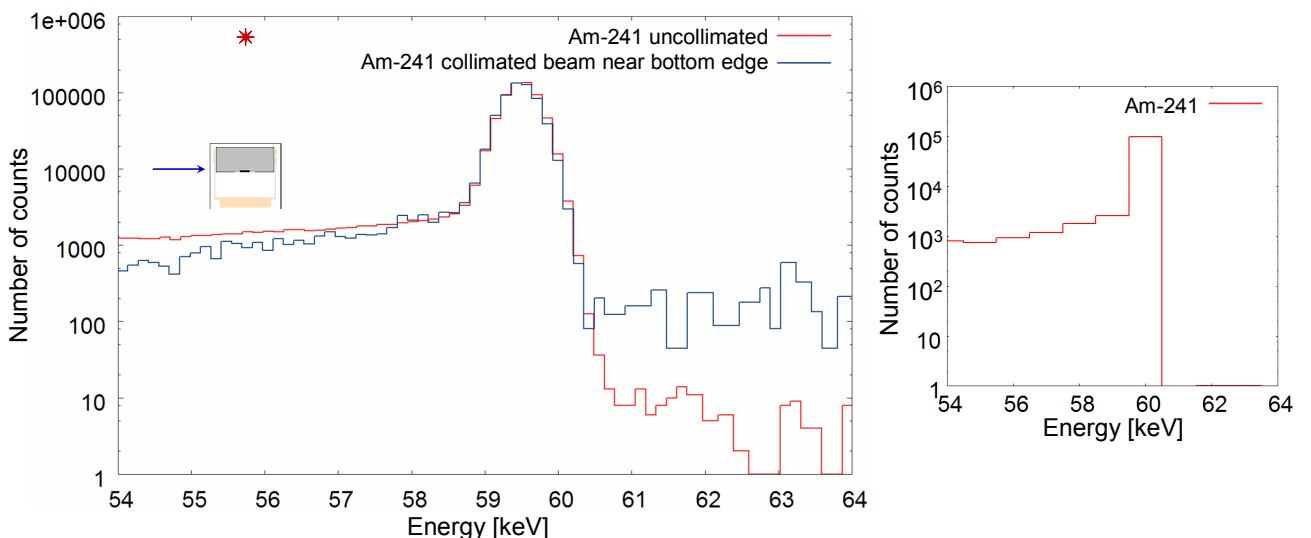


**Figure II-11** The 59.5 keV peak in  $^{241}\text{Am}$  spectra. **Left:** The red spectrum was measured with an uncollimated source at the front of the detector; the blue spectrum is from a collimated beam at the position shown in the inset. The spectra are normalised to the same peak height. No difference is seen between the peak tails, although the collimated beam is at a position where a weak electric field could be expected. **Right:** Monte Carlo simulation of a  $^{241}\text{Am}$  spectrum in another Ge-detector, showing a similar tail, caused by a partial energy loss in the dead layer and the cryostat window.

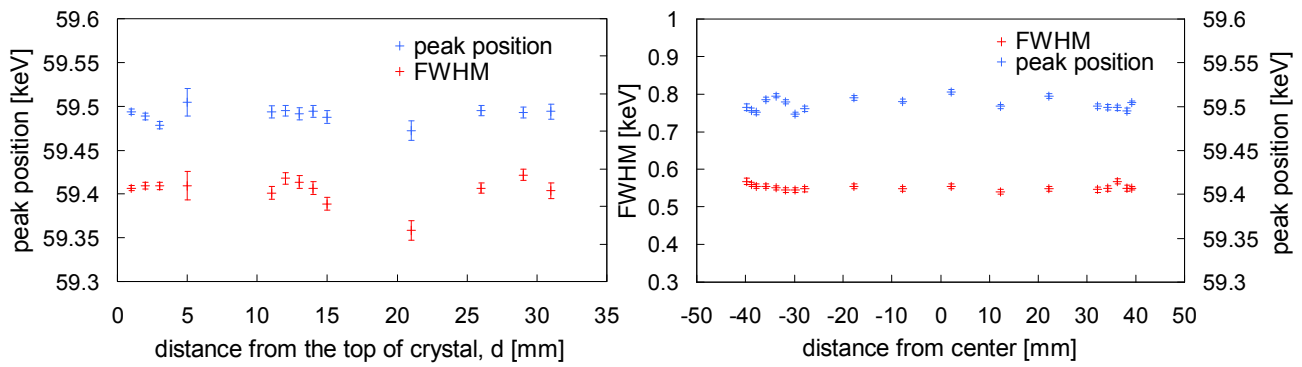


**Figure II-12** Peak position and energy resolution variation along the side (left plot) and the top (right plot) surfaces of the BEGe detector, obtained with a collimated 59.5 keV  $\gamma$ -ray beam from a  $^{241}\text{Am}$  source. The side scan shows a maximal peak position variation of 0.055% and the top scan of 0.075%. Other scans along different axes across the top and side surfaces exhibited even smaller variations. The fluctuation of the uncertainty of the data points in the left plot is caused by varying statistics due to  $\gamma$ -ray absorption in the detector holder (see Figure II-13).

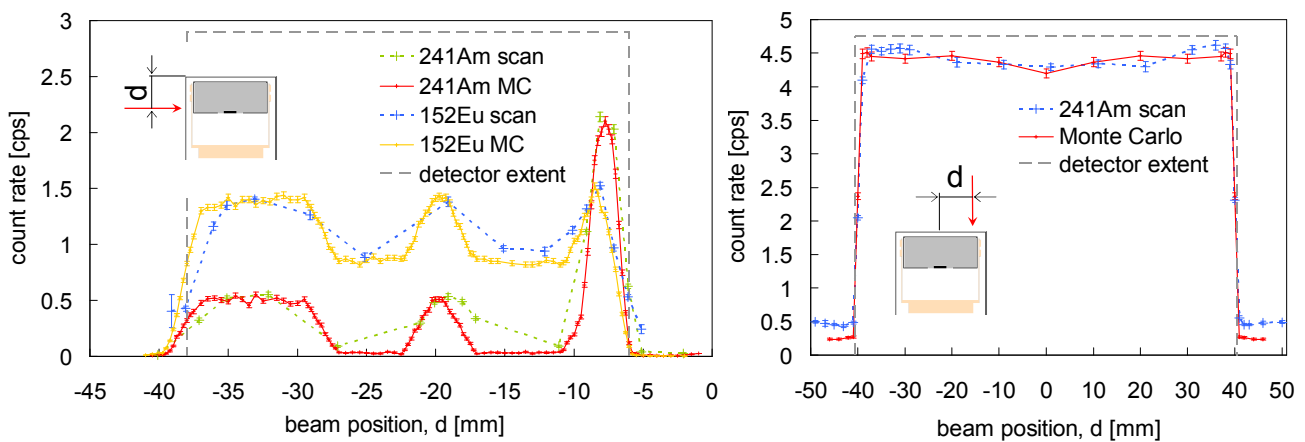


**Figure II-13** Count rate variation in the full energy peak (59.5 keV from  $^{241}\text{Am}$  and 122 keV from  $^{152}\text{Eu}$ ) along the side (left plot) and the top (right plot) surfaces of the BEGe detector, obtained with collimated  $\gamma$ -ray beams. The insets show the beam direction. In case of the side-surface scan, the measurement and simulation results do not agree perfectly, probably due to a slight deviation of the dimensions of the copper detector holder from technical drawings.

The count rate variations in the scan results are displayed in Figure II-13. Along the top surface, the observed variation in the count rate was caused by elastic scatterings of the low energy  $\gamma$ -rays from the surrounding materials of the background shield. The amount of reflected photons reaching the detector depended on the changing position of the collimator, which partially shielded the detector. This caused the slight decrease of the number of counts in the peak when the collimator was aimed at the centre of the crystal (as is visible in the right plot in Figure II-13), covering most of the detector surface. Elastic scattering was responsible also for the residual count rate in the full-energy peak when the beam was pointed off the detector. Both effects were reproduced also in MC simulations of the measurements. A significantly higher count rate variation was observed in the scans along the side of the detector. This was caused by the absorption of  $\gamma$ -rays in the uneven detector holder made of copper. MC simulations of the measurements confirm that the absorption in the holder is compatible with the measurement results. No inhomogeneity in charge collection along the surfaces of the BEGe detector was observed in these measurements. The MC simulations and a part of the measurements were performed by N. Khanbekov, as a part of his internship at MPIK, under the supervision and guidance of the author.

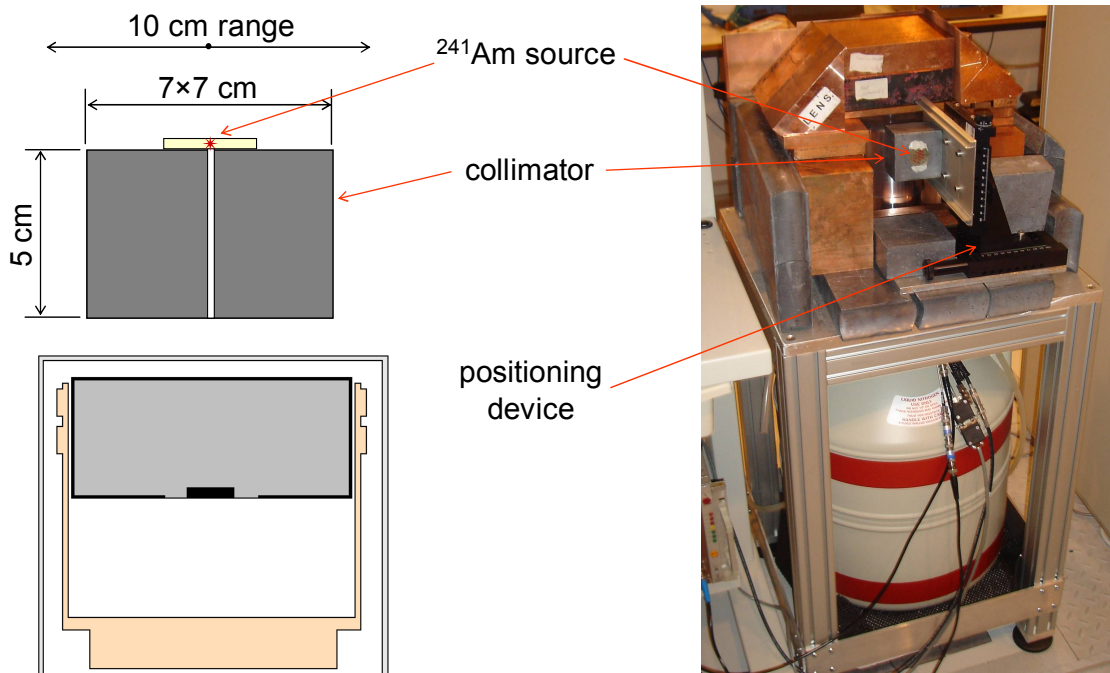


**Figure II-14** **Left:** The geometry of collimator scanning measurements with a  $^{241}\text{Am}$  source, configured for a top surface scan. The collimator with  $\text{Ø}1.5$  mm hole is mounted on a precision positioning device allowing movement along the horizontal axis. **Right:** A photo of the collimator scanning setup configured for a side surface scan. A lead and copper shielding was built around the detector to reduce external background.

As a final test of the concerns about possible dead volumes lacking efficient charge collection, a measurement of the active volume was performed. This was done following the procedure outlined in Section 9 and is illustrated in Figure II-15. Since this procedure requires accurate measurements of the count rate, the analogue DAQ system was used, as the FADC did not have an accurate dead-time determination. First, the dead layer at the top of the crystal was measured, using a ratio of the count rates in the detected  $\gamma$ -lines from an uncollimated  $^{241}\text{Am}$  source. The determined dead layer thickness was  $(0.430 \pm 0.004)$  mm. In the second step, the active mass was evaluated using a  $^{60}\text{Co}$  source. Instead of altering the borehole dimensions, as was done in Section 9, in the case of BEGe the thickness of dead layers on the surfaces of the detector was modified to adjust the active volume. The active mass of the detector was determined to be  $(833 \pm 16)$  g, 95% of total. This would correspond to 0.46 mm of inactive material uniformly distributed on the surface of the detector, in good agreement with the front dead layer determination and with the manufacturer specification (Table II-1).

In the comprehensive series of measurements summarised in this section, no indication of charge collection issues was found with the BEGe detector. The very good energy resolution and the fairly small thickness of the dead layer indicate that the efficiency of charge collection in the tested BEGe detector is competitive with any good quality HPGe detector. From the performed measurements it is apparent that the only inactive volume inside the crystal is the lithium drifted  $n+$  contact, as is normally expected for a  $p$ -type detector.

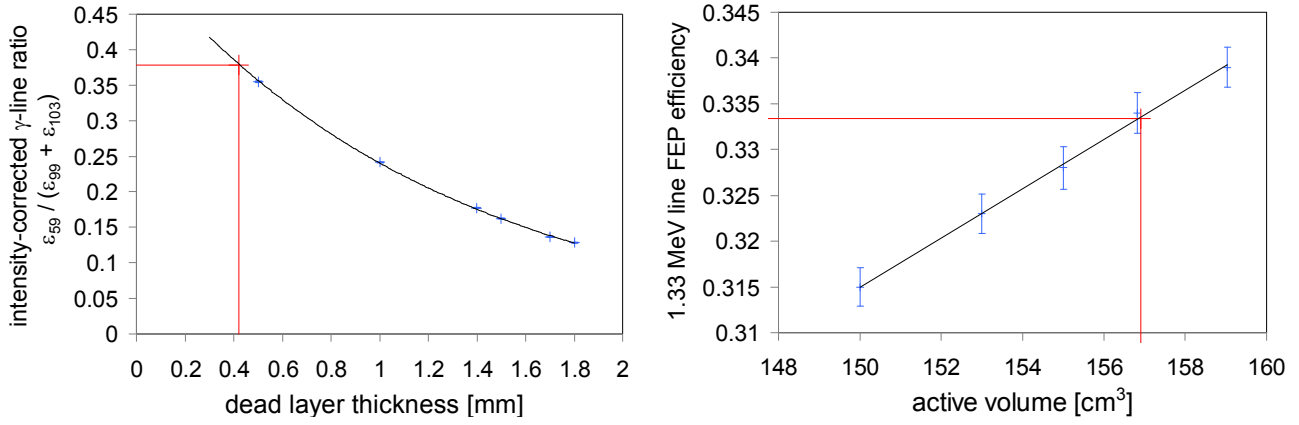


**Figure II-15** Dead layer thickness (left plot) and active volume (right plot) determination. The blue points are MC simulated data with their statistical uncertainties. The black lines are the fit functions. The red lines indicate the measured efficiency (or ratio) and the corresponding interpolated result. The dominant uncertainty of the result comes from the data interpolation, and the source activity uncertainty in case of the active volume determination. N. Khanbekov performed under the guidance of the author the MC simulations and the measurement evaluation. For a description of the method and a discussion of the MC simulation uncertainties see Section 9.

## 12. Pulse shape analysis

The basic ideas behind the analysis of the time structure of the signals from germanium detectors were outlined in Section 3.3. As was noted at the beginning of this chapter, point contact detectors were found to have features enabling very sensitive pulse shape analysis, especially concerning the discrimination of single-site and multi-site events. The BEGe detector was expected to have similar favourable properties due to its similarities with these detectors. As can be seen on Figure II-16, the recorded signals indeed have features which make SSE and MSE easily distinguishable.

The structure of the detector signals can be understood by examining the process of charge collection inside the active volume. The signal development in a germanium detector is described in Section 2.3. The charge induced at the electrode by charge carriers ( $Q^e$  for electrons,  $Q^h$  for holes) was given by the equation (7), repeated here:

$$Q(\mathbf{x})^{e,h} = -q^{e,h} \cdot W(\mathbf{x}) \quad (\text{II-1})$$

where  $q$  is the charge of a charge carrier cluster ( $q^e = -e$ ,  $q^h = +e$ ) and  $W(\mathbf{x})$  is the weighing potential. The pulse shape can be then simulated using numerical calculations for charge transport within the material. To accurately reconstruct the process of inducing charge on the diode electrodes by the moving charge carriers, a full description of the weighing potential within the crystal is necessary. However, this requires detailed knowledge of the geometry of the electrodes, electrical properties of the material, and characteristics of the space charge distribution within the depleted volume. At the time of this writing, the information about the profile of impurity concentration and the exact electrode geometry of the BEGe diode were not available from the detector manufacturer. Still, it is known that the read-out electrode is small, and the weighing potential is expected to be sharply increasing near this electrode, analogously as in point contact detectors. Based on this information I could develop a simple qualitative model to reproduce the main features of the pulse shape.

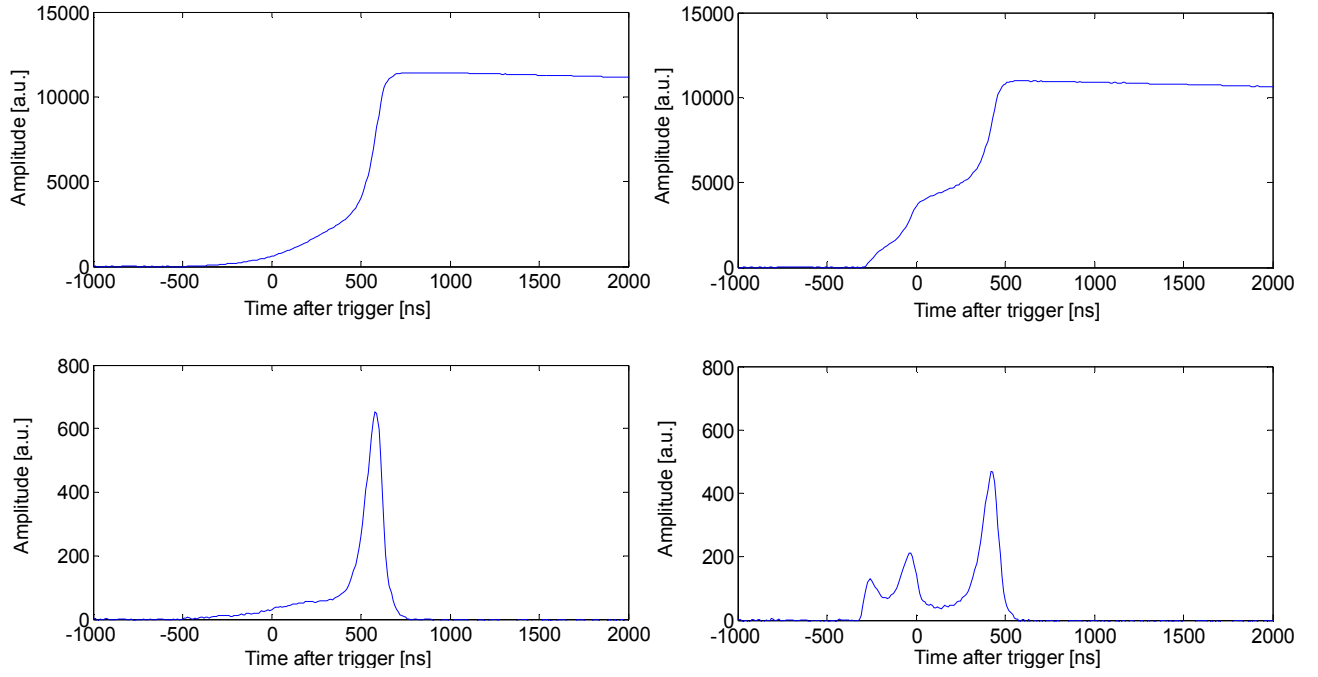


**Figure II-16** Signal traces recorded by FADC (10 ns per point). **Top row:** Voltage pulses from the preamplifier (corresponding to detector charge pulses). **Bottom row:** The same pulses after 50 ns smoothing and 10 ns differentiation (analogous to detector current pulses). **Left column:** A typical candidate for a SSE. **Right column:** A candidate for a multiple-scattered photon induced MSE. Both events had approximately equal energy. The events were recorded from a  $^{228}\text{Th}$  radioactive source.

The simple model assumes a hypothetical detector with 1 cm distance between its electrodes. The calculation is done in a one dimensional approximation, not taking into account the signal distortion by noise, electronics bandwidth, non-zero volume of the energy deposit, charge diffusion, etc. I selected a typical candidate SSE pulse shape from our BEGe detector (see Figure II-16, left) and constructed a suitable arbitrary one-dimensional function, which qualitatively simulates the weighing potential along the particular charge-migration path realised in the selected event. The choice of the function was arbitrary, with a requirement to have a small, almost constant, gradient along most of the path, sharply increasing at the read-out electrode:

$$W(x) = \frac{2}{3} \cdot \left[ \left( \frac{1-x}{1+x} \right)^{10} + \frac{1}{2} \cdot (1-x)^{1.5} \right] \quad (\text{II-2})$$

where  $x$  is the distance from the read-out electrode in cm. The function is normalised to meet the weighing potential boundary conditions [44]:  $W(x_R) = 1$ ;  $W(x_{HV}) = 0$ , where  $x_R = 0$  is the position of the read-out electrode and  $x_{HV} = 1$  cm the position of the HV electrode. The shape of the function (II-2) is shown in the left-hand side of Figure II-17, and is compared to a theoretical weighing potential function of a true coaxial HPGGe detector on the right-hand side. It can be seen that in our model the  $W(x)$  is rising much more sharply near the read-out electrode than is the case for a coaxial diode. The absolute value of the *weighing field*,  $E_w = dW/dx$ , is also shown (in three dimensions the weighing field is  $E_w = \nabla W$ ). Compared to the coaxial detector, the  $E_w$  in our model has a sharp peak at the read-out electrode and is small and almost unchanging in the rest of the volume.

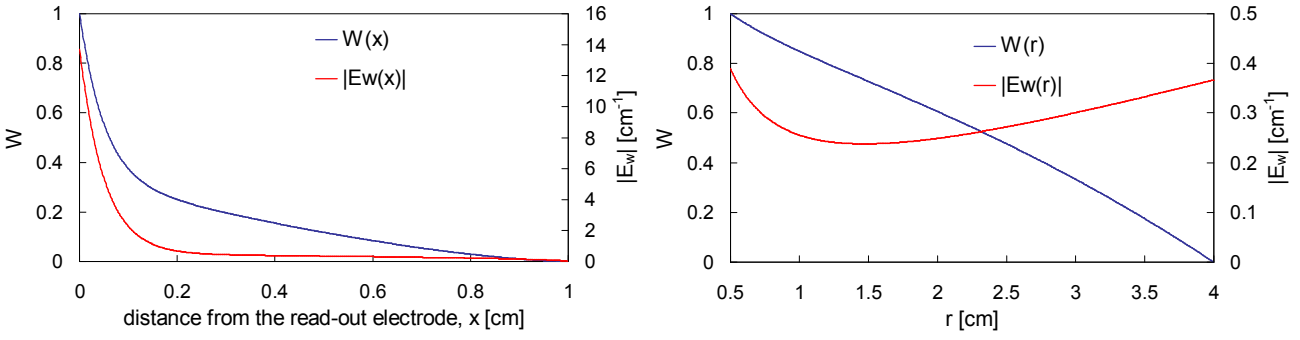


**Figure II-17** **Left:** Weighting potential function  $W$  according to equation (II-2), and the absolute value of the corresponding weighing field  $E_w$ . This function is meant only to qualitatively approximate the shapes of BEGe pulses, and is not based on any real detector configuration. **Right:** Weighting potential and weighing field of a typical true coaxial HPGe detector, calculated from the theoretical electric field equation (3.11) in [39]. The following characteristics were used: impurity concentration  $5 \cdot 10^9 \text{ cm}^{-3}$ , inner electrode radius 0.5 cm, crystal radius 4 cm, bias voltage 3500 V.

The time structure of the charge signal is calculated by accounting for the charge carrier drift:  $x(t) = x_0 + v \cdot t$ , where  $x_0$  is the interaction point. The value of the drift velocity  $v$  used in the calculation was  $10^8 \text{ mm/s}$  for electrons and  $-10^8 \text{ mm/s}$  for holes. Inserting the resulting  $W(t)$  into the equation (II-1), the time development of the charge  $Q(t)^e$  and  $Q(t)^h$  induced at the read-out electrode by electrons and holes, respectively, was calculated. The total charge signal from the detector is then  $Q(t) = Q(t)^e + Q(t)^h$ . When either of the charge carrier clusters reaches its corresponding electrode, it stops moving at that point, and the charge  $Q(t)^x$  induced by it stays constant. The current signal is obtained by time-derivation of the charge signal:

$$I(x)^{e,h} = -q^{e,h} \cdot \frac{\partial W(x)}{\partial t} = -q^{e,h} \cdot \frac{\partial W(x)}{\partial x} \frac{dx}{dt} = -q^{e,h} \cdot E_w(x) \cdot v \quad (\text{II-3})$$

where  $E_w$  is the weighing field. The time dependence  $I(t)$  is then calculated the same way as  $Q(t)$ . The calculated pulse shapes are compared to a typical SSE recorded candidate in Figure II-18. The important features that were reproduced with the simple model are the slow rise, followed by a steep rise in the charge signal, and the significant peak in the current signal. The charge pulse shapes are also comparable to those calculated for the point contact detector in [94].

The recorded SSE candidate signals in Figures II-16 and II-18, and the calculated pulse shapes shown in Figure II-18, feature always a single peak in the current signal. From equation (II-3) it is obvious that the current signal depends linearly on the weighing field  $E_w$ . The current peak is generated when a cluster of charge carriers reaches a peak in  $E_w(x)$ , with its height directly proportional to  $E_w(x)$  and to the charge contained in the cluster. In our simple model,  $E_w$  has a single sharp peak near the read-out electrode, and is small in the rest of the volume (see Figure II-17). In a  $p$ -type detector, the charges collected at the read-out electrode are holes. Thus, for most events only holes are responsible for the current peak and the contribution from electrons is small. Consequently, the peak amplitude will depend only on the charge in the hole cluster, which in turn depends only on the event energy for SSE. The constant current peak amplitude, independent on interaction location, can be seen in the calculated signals in Figure II-18, which have constant energy. The only exception is when the interaction takes place very close to the read-out electrode (the green curve "0.4" in Figure II-18). In this case holes and electrons both briefly drift through the region with high  $E_w$ . Their charges, as well as their velocities, have opposite sign so according to the equation (II-3) the current induced by both charge carrier types has equal sign. Hence their signal adds up, resulting in

a peak higher than the signals from the rest of the volume.

Based on the presented qualitative model, we can make a prediction of expected observable differences between the pulse shapes of single-site and multi-site events. The MSE can be seen as a superposition of two or more SSE happening simultaneously in separated locations in the active volume. In each interaction point a cluster of charge carriers is created and drifts independently towards the electrodes. If the interactions happened at different distances from the read-out electrode, the hole clusters will arrive at different times, each time creating the characteristic sharp current peak. Each cluster will contain only part of the total charge created in the event, therefore the current peaks will be significantly smaller than what would be expected if all holes would arrive at once (like would be the case in a SSE). Thus the MSE can be distinguished from SSE by featuring more time separated peaks in the pulse trace, amplitude of each peak being smaller than that from a SSE of equal energy. A calculated example MSE signal is displayed in Figure II-19, and compared to a SSE and a typical MSE candidate recorded from BEGe.

First attempts at pulse shape discrimination of BEGe signals based on counting peaks in the current signal were not very successful. This was probably mainly caused by noise and bandwidth limitations, making it hard to separate close current peaks in MSE signals. Therefore a discrimination based on measuring the peak amplitude was developed, and will be discussed further in the next section.

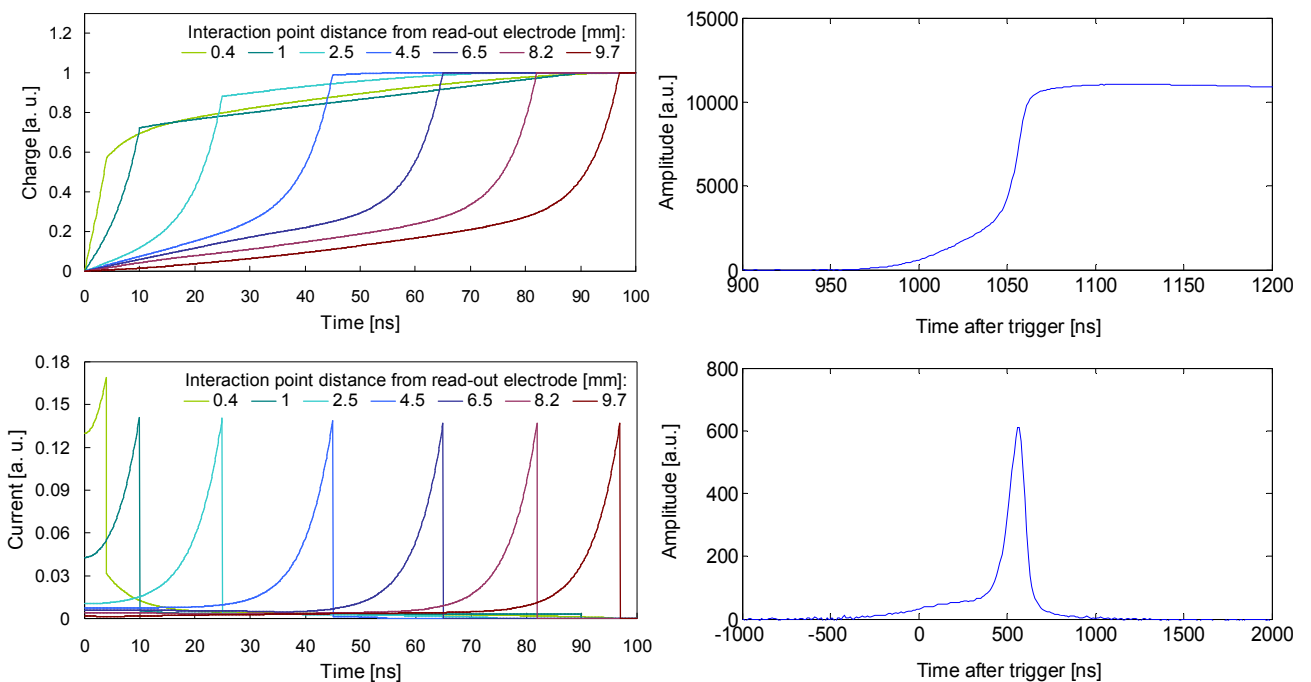


**Figure II-18** Comparison of calculated SSE signals of a hypothetical detector with a weighing potential described by equation (II-2) (left), and a typical candidate for a SSE recorded from BEGe (right). The top row shows charge pulses and the bottom row current pulses. See text for more details of the calculation.

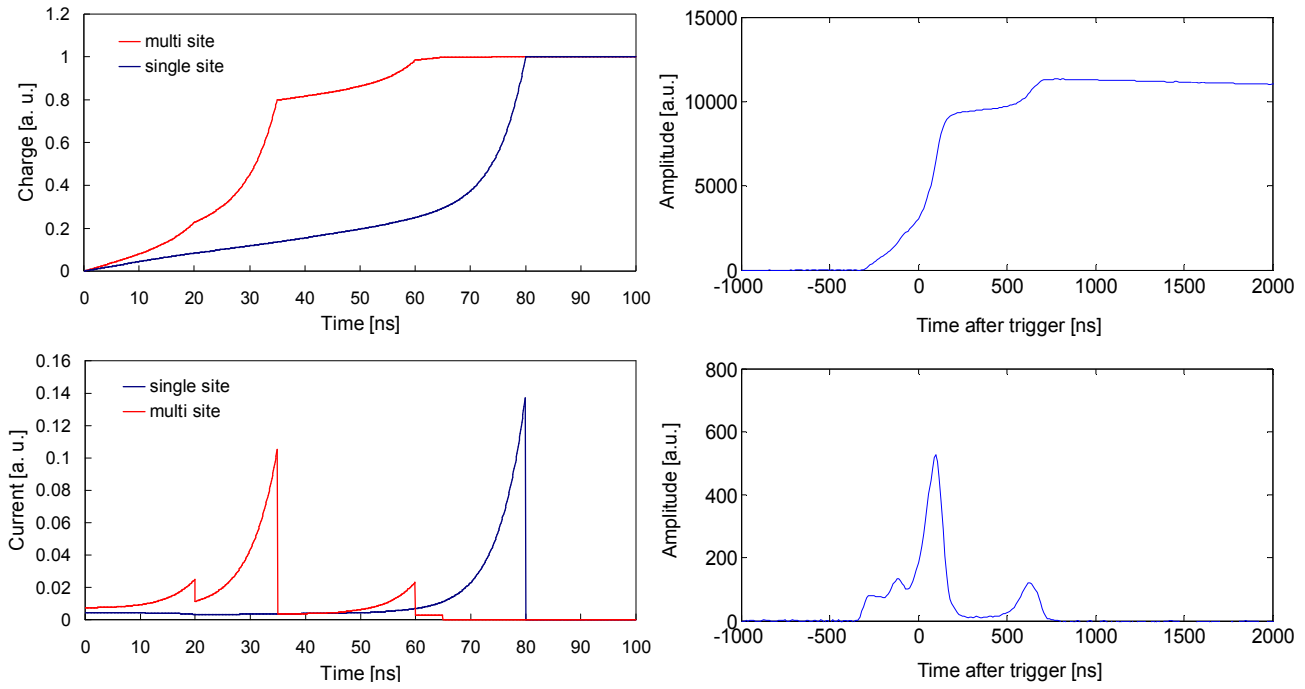


**Figure II-19** Comparison of calculated MSE and SSE signals (left), and a typical candidate for a MSE recorded from BEGe (right). The calculated MSE is composed of three charge depositions, sharing energy in the ratio 0.1:0.75:0.15. The SSE has its energy equal to the sum of the MSE depositions. The top row shows charge pulses and the bottom row current pulses. See text for details of the calculation.

### 13. Experimental pulse shape discrimination

The shape analysis of the BEGe signals was first tested on measurements of  $^{228}\text{Th}$ , because this commonly available isotope presents a source of SSE in germanium detectors. The isotope  $^{208}\text{Tl}$ , a daughter of  $^{228}\text{Th}$ , emits 2614.5 keV  $\gamma$ -rays, which have a significant probability of interaction via  $e^+e^-$  pair production. As explained in Section 2.2, this results in a localised energy deposition followed by an annihilation of the  $e^+$  accompanied by a back-to-back emission of two 511 keV annihilation photons. The two photons are likely to escape the detector without further interaction. When this occurs the absorbed energy will be two electron rest masses smaller than the full  $\gamma$ -ray energy – 1592.5 keV. A peak at this energy (called double escape peak – DEP) is commonly visible in  $^{228}\text{Th}$  spectra. Because it consists of a highly localised interaction of the electron and positron, it contains a high fraction of SSE. Apart from the DEP, single Compton scattering (SCS) events are another way to generate SSE, in which a  $\gamma$ -ray transfers a part of its energy to an electron in a single interaction. These are distributed in the energy spectrum along the Compton continuum, which however contains also a considerable fraction of multi-site multiple Compton scatterings (MCS).

Contrary to SSE, multi-site events are created by a majority of  $\gamma$ -ray interactions at energies above a few hundred keV. Most notable samples with a high MSE content are the full energy peaks (FEP), and the single escape peak (SEP) located at 2103.5 keV in  $^{228}\text{Th}$  spectrum. A single escape event is an  $e^+e^-$  pair production event followed by a full capture of one annihilation  $\gamma$ -ray and an escape of the other. Since it contains a full-energy  $\gamma$ -ray absorption in addition to the localised  $e^+$  and  $e^-$  interaction, it has a higher probability to consist of well separated energy depositions than a FEP.

The experimental measurements with  $^{228}\text{Th}$  were performed with the BEGe detector covered with a lead and copper shield, to minimise background from environmental radioactivity. Especially the 1588 keV  $\gamma$ -line from  $^{228}\text{Ac}$  creates an inconvenient background of MSE events close to the DEP energy. As can be seen in the spectrum in Figure II-21, the external backgrounds were sufficiently suppressed in our measurement setup, and could be considered negligible.

In the following subsection, a SSE-MSE pulse shape discrimination (PSD) method will be described. Next, the SSE acceptance of the method will be validated by its application to DEP event samples and SCS data. Finally, results from a suppression of MSE backgrounds from various sources ( $^{228}\text{Th}$ ,  $^{226}\text{Ra}$ ,  $^{60}\text{Co}$ ) will be presented. A list of the analysed pulse-recording measurements is shown in the Appendix.

### 13.1. Pulse shape discrimination method

The basic concept behind the presented discrimination method of BEGe signals is comparing the energy transferred to the individual clusters of charge carriers to the total energy deposited during the interaction event. In case of a SSE, the whole event energy is contained within one cluster. Following the qualitative description of BEGe pulse shapes, given in Section 12, the amplitude of the current signal will be independent on the place of interaction except of a small region near the read-out electrode. In case of a MSE, the energy is distributed between two or more smaller charge clusters, creating peaks with smaller amplitude in the current signal. For the fraction of events that happen near the electrode, the efficiency of this PSD method is reduced. However this fraction is relatively small due to the small size of the BEGe read-out electrode. This issue will be investigated in detail in Section 13.3.3.

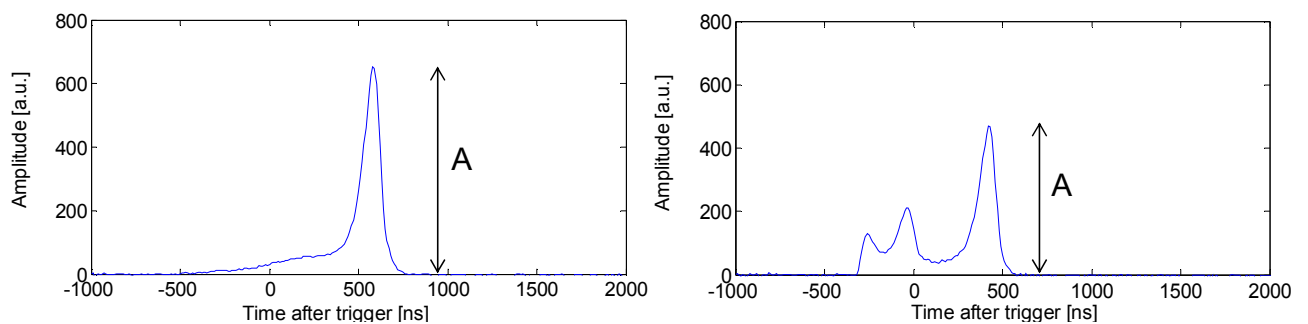


**Figure II-20** Recorded candidate SSE (left) and MSE (right) current signal from the BEGe detector, with an approximately equal energy. The figure shows the amplitude  $A$ , corresponding to the highest energy deposition within an event.

The detector current pulse can be approximately reconstructed by differentiating voltage pulses from the preamplifier (see Figures II-16 and II-18). The differentiation can be performed by a timing-filter amplifier before recording the pulses by FADC, or off-line on recorded raw signals. In the presented analysis, the latter method was used, with 50 ns smoothing followed by 10 ns differentiation. The outlined PSD method allows discrimination based on a single parameter: the ratio of the amplitude  $A$  of the differentiated pulse trace to the total event energy  $E$ , designated  $A/E$ . The amplitude  $A$  (see Figure II-20) is directly proportional to the charge created in the interaction point with the highest energy deposit within an event.

The energy dependence of  $A/E$  from recorded  $^{228}\text{Th}$  events can be seen, together with the energy spectrum, in Figure II-21. The 2614.5 keV  $\gamma$ -line has a relatively small probability of being fully absorbed in a few cm of germanium. Thus the spectrum features a significant Compton continuum composed of single and multiple scattered events. In the  $A/E$  density plot on Figure II-21, the Compton events are separated into two groups: one is concentrated in a narrow line, approximately constant with energy; the other is spread in a broader, lower density region below the line. There are also events above the high-density line, but the event density is very low in that region. These events are assumed to be caused by interactions occurring close to the read-out electrode, and will be discussed in Section 13.3.3.

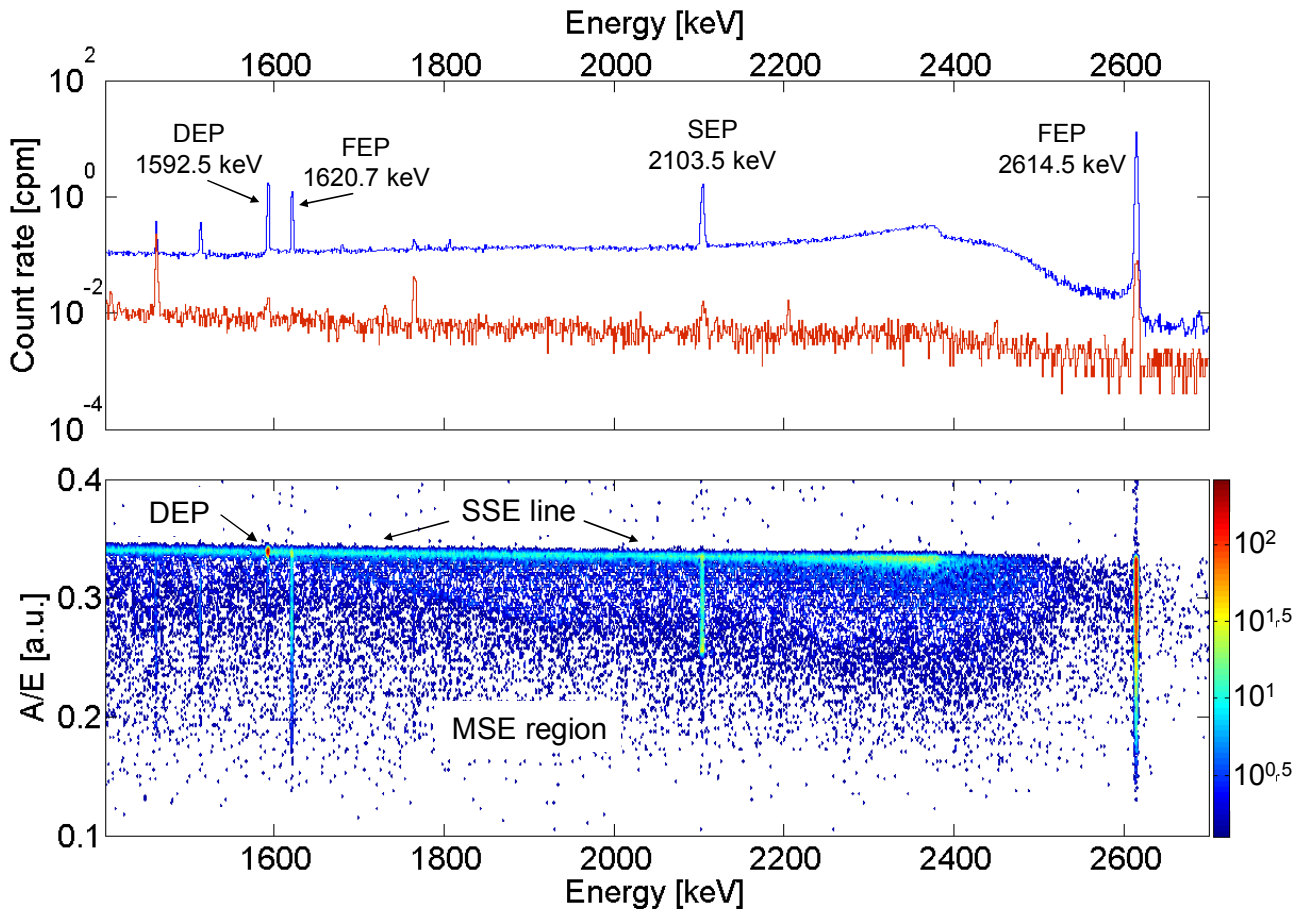


**Figure II-21** **Top:**  $^{228}\text{Th}$  spectrum (blue) recorded with BEGe, with background spectrum (red) for comparison. **Bottom:** Density diagram of  $A/E$  parameter (in arbitrary units, a.u.) distribution in the same measurement, in dependence on event energy. The colour bar on the right indicates in logarithmic scale the number of events in a square of 1 keV  $\times$  0.0025 a.u. The horizontal high density region is referred to as the *SSE line* and the broad area below it is the *MSE region*. The location of the DEP is highlighted.

Based on the earlier discussion about the expected pulse shapes, the  $A/E$  distribution in the Compton-continuum regions can be interpreted as follows. The high density line contains SSE, which result from single-scattering events. The current amplitude  $A$  of these events is directly proportional to the deposited energy. This will be called the *SSE line*. The broader region below the line contains MSE created by two or more times scattered  $\gamma$ -rays. In this case the  $A/E$  is always smaller, because each event is composed of several charge-carrier clusters, each carrying only a part of the total charge signal created. This area will be called the *MSE region*.

This interpretation is supported by the  $A/E$  distribution of events in DEP, SEP and FEPs. In the density plot in Figure II-21, the events at the DEP energy are highly concentrated in a small spot on the SSE line. All FEP have significant tails in the MSE region and the SEP seems to have a particularly high fraction of events in that region as well. A further validation of this interpretation of BEGe pulse shapes will be presented in the Section 13.3.

The aim of our PSD is to keep SSE and suppress MSE, therefore the  $A/E$  cut is selected so that the events in the SSE line are kept and the MSE region is rejected. The distribution of events in the SSE line in dependence on energy was studied by selecting several spectral regions and plotting histograms of  $A/E$  distribution in those regions. A few example plots are shown in Figure II-23. The DEP region was selected within  $1\sigma$  on each side of the DEP in the spectra. This gives good signal to background ratio ( $\sim 93\%$  at the level of background in the recorded spectra). Combined with the fact that DEP events are mostly SSE (typically 4% to 9% of the events are MSE caused by hard bremsstrahlung of the electron or positron [101,102,103]), close to 90% of the data in the selected region are expected to be SSE. Indeed, about 87 - 89% of the counts in the  $A/E$  histograms of DEP regions were found to be concentrated in a Gaussian-like peak positioned on the SSE line (see the 'DEP  $\pm 1\sigma$ ' histogram in Figure II-23). The SSE event distribution was therefore fitted with a Gaussian function.

From the  $A/E$  histograms of Compton regions in Figure II-23 it is evident that the SSE line (determined by the centres of the Gaussian peaks) is not constant with energy. Therefore a PSD cut discriminating SSE and MSE events has to be a function of energy. The shape of this energy dependence was determined from the distributions of several Compton regions at different energies. The  $A/E$  histograms of Compton regions feature a significant MSE tail in addition to the Gaussian peak. The  $A/E$  distribution in each region was therefore approximated by a function consisting of a Gaussian, representing the SSE events, and an exponential tail:

$$f(x) = \frac{n}{s \cdot \sqrt{2\pi}} \cdot \exp\left[-\frac{(x-m)^2}{2 \cdot s^2}\right] + c \cdot \frac{\exp[e \cdot (x-l)] + d}{\exp\left(\frac{x-l}{t}\right) + 1} \quad (\text{II-4})$$

The parameters  $c$ ,  $d$ ,  $e$ ,  $l$  and  $t$  describe the exponential MSE tail, while  $n$ ,  $m$  and  $s$  are parameters of the SSE Gaussian (its integral, mean value and spread, respectively). The function (II-4) fitted to an  $A/E$  histogram is shown in Figure II-23.

The shape of the SSE line function was calculated from the mean values of the Gaussians  $m_i$  for each Compton region at energies  $E_i$ . The dependence could be approximated by a linear function:

$$\hat{m} = a \cdot E + b \quad (\text{II-5})$$

where  $a$  is the slope, and  $b$  the offset of the linear dependence. An example least squares fit to the data and the fit residuals are shown in Figure II-24. The energy dependence (II-5) was calculated from the Compton regions between  $\sim 1.4$  and  $\sim 2.4$  MeV. However, a significant systematic shift was observed with respect to the mean value of the  $A/E$  distribution of the DEP (see Figure II-27 in Section 13.2). It is believed to be caused by the presence of the MSE tail in the Compton data, which interferes with the fit, introducing a systematic bias to the fitted Gaussian function in (II-4). Since they contain similar fractions of MSE, this systematic bias can be assumed equal for all Compton regions. Consequently, it is assumed that the calculated slope of the fitted linear dependence is compatible with the slope  $a$  of the SSE line function (II-5), but the fitted offset is system-

atically smaller than the offset  $b$ . Instead, the Gaussian mean  $m$  of the DEP data was used to fix the offset of the SSE line, because it represents a much cleaner sample of SSE events. The offset in (II-5) is thus given by:  $b = m_{DEP} - a \cdot E_{DEP}$ . The spread of the SSE events around the SSE line was also estimated from the DEP data, as the width  $s$  of the Gaussian in (II-4). The cut function used for PSD can be then written as:

$$CF(E) = \hat{m} - f \cdot s_{DEP} = a \cdot E + m_{DEP} - f \cdot s_{DEP} \quad (\text{II-6})$$

where  $a$  is a least squares fit to the  $m$  values of Compton regions,  $f$  is a factor adjusting the acceptance of SSE events (since the cut is performed only on the lower side of the Gaussian,  $f=2$  results in 97.7% acceptance,  $f=3$  in 99.85% acceptance, etc). The quantities  $m_{DEP}$  and  $s_{DEP}$  are the mean and the spread of the  $A/E$  Gaussian from the DEP events, fitted after correcting the data for the slope  $a$  (see Figure II-25).

The process of calibrating the cut function from the  $^{228}\text{Th}$  data, and its application in PSD is illustrated by the flowchart in Figure II-26. Figure II-22 demonstrates the cut applied to the  $^{228}\text{Th}$  data. The uncertainties of the cut function, its validation, and obtained results will be discussed in following subsections.

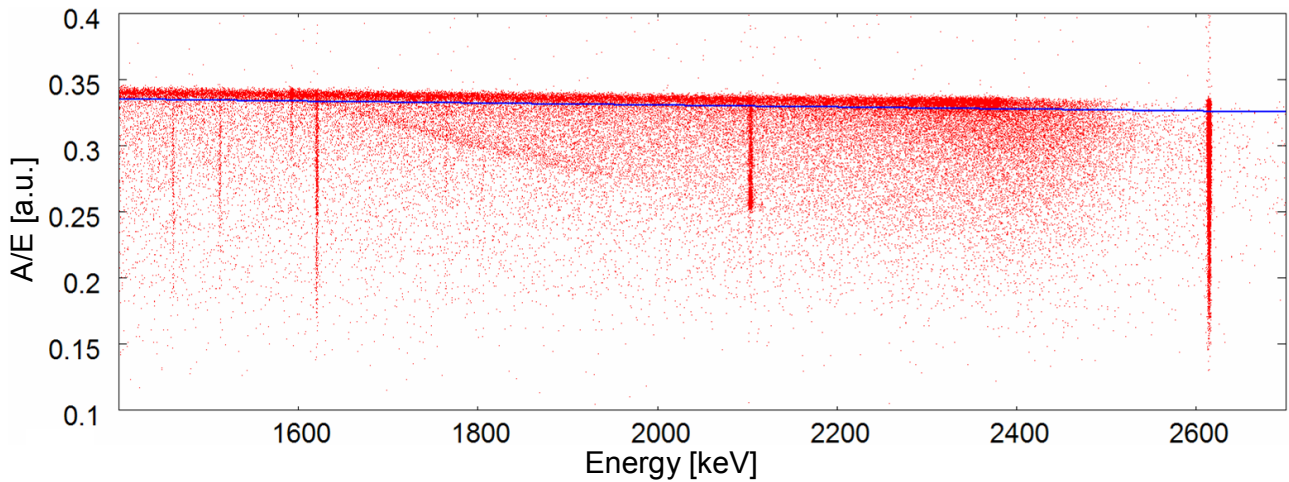


**Figure II-22** Scatter plot of the  $A/E$  parameter in dependence on event energy. The blue line is the PSD cut function (II-6) with  $f=3$  (99.85% acceptance for SSE events). It should be noted that the cut function was determined from data between 1.4 and 2.4 keV and its validity outside of this range was not tested.

### 13.2. Cut function uncertainties and fluctuation

There are several sources of uncertainty in the PSD cut function, introduced in the previous subsection. The slope and the offset are calculated from the fitted  $A/E$  histograms. Their uncertainty is dominated by the statistical uncertainty and the fitting uncertainty of the Gaussian mean  $m$ . The variation of the residuals of the SSE line fit in Figure II-24 is apparently larger than the depicted error bars, which include the statistical and fit uncertainty. It is very likely that the  $A/E$  histogram fit error is underestimated. The real fit error is the dominant source of the variation of the fit residuals and in turn dominates the uncertainty of the determined SSE line slope and offset.

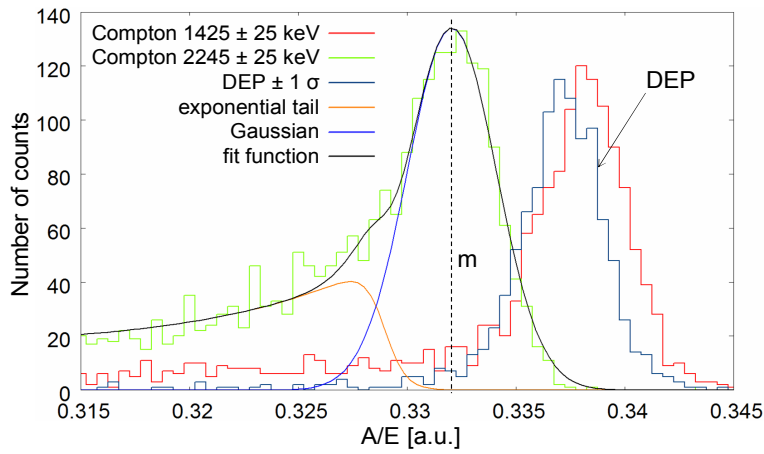


**Figure II-23**  $A/E$  histograms of the data from the DEP and two Compton regions from a single  $^{228}\text{Th}$  measurement. The histogram of the 2.2 MeV Compton is fitted by the function (II-4), consisting of a Gaussian and an exponential tail, with the Gaussian mean  $m$  indicated.

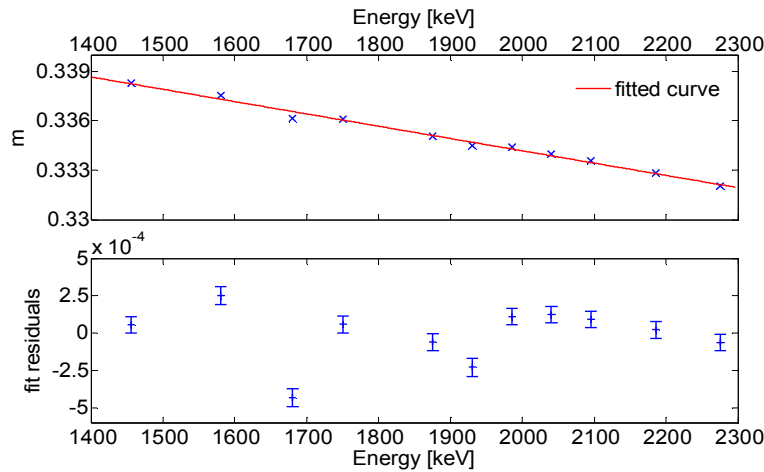


**Figure II-24** SSE line function (II-5) fitted from the mean values  $m$  of the Gaussians fitted to  $A/E$  histograms of several Compton regions (top), and the fit residuals (bottom). The error bars include the statistical uncertainty and the estimated error of the  $A/E$  histogram fit.

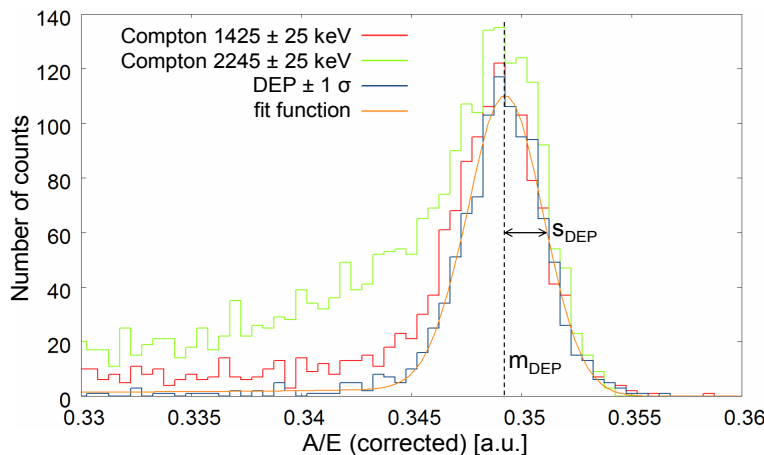


**Figure II-25**  $A/E$  parameter histograms (same data as in Figure II-23) after correcting for the SSE line slope  $a$ . The Gaussian fit of the DEP histogram is shown, with the mean  $m_{\text{DEP}}$  and spread  $s_{\text{DEP}}$  indicated. The parameters  $m_{\text{DEP}}$  and  $s_{\text{DEP}}$  define the offset of the PSD cut function (II-6).

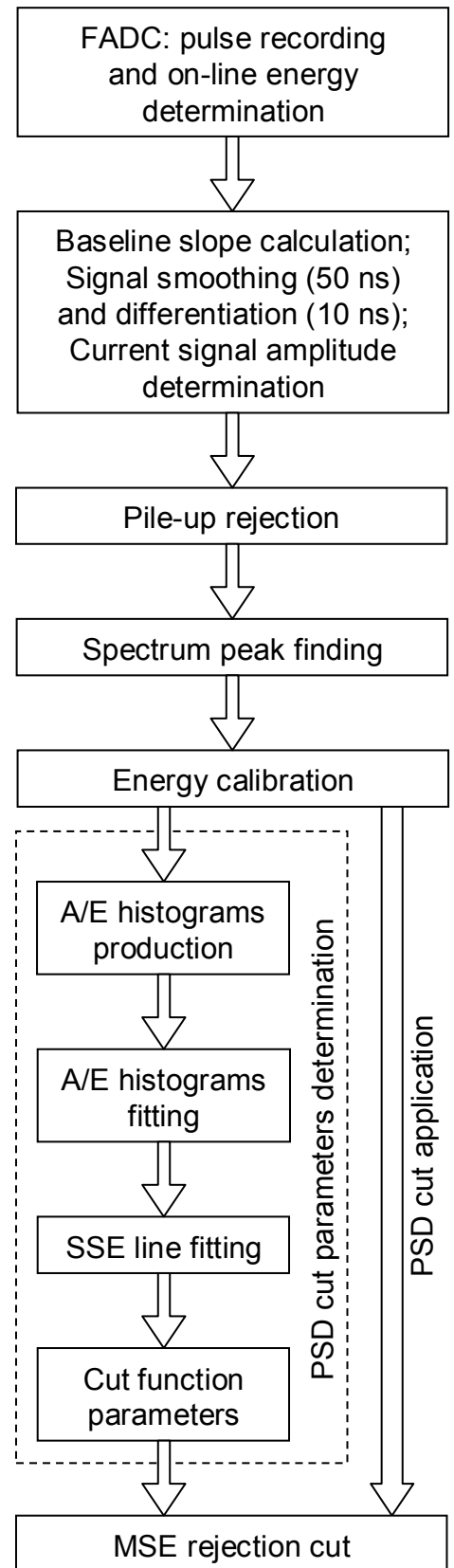


**Figure II-26** Flowchart of the pulse-shape discrimination process. Each box represents a separate code (except of the FADC custom DAQ program, all other were Matlab<sup>®</sup> codes).

Further uncertainty comes from the variability of our DAQ electronics. In Section 11.2.1 it was mentioned that the amplification gain fluctuated significantly with time. After analysing the pulse-shape data acquired with  $^{228}\text{Th}$ , it was found that the SSE line of the  $A/E$  distribution was also not perfectly stable. The data taking runs (see Appendix) were separated into several measurements, each containing on average  $\sim 2 \cdot 10^6$  events. As shown in Figure II-27, the variation in the line offset between individual measurements was larger than the fit error of the  $A/E$  histograms. The difference can be as big as one standard deviation  $s$  of the fitted SSE Gaussian distribution. This fluctuation could be caused, e.g., by variation of the electronic bandwidth. It is planned to investigate further which particular element of the DAQ chain is responsible. To account for the considerable fluctuation between measurements, the offset  $m_{DEP}$  and the spread  $s_{DEP}$  of the cut function (II-6) were determined individually for each measurement.

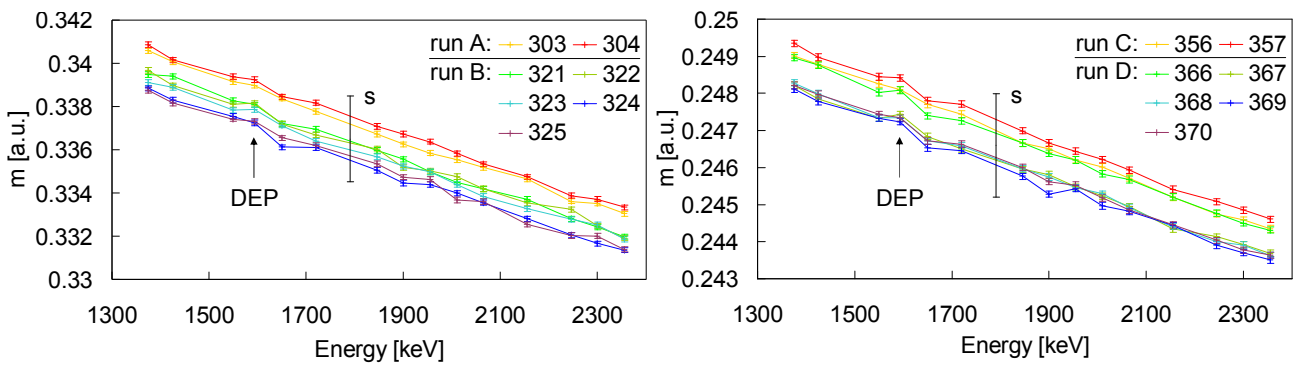


**Figure II-27** Mean values  $m$  of  $A/E$  Gaussians calculated from DEP and several Compton regions in function of energy, for two sets of  $^{228}\text{Th}$  measurements performed with different electronics layout (Left: both preamplifier outputs read out; Right: only one output read out). The error bars represent the fit uncertainty of the  $A/E$  Gaussians. The average width  $s$  of the  $A/E$  Gaussians is also indicated. In all measurements, the  $m$  value of the DEP data shows a systematic offset compared to the Compton data. The data point at the higher energy next to the DEP shows an opposite offset<sup>3</sup>.

Unlike the fluctuation of the SSE line offset, the variation of the slope between the individual measurements within each data taking run (see Figure II-28) was consistent with the fluctuation of data points in the least-squares fit (hence with the  $A/E$  histogram fit error). Thus a weighted mean of the slopes from the individual measurements in one data set could be used to determine the slope  $a$  in the cut function (II-6), applicable to that set.

A much higher difference in the offset occurs between sets of measurements with different electronic layouts. In the measurement set shown on Figure II-27, left, both signal outputs from the preamplifier were read out, while in the set on Figure II-27, right, only one output was used. This probably significantly altered the preamplifier bandwidth, resulting in the observed change of the SSE function offset by about 30%. Also the slope of the function was noticeably different between

<sup>3</sup> This is because at this energy (region  $1650 \pm 25$  keV) a further systematic offset to the fitted  $m$  occurs due to the presence of pair production events of the 2.6 MeV  $\gamma$ -line, interfering with the Gaussian fit. This effect was not corrected, but was included in the systematic uncertainty of the fit. The pair production events always contain a local energy deposition of the created  $e^-$  and  $e^+$ , which can be accompanied by scatterings of annihilation photons. Special cases are the DEP and SEP. The single-site  $e^- e^+$  absorption carries most of the energy in the interaction (1592.5 keV), as the annihilation photons can each contribute a maximum of 511 keV. Thus the current peak  $A$  is constant for these events, thus the  $A/E$  shows a  $1/E$  dependence. These events are visible as an edge of an almost triangular area with a slightly higher density in the  $A/E$  distribution in Figure II-22 between the DEP (1592.5 keV) and the SEP (2103.5 keV).

the two sets, as can be seen in Figure II-28. Therefore the cut function has to be calculated independently every time the electronic layout of the setup is modified.

When applying the cut function to the  $^{228}\text{Th}$  data sets, from which the parameters were calculated, only the  $A/E$  histogram fit uncertainties are dominant, because the fluctuating offset is calculated individually for each measurement. When the PSD is applied to independent data sets, e.g. from different sources not containing any clean SSE sample like a DEP, the cut function determined from the  $^{228}\text{Th}$  runs must be used. In this case the fluctuation arising from the electronics instability has to be taken into account.

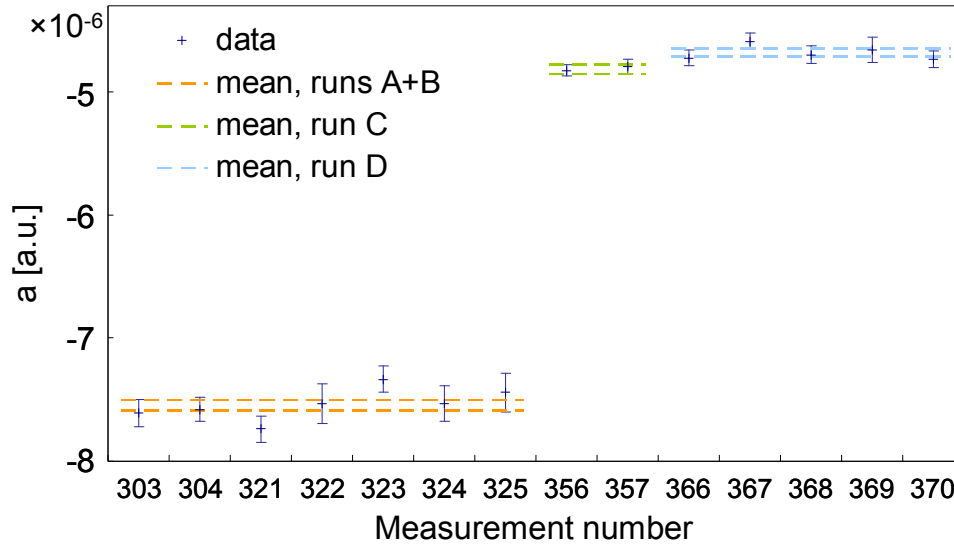


**Figure II-28** The slope  $a$  obtained from individual  $^{228}\text{Th}$  measurements. The dashed horizontal lines are uncertainty intervals of the weighted averages. The error bars represent the uncertainty of the least-squares fit.

### 13.3. Validation measurements

The PSD cut function (II-6) was developed and calibrated from  $^{228}\text{Th}$  measurements, using the pulse shapes of events from Compton regions and the DEP. It was based on the assumptions illustrated by the simple model presented in Section 12. Its general validity and applicability in a  $0\nu\beta\beta$  experiment, needed to be tested on an independent sample with a high fraction of SSE. As was noted previously, Compton continuum contains single Compton scattering (SCS) events, which consist of a single electron interaction, thus are mostly SSE. However they are contaminated by a significant amount of multiple Compton scattering (MCS). The MCS background can be suppressed by kinematically restraining the allowed range of scattering angles. This can be achieved by detecting the scattered  $\gamma$ -rays with a second detector, and recording the data in coincidence. By selecting the scattering angle  $\alpha$ , the energy deposited in BEGe can be adjusted according to the well known Compton scattering equation:

$$E = \frac{E_0 \cdot (1 - \cos \alpha)}{1 - \cos \alpha + \frac{511}{E_0}} \quad (\text{II-7})$$

where  $E_0$  is the initial  $\gamma$ -ray energy. Ability to create SSE at a predetermined energy is advantageous

compared to the DEP, which is fixed in energy. Although the DEP events of  $^{208}\text{Tl}$  have been considered as a good representation of  $\beta\beta$ -decay events [101,102,103], they have different energy than the  $0\nu\beta\beta$ -decay ( $Q_{\beta\beta} = 2039$  keV in  $^{76}\text{Ge}$ ). Since our cut function is energy dependent, it is useful to test the PSD method on a sample of SSE at  $Q_{\beta\beta}$  energy, which can be obtained with SCS. The coincidence measurements of Compton scattering will be summarised in Sections 13.3.1 and 13.3.2.

Another difference between the DEP and  $0\nu\beta\beta$  events is their spatial distribution within the detector. While  $^{76}\text{Ge}$  is distributed homogeneously in the detector material, DEP events are more likely to occur close to edges, because there the probability of the annihilation  $\gamma$ -rays escaping without interaction is higher. It is already evident from the expected signal shapes discussed in Section 12 that our PSD method is mostly independent on the event location, however loses efficiency for events located close to the high weighing potential region near the signal contact. A test of spatial distribution dependence of the PSD cut can also be provided by the performed SCS measurements, since their geometry differed significantly from the non-coincident  $^{228}\text{Th}$  measurements (see Figure II-44). The resulting effect on the  $A/E$  distributions will be examined in Section 13.3.2. The influence of spatial distribution was further investigated with measurements of a collimated beam of 2614.5 keV  $\gamma$ -rays, which will be summarised in Section 13.3.3.

### 13.3.1. Coincidence setup for single Compton scattering measurements

A photo and a scheme of the setup used for SCS measurements is shown in Figure II-29. One of the HPGe spectrometers in MPIK Low-Level Laboratory, Dario (previously used for  $\gamma$ -ray screening), was mounted on a movable table with an adjustable height. By adjusting its position relative to the BEGe detector, the mean angle of single-scattered  $\gamma$ -rays could be selected, as well as its allowed spread, which affects the width of the constrained SCS energy region. A lead and copper shield was stacked between the source and the Dario detector, to avoid direct detection of  $\gamma$ -rays from the source. The 2614.5 keV  $\gamma$ -rays from a 250 kBq  $^{228}\text{Th}$  source were used in the measurement. The lead/copper shielding was sufficient to absorb this large  $\gamma$ -ray flux, and no worsening of Dario background count rate was observed with the source. The source had an unobstructed view on the BEGe detector. With this arrangement,  $\gamma$ -ray scattering events were distributed in the whole volume of the BEGe crystal. The relatively loose constraints on the scattering angle allowed a reasonable coincident count rate, but provided less protection against MCS, compared to a setup with a collimated beam (as in, e.g., [93,104]).

The strong radioactive source in a small distance caused a significant count rate in the BEGe detector. The coincidence rate was only a fraction of that, but the high flux of  $\gamma$ -rays caused a high probability of signal pile-ups. Pile-up rejection described in Section 11.1 was applied, removing  $\sim 20\%$  of the events recorded in the coincidence measurements.

The coincidence check was performed in two steps. First, the DAQ software of the FADC was modified to trigger on the events occurring in both detectors within 4  $\mu\text{s}$  wide coincidence window. Signal traces from both detectors were recorded. The second step of the coincidence selection was done off-line, using the differentiated pulse traces (50 ns smoothing followed by 10 ns differentiation). The position of the maximum was determined in the signals from both detectors, and the difference between the positions was calculated. The resulting histogram of the timing difference is

shown in Figure II-30. A flat background coming from random coincidences can be seen, along with a peak containing the true coincident events. The maximal time difference of the true coincidences is equal to the maximal charge collection time of BEGe ( $\sim 1 \mu\text{s}$ ) plus the maximal charge collection time of Dario ( $\sim 500 \text{ ns}$ ). The peak in the timing difference histogram shown in Figure II-30 is consistent with this expectation, having approximately  $1.5 \mu\text{s}$  width (taking into account the tail to the left side). The peak in the Figure II-30 is asymmetrical, because BEGe pulses have an increased probability of long charge collection time compared to Dario pulses. This is due to the fact, that the ratio of the detector volume to the read-out electrode size is larger in BEGe than in Dario. Hence the charge carriers are more likely to travel over longer distances in BEGe.

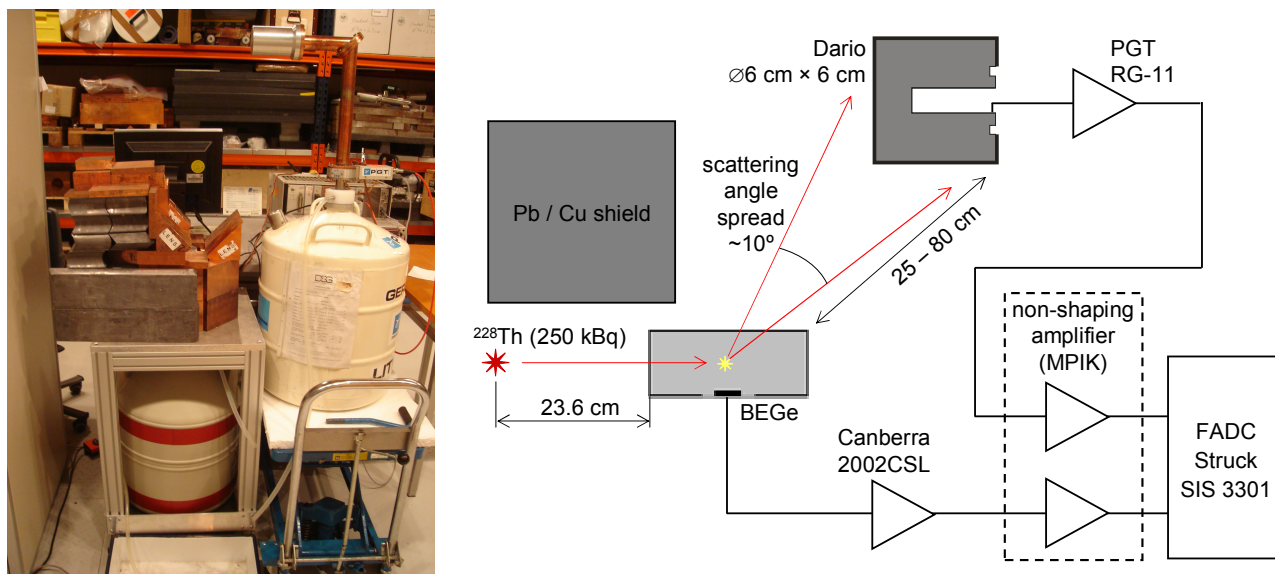


**Figure II-29** **Left:** A photo of the coincidence measurement setup. The Dario detector is positioned on a movable table with adjustable height, allowing to select different scattering angles. The spread of the scattering angles can be also altered, by changing the relative distance of the detectors. **Right:** A scheme of the coincidence measurement setup, showing the electronics layout and the geometry of the measurements.

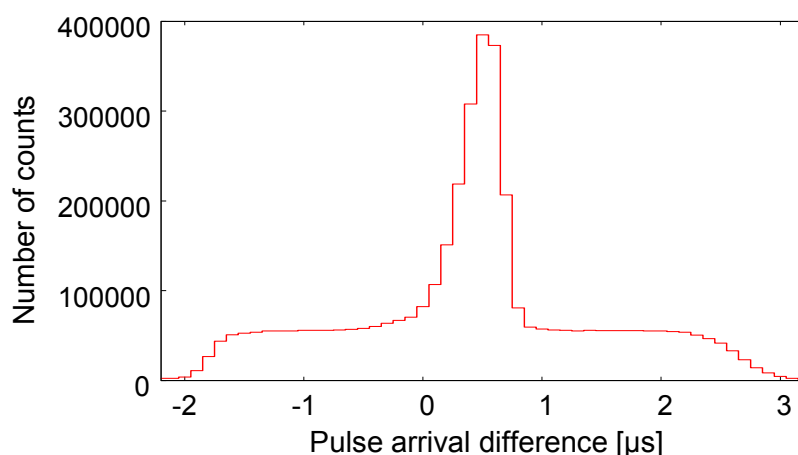


**Figure II-30** Current-signal peak arrival time difference (BEGe signal arrival time after Dario signal) histogram (cumulative for all coincidence measurement runs). Off-line coincidence selection was performed by selecting a  $1.6 \mu\text{s}$  window around the peak in the histogram.

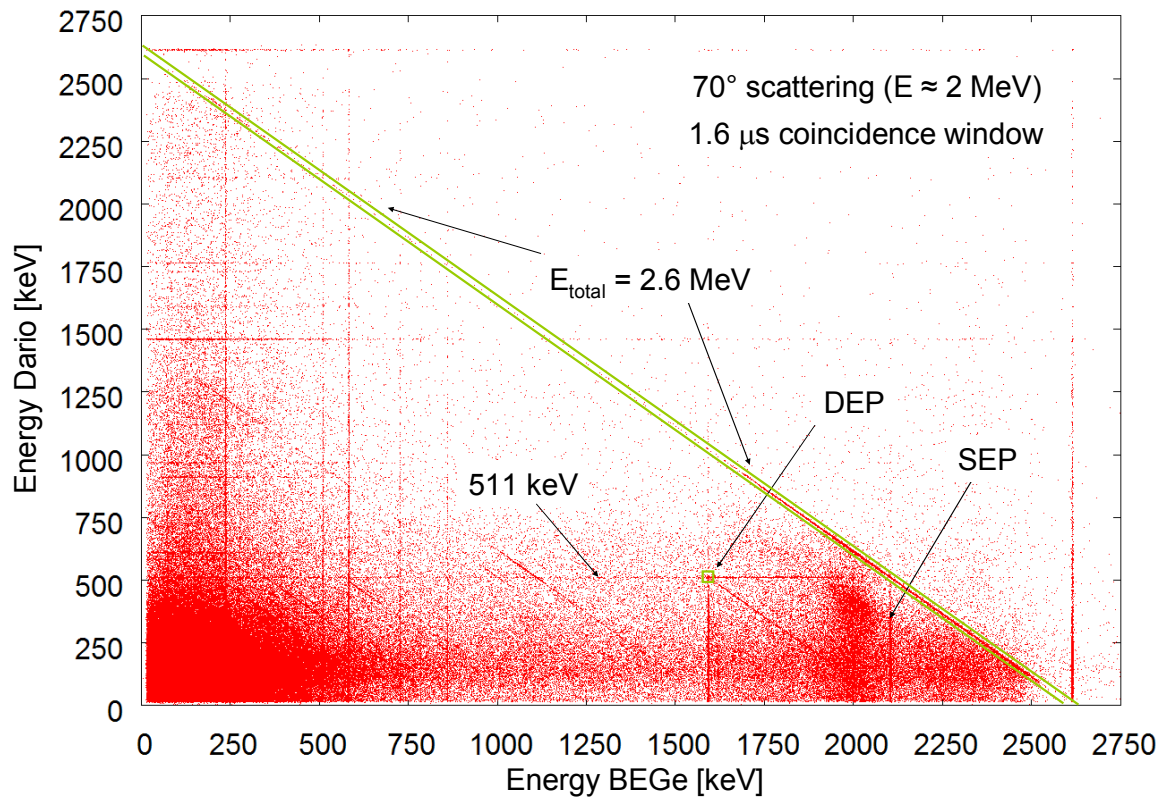


**Figure II-31** Scatter plot of coincident event energy in the 70° Compton scattering run. The selection of the full summation ( $E_{total} = 2.6$  MeV) data set is indicated by the green lines, and the coincident DEP data set by the green box. An increased density of events is visible around 2 MeV energy in BEGe, corresponding to  $\sim 70^\circ$  scattered  $\gamma$ -rays. The vertical and horizontal straight lines at  $\gamma$ -line energies occur due to random coincidences between BEGe and Dario.

After selecting the true coincidences, two data sets were prepared using different energy cuts. The energy cuts and other noticeable features are highlighted in the coincident BEGe-Dario energy scatter plot in Figure II-31. These were the *full summation cut* and the *coincident DEP cut* data sets. Another data set was obtained by taking an asynchronous timing cut, selecting only random coincidence events (the flat continuum in Figure II-30). This was the *random coincidence* data set. All three data sets were calculated separately for each coincidence run (40°, 50° and 70° run). After the timing and energy cuts, the rest of the analysis (calculation of  $A/E$  histograms) was equivalent to the analysis of non-coincident data. A flowchart with the scheme of coincident measurement analysis is shown in Figure II-35.

### The full summation data set

In the first set, the scattering events of the 2614.5 keV  $\gamma$ -rays were selected. This was done by requiring that a photon scattered in BEGe is fully absorbed in Dario, equalling the sum of the energy deposited in both detectors to the full 2614.5 keV. The width of the energy cut was on average 10 keV, equivalent to  $\sim 3.5 \sigma$  on each side of the peak. A cut-out of the spectrum of summed energy in both detectors is shown in Figure II-32. It can be seen that the background from random coincidences, from  $\gamma$ -ray cascades (e.g. possible summation of 583 keV and 2614.5 keV  $\gamma$ -rays from  $^{208}\text{Tl}$ ), and from scattering events losing partial energy outside of both detectors, is relatively small.

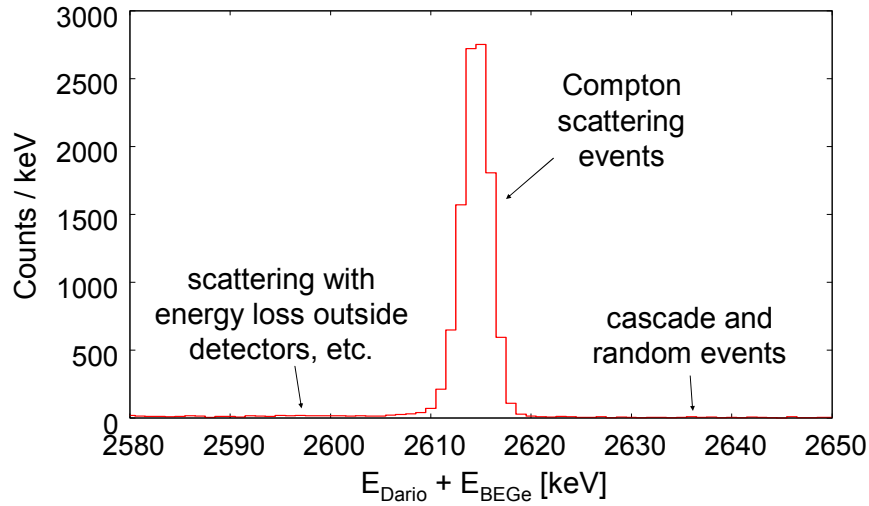


**Figure II-32** Spectrum of summed Dario and BEGe energy (40° scattering run). The FWHM of the peak  $E_{Dario} + E_{BEGe} = 2.6$  MeV was between 3 keV and 3.4 keV, depending on the measurement run. The full summation data set was selected by taking a 3 FWHM wide region around the peak. The spectrum shown includes only events in the approximate energy range of single Compton scattering ( $E_{BEGe} = 1$  to 1.75 MeV for the 40° run spectrum shown).

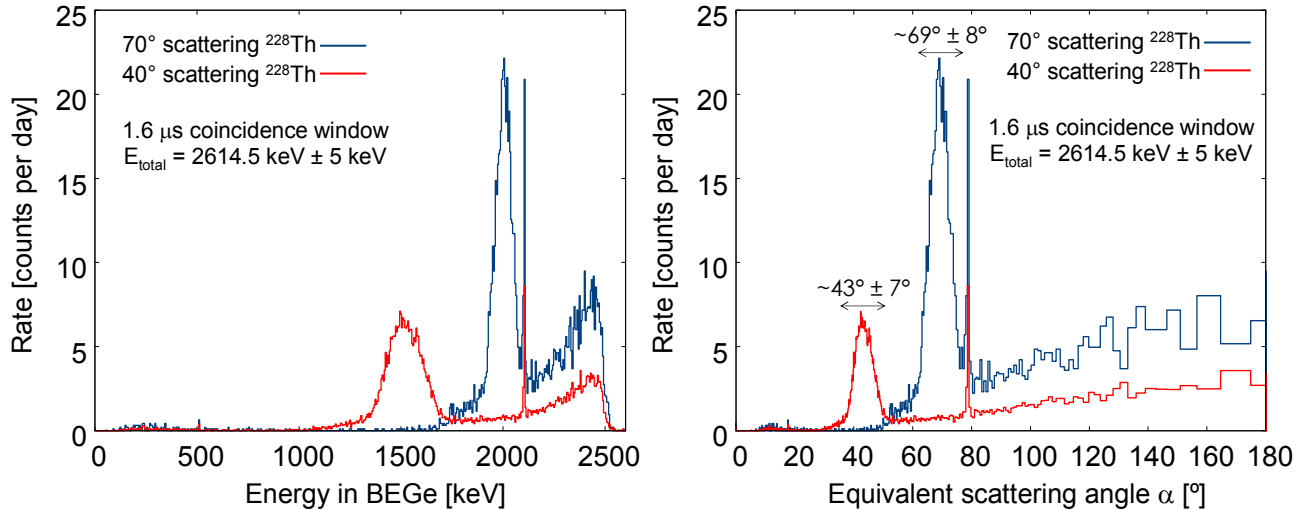


**Figure II-33** **Left:** Energy spectra of the 40° and 70° full summation data sets. The peak at 2103.5 keV is the SEP coincident with 511 keV energy deposition in Dario. Events above 2103.5 keV are dominated by partial SEP events, consisting of an SEP event plus an annihilation photon sharing its energy between BEGe and Dario. **Right:** Equivalent scattering angle spectra of the same data sets, calculated according to equation (II-8). The approximate mean scattering angle in each measurement and the kinematically allowed ranges are indicated.

Figure II-33 shows the spectra of coincident scattering events of 2614.5 keV photons (the full summation sets) in different coincident measurement runs. The equivalent angular distribution, on the right side of the figure, was calculated according to the equation:

$$\alpha = \arccos\left(1 - \frac{511}{2614.5 - E} + \frac{511}{2614.5}\right) \quad (\text{II-8})$$

where  $E$  is the energy deposited in BEGe. The kinematically allowed spread of the angle  $\alpha$  is also indicated. In each measurement, a substantial part of the scattering events is concentrated in a wide peak, consistent with the region kinematically allowed for SCS. The events at energies, which are kinematically forbidden for SCS, are created by multiple-scattered  $\gamma$ -rays. These

represent MSE background to the SCS data.

Other coincident backgrounds contributing to the full summation data sets are background coincidences, from radioactivity in materials surrounding the setup, random coincidences and  $\gamma$ -ray cascade events. The latter two were already shown to be insignificant in Figure II-32. Figure II-34 shows the contribution from background and random coincidences to the full summation cut. They can be both neglected in the energy range of the SCS events.

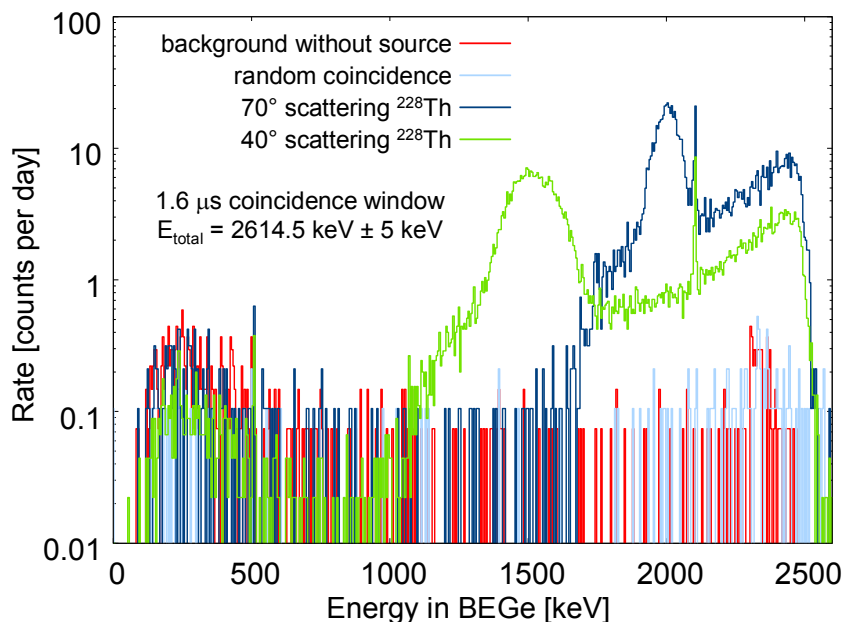


**Figure II-34** Count rate spectra of the full summation data sets from the 40° and 70° coincidence runs compared to background contributions from random coincidences and background coincidences. The random coincident data were obtained by selecting an asynchronous coincidence window. The background coincidences were measured with the coincidence setup without the  $^{228}\text{Th}$  source. The comparison is shown in logarithmic scale for better visibility.

### The coincident DEP data set

The DEP events in coincidence with a 511 keV deposition in Dario were another interesting sample of coincident events. This presents a SSE sample with a substantially reduced Compton background. It was used for a comparison with the non-coincident  $^{228}\text{Th}$  measurements used for PSD development, and for  $A/E$  offset correction of coincidence data.

### The random coincidence data set

The events in this set are selected by an asynchronous coincidence window. Random coincidences mainly occur between the  $\gamma$ -rays from the  $^{228}\text{Th}$  source detected by BEGe and background events detected by Dario. Dario was well shielded from the  $^{228}\text{Th}$  source, therefore random coincidences between two  $^{228}\text{Th}$   $\gamma$ -rays are less likely. This set thus represents a data sample equivalent to a non-coincident  $^{228}\text{Th}$  measurement. It has a different spatial distribution of events than the SCS data in the full summation cut and the coincident DEP data. This data set was used for a test of spatial distribution dependence of the pulse-shape discrimination (see Figure II-37 in the next subsection) and to determine the SSE line slope in the coincidence measurements (Figure II-38).

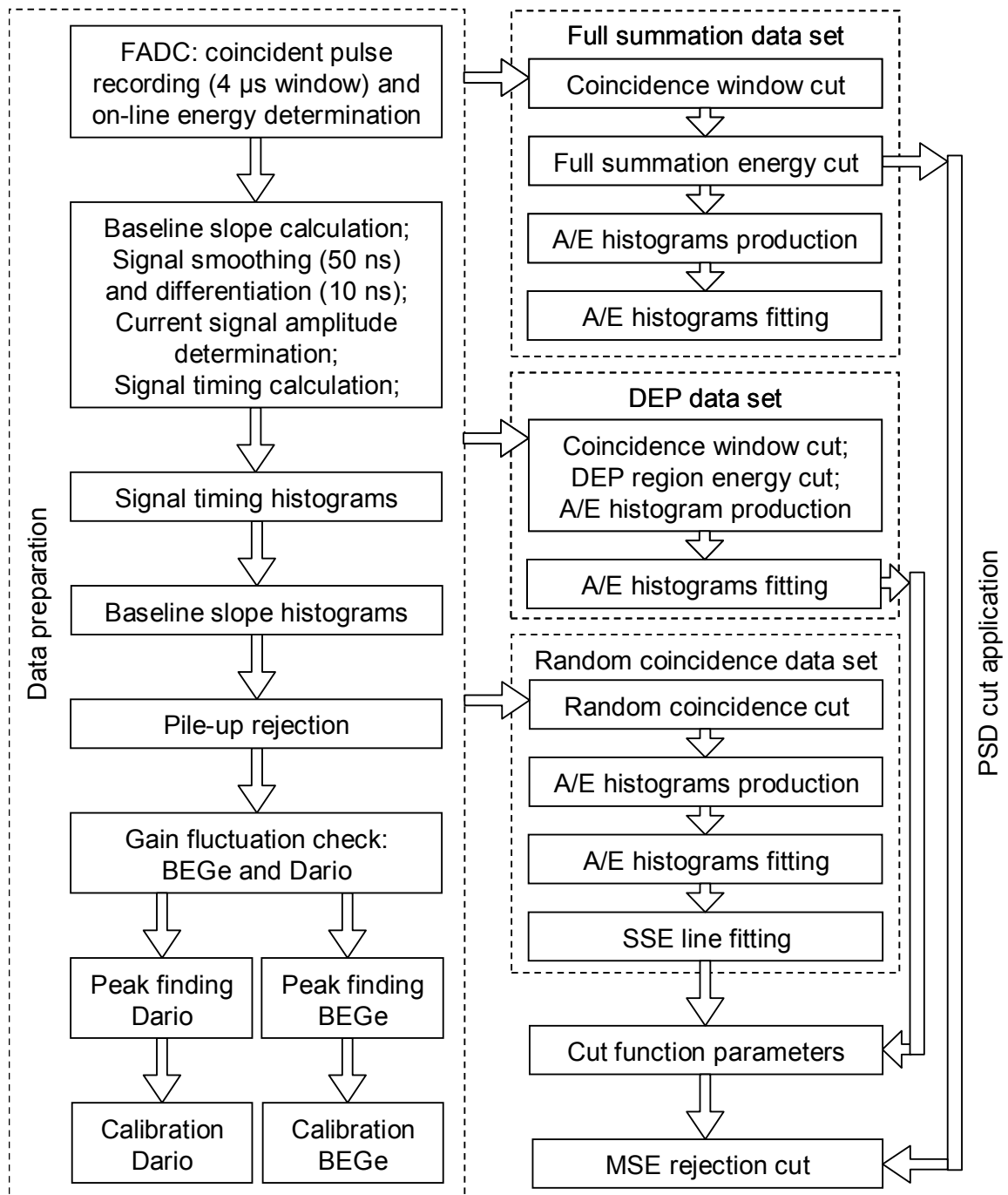


**Figure II-35** Flowchart of the coincident measurement analysis and pulse-shape discrimination. Each box represents a separate code (except of the FADC custom DAQ program, all other were Matlab<sup>®</sup> codes).

### 13.3.2. Coincidence measurements evaluation

The coincidence measurements allow quantitative comparisons of the SSE parameters at different energies, spatial distributions and event topologies. The DEP events in the random coincidence data set, the coincident DEP data, and the SCS data have different spatial event distributions, due to their different kinematic constraints. Furthermore, the SCS events are composed of the interaction of a single scattered electron, while the DEP events consist of an interaction of an electron and a positron, which share equally the event energy. This has a consequence on the probability of

bremsstrahlung emission, which is energy dependent. Thus, these data contain slightly differing fractions of MSE. These comparisons are presented in this subsection.

The energy dependence of the  $A/E$  Gaussian mean  $m$  calculated from the full summation cut data sets of three SCS runs is compared to the random coincidence data and to non-coincident measurement in the left-hand part of Figure II-36. It is apparent that the large offset fluctuation is similar as in the non-coincident  $^{228}\text{Th}$  data, discussed in Section 13.2. The slope of the  $A/E$  function (calculated from the random coincidence data) has slightly changed compared to the non-coincident data set, as can be seen in the right-hand part of Figure II-36. This is due to a modification of the electronics layout by adding the read out of the Dario detector to the DAQ chain. Overall, the energy dependence of the  $A/E$  parameter is similar as in the non-coincident data. The cut function of the coincidence measurements was computed the same way as described in Section 13.1. The slope was obtained from the Compton regions in the random coincidence data, and the offset and spread were determined from the DEP data.

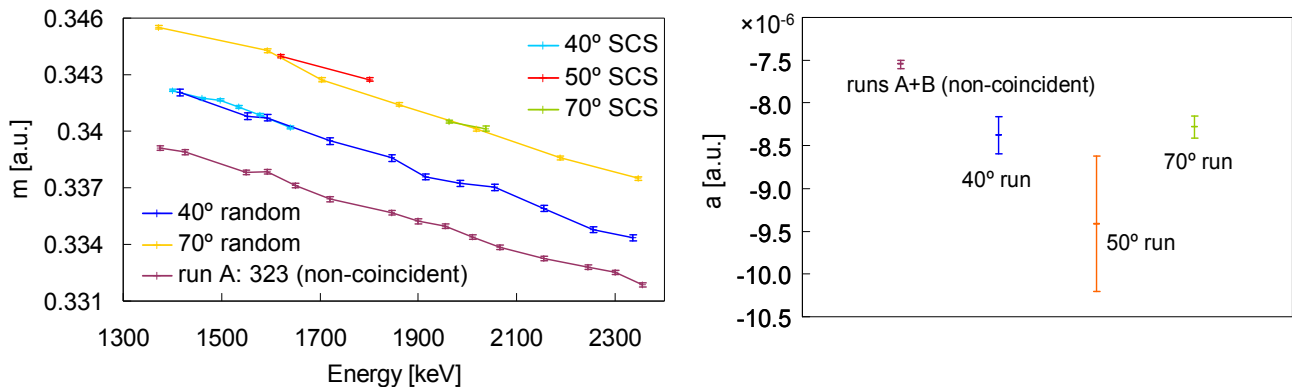


**Figure II-36** **Left:** Mean values  $m$  of  $A/E$  Gaussians calculated from SCS, random coincident and non-coincident data. The error bars represent the fit errors of the  $A/E$  Gaussians and the statistical uncertainty. **Right:** The slope  $a$  obtained from the random-coincidence Compton data of three coincidence measurement runs, compared the weighted average slope of a non-coincident data set. The error bars represent the uncertainty of the least-squares fit.

Figure II-37 and Table II-2 present a comparison of  $A/E$  histograms from the DEP data in the random coincidence data set and in the coincident DEP set, and from the 40° SCS data near the DEP energy. No significant difference between the distributions can be seen in the plot. However, a quantitative comparison of the Gaussian means  $m$  in Table II-2 reveals a small difference between the  $A/E$  histogram from the coincident DEP set and the histograms from SCS and the random coincidence DEP. The  $m$  values of the latter two are equal, but the coincident DEP  $m$  differs by slightly more than the width of the uncertainty interval. Although the difference is tiny, a similar effect is seen also in the data from other coincidence runs (see Figure II-38). It is thought to be caused by a slight deviation of the calculated energy of DEP events, rather than a current-pulse amplitude  $A$  deviation. The DEP events have an increased probability of occurring near the edges of the BEGe detector, therefore in this case there is a higher chance that the signal will arrive with longer delay after the coincident Dario signal. In our setup the signal trace beginning and end are determined by the Dario trigger, thus the more is the BEGe signal delayed, the shorter is its recorded length. This causes underestimation of the signal energy in the digital shaping algorithm, leading to an overestimation of the  $A/E$  parameter. This drawback was, however, not corrected in

the recorded data. Nevertheless, the effect is very small, especially when compared to the electrical instability issues of our setup.

Table II-3 shows a comparison between the relative widths of the fitted  $A/E$  Gaussians in the coincident DEP data from the  $40^\circ$  scattering run ( $\text{DEP}_{\text{coinc}}$ ), and in the DEP data from a non-coincident  $^{228}\text{Th}$  measurement ( $\text{DEP}_{\text{non-coinc}}$ ). The larger widths of the  $A/E$  Gaussian in the coincidence run are caused by a higher fluctuation of the current-signal amplitude, because the data were taken over a much longer time than in the non-coincident measurement (45 days vs. 7 hours). The value in the row  $\text{DEP}_{\text{coinc}}^*$  was calculated as a mean relative width of  $A/E$  Gaussians from subsets of the full  $40^\circ$  scattering run, each approximately one week long. On this shorter time scale the width is consistent between the coincident and non-coincident measurements.

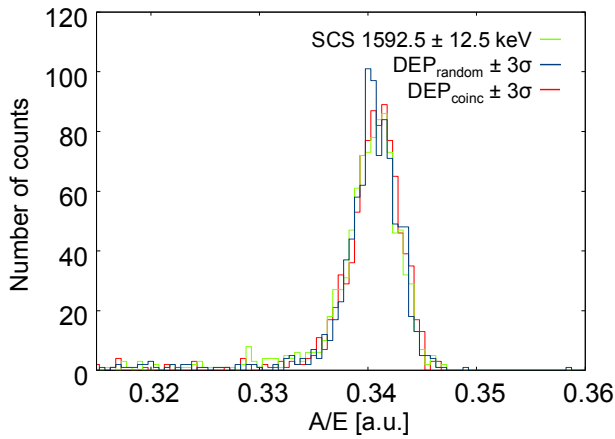


**Figure II-37** Uncorrected  $A/E$  histograms of random coincident and true coincident DEP ( $\pm 2.5$  keV), and SCS at  $1592.5 \pm 12.5$  keV, from the same data taking run ( $40^\circ$  scattering).

**Table II-2** Mean  $m$  and spread  $s$  of Gaussians fitted to the uncorrected  $A/E$  histograms shown in Figure II-37. The uncertainties include statistical and fit error.

Data	$m$ [a.u.]	$s$ [a.u.]
$\text{DEP}_{\text{random}}$	$(34071.2 \pm 9.0) \cdot 10^{-5}$	$(198.5 \pm 9.3) \cdot 10^{-5}$
$\text{DEP}_{\text{coinc}}$	$(34092.1 \pm 8.3) \cdot 10^{-5}$	$(205.9 \pm 8.6) \cdot 10^{-5}$
SCS $40^\circ$	$(34071.5 \pm 8.7) \cdot 10^{-5}$	$(206.1 \pm 9.0) \cdot 10^{-5}$

**Table II-3** Relative widths of  $A/E$  Gaussians from coincident and non-coincident DEP data. See text.

Data	$s/m$
$\text{DEP}_{\text{coinc}}$	$0.604\% \pm 0.025\%$
$\text{DEP}_{\text{coinc}}^*$	$0.510\% \pm 0.028\%$
$\text{DEP}_{\text{non-coinc}}$	$0.517\% \pm 0.023\%$

A comparison of the mean values  $m$  of the  $A/E$  Gaussians of three SCS data sets ( $40^\circ$ ,  $50^\circ$  and  $70^\circ$  run) to the SSE line slope  $a$  is shown in the left-hand part of Figure II-38. The slope was determined from Compton regions in the random coincidence data. The  $m_{\text{DEP}}$  is the mean of the DEP  $A/E$  Gaussian from the coincident DEP sets. It was subtracted from the  $m$  value in each SCS run, to correct for the offset fluctuation. The plot shows also the width of the SSE line  $s_{\text{DEP}}$  obtained from the DEP data. There is a slight systematic deviation visible between the SCS data points and the SSE line slope. It is consistent with the coincident DEP histogram deviation in Table II-2, explained earlier.

The right-hand part of Figure II-38 depicts slope- and offset-corrected  $A/E$  histograms from two of the SCS data sets, which had higher statistics. Small differences between the distributions are observable. The histogram from the  $40^\circ$  SCS run is slightly wider, due to a longer measurement time (45 days) as compared to the  $70^\circ$  run (9.5 days) causing a higher fluctuation of the current-signal amplitude. Apart from that, the  $70^\circ$  SCS histogram seems to have a slightly more visible tail on the MSE side.

The parameters of the  $A/E$  distributions of the different SCS data are quantitatively compared in Table II-4. The Gaussian mean  $m_c$  is corrected for the energy dependence and for offset fluctuation. The values at different energies of SCS events stay equal within the measurement uncertainty. The  $A/E$  Gaussian width was corrected for the current-amplitude fluctuation by averaging values from

measurement subsets, as was explained before. The corrected Gaussian widths seem to suggest a small energy dependence. This was not observed in the Compton data used for the SSE line function determination (Section 13.1). The fit uncertainties caused by the significant MSE tails in those data would overwhelm a weak energy dependence. Also in this case, the slope of the energy dependence is consistent with zero within the uncertainty of measurement (Figure II-39).

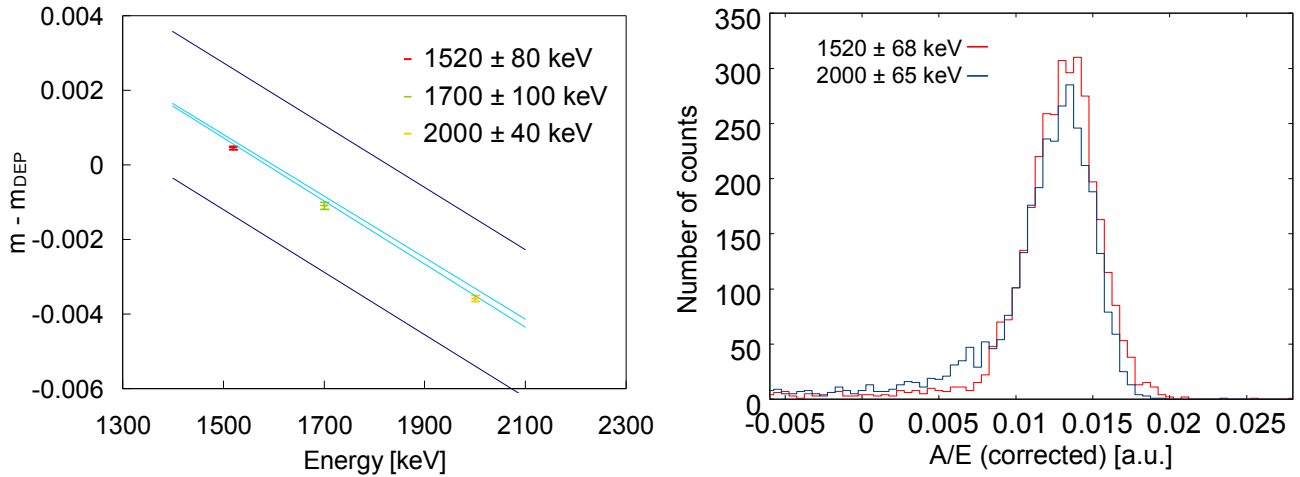


**Figure II-38** **Left:** Comparison of  $A/E$  Gaussian means, corrected for  $m_{DEP}$  offset, from three SCS data sets ( $40^\circ$ ,  $50^\circ$  and  $70^\circ$  scattering) to the SSE line slope determined from random coincidence data. The 65% confidence interval of the SSE line is shown by the light blue lines. The dark blue lines show the  $A/E$  Gaussian width  $s_{DEP}$ . **Right:**  $A/E$  histograms from two SCS data sets ( $40^\circ$  and  $70^\circ$  scattering), with each energy region containing an approximately equal number of events. The data are corrected for  $A/E$  offset and slope.

**Table II-4** The corrected means  $m_c$  of  $A/E$  Gaussians from the three SCS runs, and their spreads  $s^*$ , which are averages calculated from measurement subsets to correct for  $A/E$  offset fluctuation. The  $m$  uncertainties include statistical and fit error. The  $s^*$  uncertainties are root mean square deviations of the average.

Data	$m_c$ [a.u.]	$s^*$ [a.u.]
SCS $40^\circ$	$(1314.5 \pm 7.3) \cdot 10^{-5}$	$(184.0 \pm 2.2) \cdot 10^{-5}$
SCS $50^\circ$	$(1318.4 \pm 6.1) \cdot 10^{-5}$	$(174 \pm 12) \cdot 10^{-5}$
SCS $70^\circ$	$(1312.4 \pm 8.4) \cdot 10^{-5}$	$(197.3 \pm 5.7) \cdot 10^{-5}$

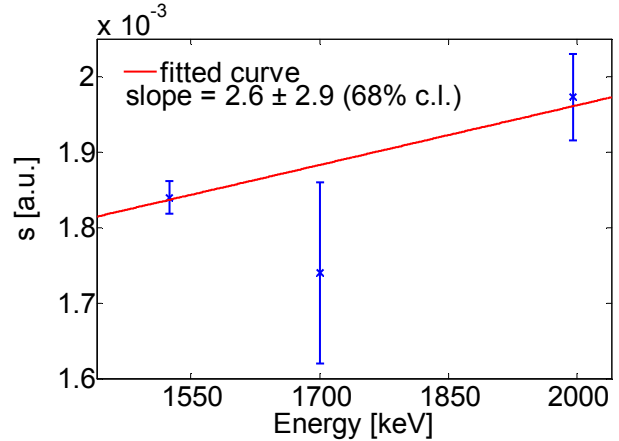


**Figure II-39** Linear fit of the energy dependence of the  $A/E$  Gaussian width  $s$  of SCS data (Table II-4).

### 13.3.3. Collimated beam measurements

The coincidence measurements have already provided pulse-shape data sets with various spatial distributions of events inside the detector. As was discussed in the previous section, no difference was found between the  $A/E$  pulse shape parameter histograms from these sets. However, it was mentioned in the PSD method description in Section 13.1, that the discrimination was expected to be less effective for events occurring close to the read-out electrode. In this case both electrons and

holes drift briefly through the high weighing potential region near the electrode. Their induced current adds up and the peak amplitude  $A$  of the induced current is therefore higher than if only the holes would cross this region, as is the case for events happening further in the detector volume. As a consequence, the  $A/E$  parameter increases, and with a fixed PSD cut value, the acceptance of MSE should increase for events with energy deposition near the electrode. On the other hand, SSE should be principally unaffected, as their  $A/E$  is concentrated mostly above the cut value anyway (the cut is performed only on the lower side of the  $A/E$  Gaussian).

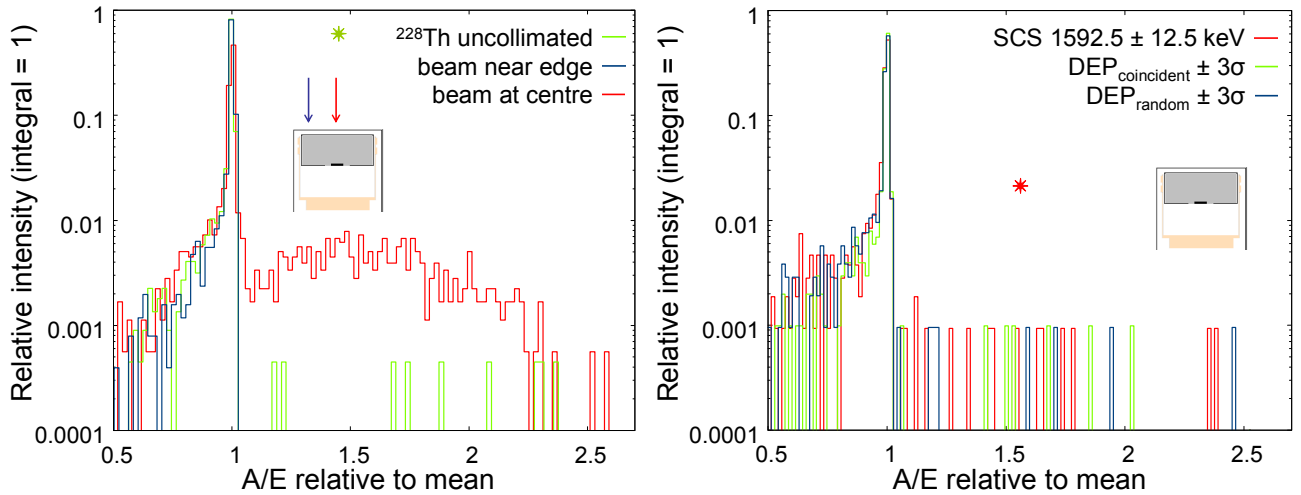


**Figure II-40** **Left:** Comparison of  $A/E$  histograms of collimated and uncollimated  $^{228}\text{Th}$  DEP events. The x-axis values are relative to the Gaussian means of the distributions, the y-axis is relative to the total number of counts in the whole region. The beam locations (arrows) and the uncollimated source position (star) are indicated in the inset, with the colours corresponding to the histograms. **Right:**  $A/E$  histograms of three data sets from the  $40^\circ$  coincidence run.

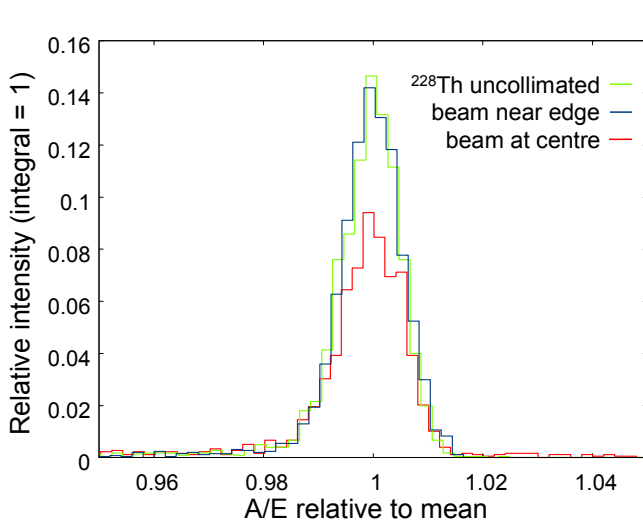


**Figure II-41** Same comparison as in the left-hand part of Figure II-40, with zoom on the Gaussian peak, and with a finer binning. The histograms are relative to the total number of events in the DEP. The "beam at centre" peak is smaller, because a part of the events is shifted to the right side with higher  $A/E$ .

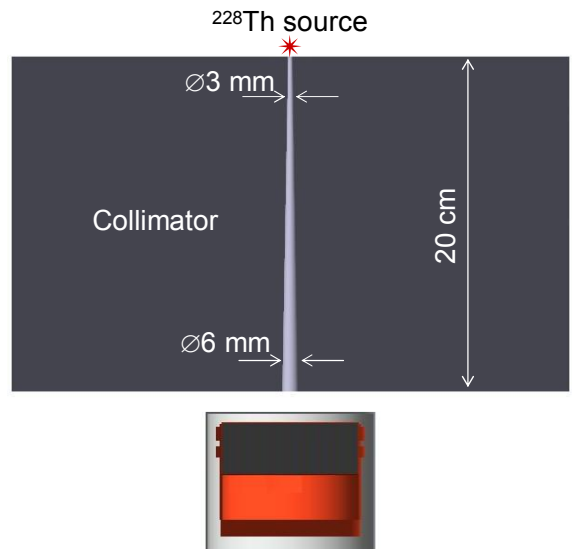


**Figure II-42** The geometry of the collimated  $^{228}\text{Th}$   $\gamma$ -ray beam measurements. The collimator is made of lead. One measurement run was performed with the collimator aimed at the centre of the detector, and one aimed at  $\sim 8$  mm from the edge of the crystal.

To test this effect, measurements of a collimated beam of 2614.5 keV  $\gamma$ -rays were performed. This allowed to create DEP events in a small cylindrical cut-out of the detector volume. To efficiently collimate this high energy  $\gamma$ -ray beam, a 20 cm thick lead collimator was used. The setup is depicted in Figure II-42. The collimator had a  $\varnothing 3$  mm opening on the top, increasing in steps to  $\varnothing 6$  mm at the bottom. Thus the events were concentrated in an approximately  $\varnothing 7$  mm cylindrical volume through the thickness of the detector ( $\sim 0.75\%$  of the total volume). A 250 kBq  $^{228}\text{Th}$  source was used. Two runs were performed, one with the collimator aimed at the centre of the crystal (as in Figure II-42), and one aimed at  $\sim 8$  mm from the edge of the crystal.

The left-hand part of Figure II-40 compares the  $A/E$  histograms of events at the DEP energy  $\pm 1\sigma$  from collimated and uncollimated measurements. The histogram of the beam aimed at the detector centre has clearly more events with  $A/E$  above the Gaussian peak than the other two measurements. In the uncollimated measurement, a few events occur in this region, while in the measurement with the beam near the edge, all events are concentrated in and below the SSE Gaussian. This is in accordance with expectations. A zoom of the histograms, centred on the Gaussian peak is shown in Figure II-41. No other differences between the distributions are observed, except of the smaller fraction of events in the data from the beam at the detector centre. For comparison, histograms from the  $40^\circ$  coincident run (same data as in Figure II-37) are shown in the right-hand part of Figure II-40. In this case the measurement geometry is different, and slightly more events have their  $A/E$  above the Gaussian mean, than in the uncollimated measurement on the left. Despite their somewhat different spatial event distributions, there are no visible differences between the three data sets from the coincidence measurement.

### 13.3.4. Validation measurements discussion

The coincidence measurements provided data sets with high fraction of SSE at different spatial event distributions (the SCS events, DEP events from true and random coincidences), event topology (single electron event in SCS, electron and positron event in DEP), and energy. The comparisons of the DEP and SCS data all show no differences between their  $A/E$  distributions. These results confirm that the DEP represents very well the double-beta decay events. Non-coincident measurements of DEP and Compton region samples are therefore sufficient to calibrate pulse-shape parameters of  $0\nu\beta\beta$ -decay events with satisfactory accuracy.

Only a small difference was found between single electron the scattering events at 1.52 MeV and 2 MeV. The small tail of the  $70^\circ$  SCS histogram in Figure II-38 is so far unexplained, and could appear due to a higher MCS background at higher energies, DAQ system issues, an unforeseen energy dependence of the current-signal amplitude, or the higher fraction of bremsstrahlung events in the interactions of 2 MeV electrons compared to 1.52 MeV. These possibilities can be disentangled in future with an improved setup, and with MC simulations of the SCS interactions to determine accurately the MCS background.

With collimated beam measurements it was found that for events concentrated in a small volume near the read-out electrode the  $A/E$  distributions do differ significantly. A significant part of the events have a higher  $A/E$  value than the events occurring further from the electrode. Since our PSD cut is performed only by removing events with  $A/E$  lower than the Gaussian mean  $m$ , the observed effect does not change the SSE acceptance, but reduces the background rejection power. This will

be demonstrated by the results presented in the following section. Since the energy depositions near the electrode create a current peak at the very beginning of the signal, determining the time structure of the pulse could possibly allow to select these interactions. An additional discrimination technique could be then developed also for such events.

### 13.4. Results and discussion

The double escape peak of  $^{208}\text{Tl}$  was used as a benchmark for single-site event acceptance by our PSD method. The properties of the  $A/E$  pulse-shape parameter distribution of the DEP were tested in several comparisons with data containing high SSE fractions at different energies and spatial distributions. It was concluded that no significant differences were apparent, thus the DEP can be expected to represent acceptably the double beta decay events in tests of the PSD method performance.

Table II-5 presents the accepted fractions of DEP events for a PSD cut at an acceptance factor  $f=2$ . The cut is performed at  $A/E = m - f \cdot s$ , where  $m$  is the SSE Gaussian mean and  $s$  its width (see the equation (II-6) in Section 13.1). The events below this  $A/E$  value are removed and all events above are kept. All results were corrected for the Compton continuum background beneath the peaks, so the values are the net acceptances of DEP events. The mean value of the DEP accepted fraction was  $(89.2 \pm 0.9)\%$ . For a Gaussian distribution, a one-sided cut at two sigma leaves 97.7% of its area. Thus, the total number of DEP events in the SSE Gaussian can be estimated to 91.3%. This falls within the range of previous estimates of the fraction of SSE in the net DEP events, which vary from 91% to 96% [101,102,103], depending on the exact definition of SSE. This reinforces the assumption that the Gaussian peak in  $A/E$  distributions consists of SSE, on which our PSD method is established.

**Table II-5** PSD cut acceptances from various measurements, with an acceptance factor  $f=2$ . All results except of the last two rows are from  $^{228}\text{Th}$ . For an overview of the measurements see Appendix. The results for the four peaks represent net acceptances (Compton continuum is subtracted). The uncertainties include statistical as well as systematic uncertainties, which come from cut parameter fluctuations.

Measurement run	DEP 1592.5 keV	FEP 1620.7 keV	SEP 2103.5 keV	FEP <sup>a</sup> 2614.5 keV	region around $Q_{\beta\beta}$ (2039 keV $\pm$ 35 keV)
A, B	$0.889 \pm 0.018$	$0.104 \pm 0.012$	$0.0764 \pm 0.0058$	$0.0957 \pm 0.0046$	$0.408 \pm 0.012$
C	$0.919 \pm 0.030$	$0.086 \pm 0.020$	$0.071 \pm 0.010$	$0.1025 \pm 0.0042$	$0.433 \pm 0.016$
D	$0.877 \pm 0.017$	$0.1040 \pm 0.0098$	$0.0658 \pm 0.0057$	$0.0948 \pm 0.0038$	$0.402 \pm 0.012$
40° run random coincidences	$0.875 \pm 0.054$	$0.162 \pm 0.039$	$0.076 \pm 0.022$	$0.099 \pm 0.013$	$0.392 \pm 0.030$
40° run coincident DEP	$0.871 \pm 0.056$	–	–	–	–
E (collimated beam at detector edge)	$0.913 \pm 0.017$	$0.104 \pm 0.015$	$0.0639 \pm 0.0063$	$0.1232 \pm 0.0045$	$0.464 \pm 0.012$
F (collimated beam at detector centre)	$0.876 \pm 0.021$	$0.2266 \pm 0.0095$	$0.2582 \pm 0.0066$	$0.2211 \pm 0.0036$	$0.424 \pm 0.011$
G ( $^{226}\text{Ra}$ )	–	–	–	–	$0.206 \pm 0.034$ <sup>b</sup>
H ( $^{60}\text{Co}$ )	–	–	–	–	$0.00925 \pm 0.00077$

<sup>a</sup> the validity of PSD cut was tested only in the energy range between  $\sim 1.4$  and  $\sim 2.4$  MeV. The listed acceptance values of the 2.6 MeV peak may have a systematic error, as it lies outside this range.

<sup>b</sup> a contribution from background  $^{228}\text{Th}$  (representing 40% of events) was subtracted in the computation of this value

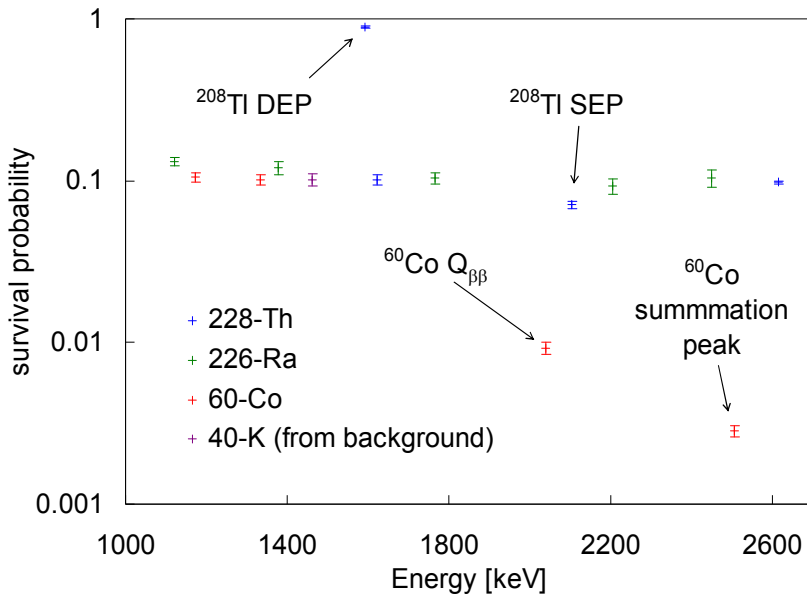


**Figure II-43** Survival probabilities of spectral peaks from different sources after PSD cut. The peaks that are not FEP are highlighted. Plotted in addition to peaks is the survival probability of  $^{60}\text{Co}$  events near the energy of  $^{76}\text{Ge}$   $Q_{\beta\beta}$ . The  $^{228}\text{Th}$  values are weighted averages from all  $^{228}\text{Th}$  results except the collimated and coincidence measurements.

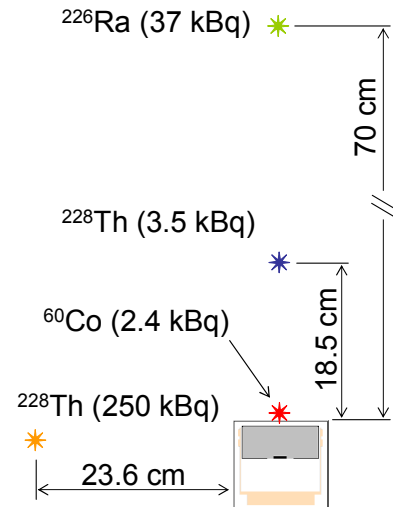


**Figure II-44** Schematic drawing of non-collimated measurements presented in Table II-5 and Figure II-43. The orange star is the source position in coincidence measurements. The other sources are colour coded as in Figure II-43.

The DEP peak acceptance was consistent between all data sets, including the coincident and collimated beam runs. This demonstrates that the spatial distribution of SSE does not significantly affect their acceptance. The large fluctuations of the cut function parameters between the measurement runs are not included in the uncertainties of the shown  $^{228}\text{Th}$  results, since the offset and slope were calculated individually for each measurement, respectively run. The consistent DEP acceptance shows that the electronic layout changes that were performed, and the variability that was encountered during our measurement campaign, do not have an effect on the PSD.

The table also includes survival fractions of the 1.6 MeV peak of  $^{212}\text{Bi}$ , as well as the 2.6 MeV peak and SEP of  $^{208}\text{Tl}$ . The survival fractions of Compton background events around  $^{76}\text{Ge}$   $Q_{\beta\beta}$  energy for  $^{228}\text{Th}$ ,  $^{226}\text{Ra}$  and  $^{60}\text{Co}$  are also shown. These events represent the most important backgrounds for GERDA. All the survival fractions from non-collimated measurements (runs A to D and random coincidence set of the 40° run) are in agreement with each other. We can conclude that the differences between the spatial distributions in these runs do not affect the PSD performance.

The spatial limit of the MSE sensitivity was found to be the small area near the read out electrode, as is demonstrated by the increased survival probabilities of FEP and SEP events in the run F (collimated beam at detector centre). However, this represents only a small fraction of the detector volume, because the events in this run were concentrated in 0.75% of the detector volume (see Section 13.3.3). If we would conservatively assume that all SEP events are multi-site, the rejection of MSE would be  $\sim 74\%$  even in this case. Assuming a perfect MSE rejection in the rest of the detector, the "effective" thickness of the region where the PSD is inoperative can be then estimated to be  $< 8$  mm from the read-out electrode. The electrode size is not known, but assuming its diameter is less than 10 mm, and that the thickness of the ineffective region is equal on all sides, an exceedingly conservative limit on the volume with ineffective PSD would be  $< 2.7\%$  of the total active volume. In addition it can be presumed, that with further investigation of BEGe pulse shapes,

the PSD efficiency can be improved even in this region, as was suggested in Section 13.3.4. It is evident that the spatial limit of our PSD is not a significant concern.

The survival probability of Compton background events around  $Q_{\beta\beta}$  energy from the run E (collimator at the edge) is also different. However, this is likely only due to kinematical constraints, since at the detector edge the photons have a higher probability of escaping after first scattering. This causes a higher SSE fraction in the Compton region in this measurement geometry.

Example spectra before and after the PSD cut are shown in Figures II-45 to II-47. Figure II-43 gives the acceptance fractions of different  $\gamma$ -ray peaks in dependence on energy. All full energy peaks, except for the lowest energy (1120 keV) peak, feature constant acceptance fraction. This is in agreement with MSE fraction measurements and simulations performed in past [61]. The SEP has a smaller acceptance than the FEPs (7% compared to 10%). This is due to larger fraction of MSE in this peak (see the beginning of Section 13 for more explanation). Also shown is the acceptance of  $^{60}\text{Co}$  events at  $Q_{\beta\beta}$  energy of  $^{76}\text{Ge}$ , which is less than 1%. These events are created by the summation of the 1.17 MeV and 1.33 MeV cascade  $\gamma$ -rays of  $^{60}\text{Co}$ . Since the two photons are angularly correlated, they are unlikely to be emitted in the same direction. The summation events thus consist of two considerably separated  $\gamma$ -ray interactions, thus are much less likely to be detected as an SSE than single-photon events.

The PSD cut results from coincident Compton scattering measurements are shown in Table II-6 and illustrated in Figure II-48. The results are not corrected for MCS background contribution. A future MC simulation of the coincident scattering setup can be used to estimate the fraction of multiple-scattered photons in the coincidence data. This would provide an improved test of the PSD acceptance of  $0\nu\beta\beta$ -decay events.

**Table II-6** PSD cut acceptances from coincidence measurements, with an acceptance factor  $f=2$ , applied to the full summation data sets. The results represent gross acceptances (without MCS background subtraction). The uncertainties include statistical as well as systematic uncertainties from cut parameter fluctuations.

Measurement run	Energy [keV]	Acceptance
40°	1525 ± 100	0.826 ± 0.045
50°	1995 ± 50	0.726 ± 0.020
70°	1712.5 ± 150	0.744 ± 0.049

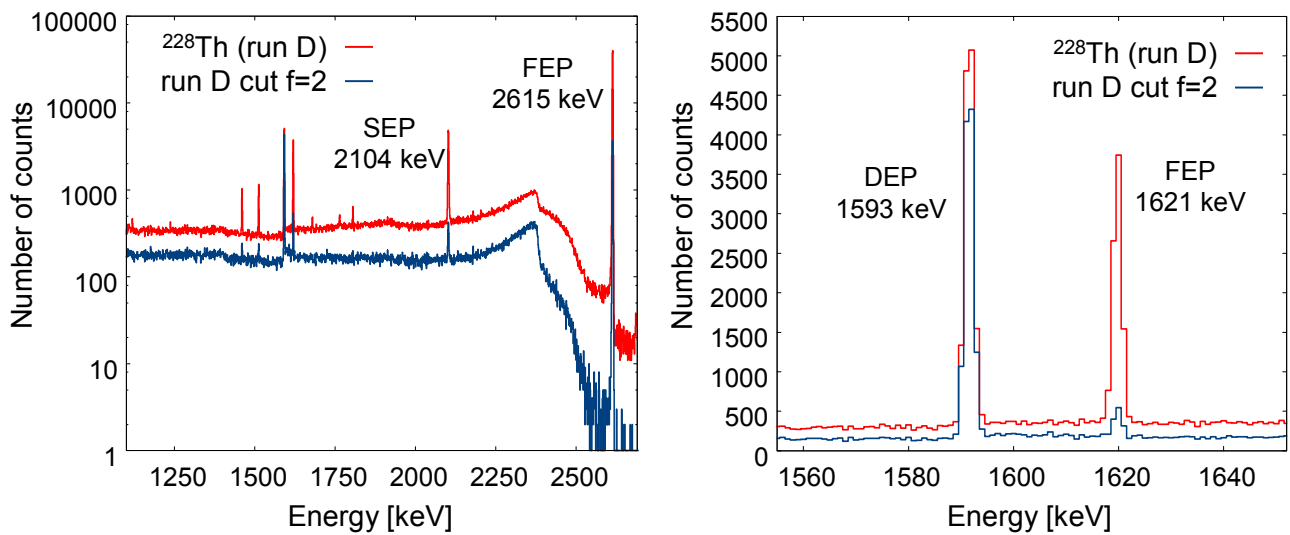


**Figure II-45** Left: Comparison of a  $^{228}\text{Th}$  spectrum before and after the PSD cut with an acceptance factor  $f=2$ , in logarithmic scale. Right: Zoom in linear scale on the  $^{208}\text{Tl}$  double escape peak and 1.6 MeV full energy peak of  $^{212}\text{Bi}$ .

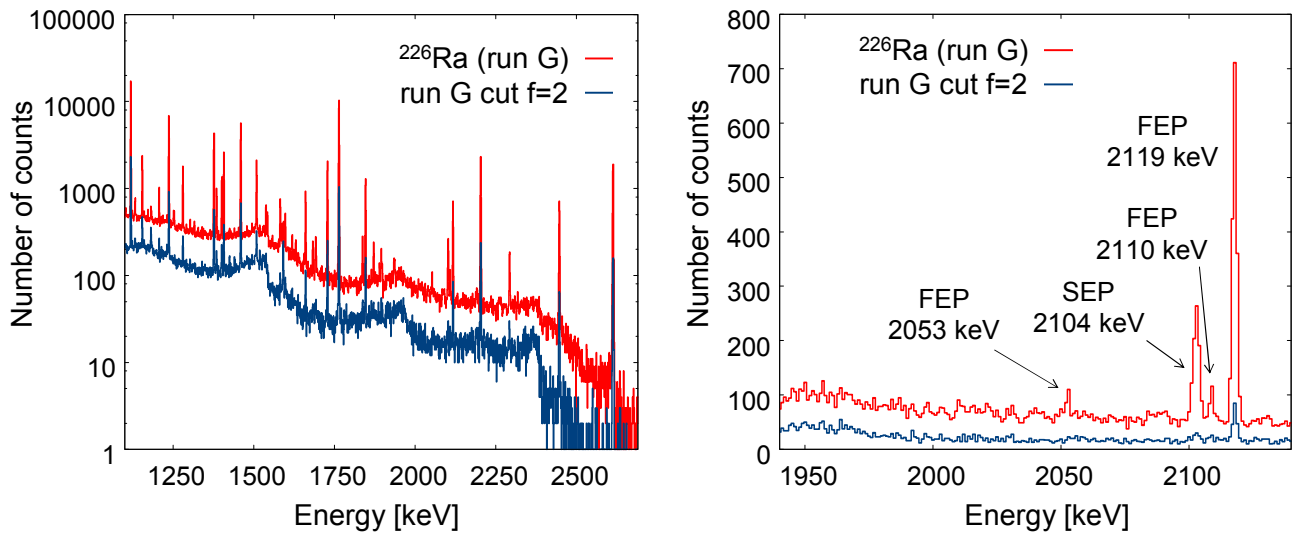


**Figure II-46** Left: Comparison of a  $^{226}\text{Ra}$  spectrum before and after the PSD cut with an acceptance factor  $f=2$ , in logarithmic scale. The 2.6 MeV peak from a  $^{228}\text{Th}$  background is also visible. Right: Zoom in linear scale on the energy region around  $^{76}\text{Ge}$   $Q_{\beta\beta}$ . Full energy peaks of  $^{214}\text{Bi}$  are highlighted, as well as the  $^{208}\text{Tl}$  SEP from background.

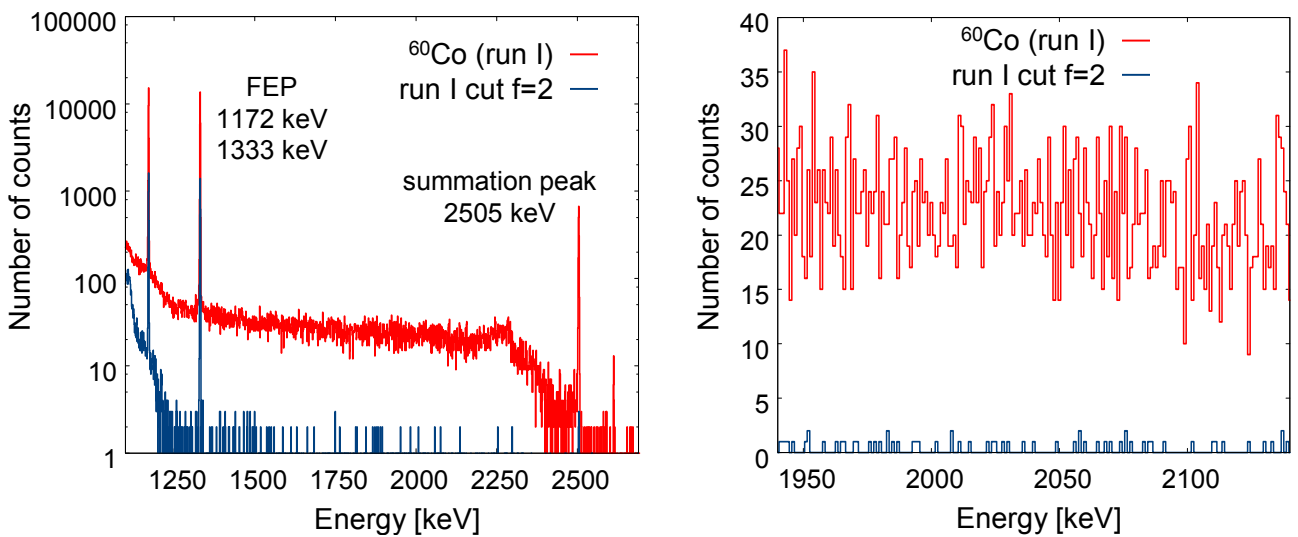


**Figure II-47** Left: Comparison of a  $^{60}\text{Co}$  spectrum before and after the PSD cut with an acceptance factor  $f=2$ , in logarithmic scale. Right: Zoom in linear scale on the energy region around  $^{76}\text{Ge}$   $Q_{\beta\beta}$ .

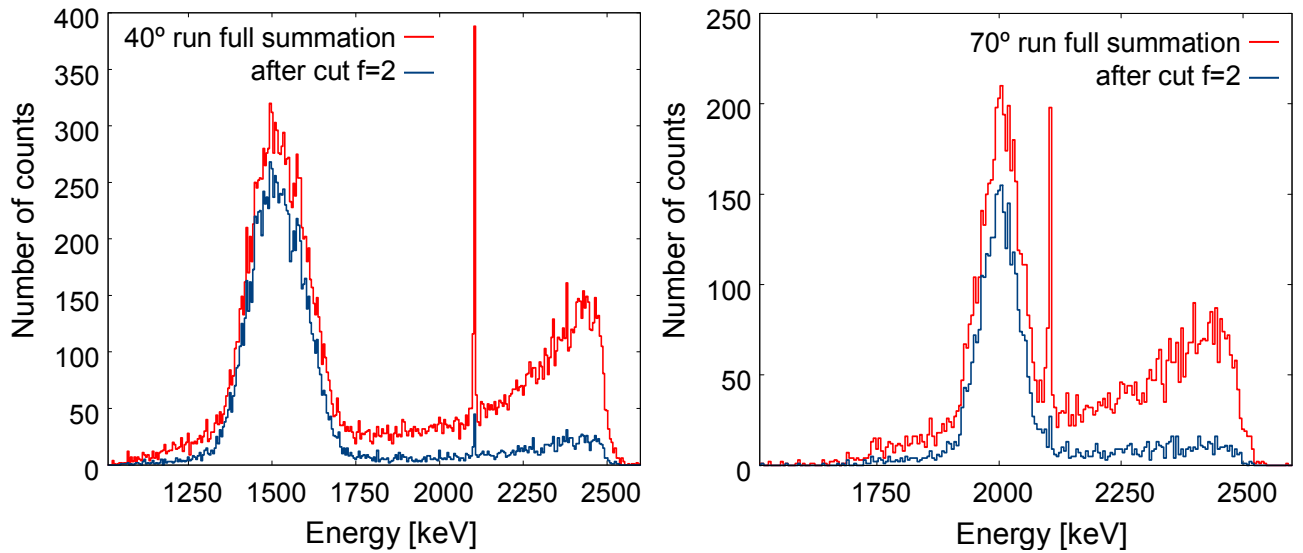


**Figure II-48** Left: Comparison of coincident full summation data set spectrum from the 40° Compton scattering run before and after the PSD cut with an acceptance factor  $f=2$ . Right: The same comparison from the 70° scattering run.

## 14. Feasibility of BEGe detectors for double beta decay experiments

The BEGe detector was studied due to its expected good pulse-shape discrimination performance. The presented experimental measurements have fully confirmed this expectation. Stability and charge collection investigations were also performed, and it was demonstrated that the BEGe detector performs flawlessly. In addition, the detector was found to have a very low electronic noise. Its energy resolution and low-energy threshold are very competitive compared to HPGe detectors of similar size and energy range (comparable to  $p$ -type point contact detectors [95]).

The stability issues of the DAQ setup used in the presented measurements were identified, and an improvement has already been achieved as was shown in Section 11.2.1. It is expected that a better isolation of the DAQ electronics from electromagnetic and microphonic interferences can further reduce the electronic gain and bandwidth variability. Nevertheless, the observed variability present in the DAQ system did not significantly affect the results of the PSD method developed in this work.

The PSD method presented here gives the unsegmented BEGe detector a background rejection power for  $^{76}\text{Ge}$   $0\nu\beta\beta$ -decay experiments, which is very competitive to highly segmented detectors [102,105]. The results are similar to those achieved with  $p$ -type point contact detectors [95], which share with BEGe the benefit of a small signal read-out electrode. The expected behaviour of a detector with such small electrode was the basis for the simplified model in Section 12. The presented discrimination technique behaves in accordance with the conclusions derived from that model. The simplicity of the PSD technique allowed by the special properties of small-electrode detectors makes it very robust, compared to PSD on coaxial detectors. The complicated weighing potentials of such detectors require much more complex discrimination techniques, which can be more vulnerable to systematic errors. The performance of the BEGe PSD is also not affected by the DAQ bandwidth, as was shown in Section 13.4. Furthermore, this method is based on a relatively

simple determination of the current-signal amplitude, which is neither expected to be significantly influenced by an increased electronic noise. The simplicity of this method permits all parameters of the PSD cut to be determined from the Compton continuum and the DEP data, so a simple measurement of  $^{228}\text{Th}$  is sufficient for a PSD calibration with satisfactory accuracy. Monte Carlo and electrical signal development simulations are not necessary to relate the DEP acceptance to an expected  $0\nu\beta\beta$ -decay acceptance.

At an expected 97.7% acceptance of SSE (a one sided cut at two sigma from the PSD parameter histogram), the PSD acceptance of DEP events was demonstrated at  $(89.2 \pm 0.9)\%$ . The survival probability of  $(20.6 \pm 3.4)\%$  and  $(40.2 \pm 1.6)\%$  was determined for events around  $^{76}\text{Ge}$   $Q_{\beta\beta}$  energy for  $^{226}\text{Ra}$  and  $^{228}\text{Th}$ , respectively. These two isotopes are the most significant external backgrounds for  $0\nu\beta\beta$ -decay in the GERDA experiment.

Potentially limiting backgrounds for  $^{76}\text{Ge}$   $0\nu\beta\beta$ -decay experiments are  $^{60}\text{Co}$  and  $^{68}\text{Ge}$ , cosmogenically produced inside the enriched HPGe crystals. A survival probability of  $(0.93 \pm 0.08)\%$  was measured for external  $^{60}\text{Co}$ , i.e. 99.1% of the events is removed. This isotope emits two angularly correlated  $\gamma$ -rays in cascade, at 1.17 MeV and 1.33 MeV, in addition to an electron with 317 keV endpoint energy [106]. For an intrinsic  $^{60}\text{Co}$ , a background event around the  $^{76}\text{Ge}$   $Q_{\beta\beta}$  can only be produced by simultaneous interaction of both  $\gamma$ -rays in addition to the electron absorption. The measured external  $^{60}\text{Co}$  events consist only of the summation of the two  $\gamma$ -ray interactions. By featuring an additional electron deposition besides the  $\gamma$ -ray summation, the intrinsic  $^{60}\text{Co}$  events at  $Q_{\beta\beta}$  energy are thus even less likely to be detected as an SSE than the summation events from the external  $^{60}\text{Co}$  source close to the detector. Consequently, with the presented PSD method using BEGe detectors, the intrinsic  $^{60}\text{Co}$  background can be reduced by more than two orders of magnitude.

Also, a high suppression can be expected for the second background source cosmogenically produced in Ge, the isotope  $^{68}\text{Ge}$ . This decays into  $^{68}\text{Ga}$ , which further undergoes  $\beta^+$  decay with a  $Q$ -value of 2.9 MeV. This happens with an emission of a positron with a maximum energy of 1.9 MeV [106]. To pose as a background for  $^{76}\text{Ge}$ , the absorption of the positron needs to be accompanied with an energy deposition from one or both of its annihilation photons. This results in a strong MSE signature. It is apparent that the BEGe PSD technique can efficiently suppress both of the most significant intrinsic HPGe detector backgrounds for double beta decay experiments.

At the beginning of this chapter, it was mentioned that using unsegmented  $p$ -type detectors in low-background experiments has the benefit of reducing potential backgrounds coming from signal contacts and read-out electronics. It was also noted, that unlike segmented or point contact detectors, the unsegmented BEGe is in standard commercial production. As a consequence of the results of the presented investigation and the favourable characteristics of BEGe detectors, the research and development for the second phase of the GERDA experiment now includes the BEGe technology alongside the detector segmentation.

# Appendix

## List of pulse shape measurements

### 1. BEGe

Measurement run	Preamp read-outs	Source	Source distance	Comment	Recorded events	Pile-up fraction
A	2	$^{228}\text{Th}$ 3.5 kBq	18.5 cm	complete shielding	$4 \cdot 10^6$	0.89%
B	2	$^{228}\text{Th}$ 3.5 kBq	18.5 cm	complete shielding	$9.9 \cdot 10^6$	0.88%
C	1	$^{228}\text{Th}$ 3.5 kBq	18.5 cm	complete shielding	$4.4 \cdot 10^6$	0.78%
D	1	$^{228}\text{Th}$ 3.5 kBq	18.5 cm	complete shielding	$15 \cdot 10^6$	0.68%
E	1	$^{228}\text{Th}$ 250 kBq	collimated beam at centre	complete shielding	$6.3 \cdot 10^6$	0.23%
F	1	$^{228}\text{Th}$ 250 kBq	collimated beam at edge	complete shielding	$7.9 \cdot 10^6$	0.24%
G	2	$^{226}\text{Ra}$ 37 kBq	70 cm	no shielding	$6 \cdot 10^6$	1.15%
H	2	$^{60}\text{Co}$ 2.4 kBq	0 cm	complete shielding, energy threshold 1.4 MeV	$3 \cdot 10^6$	20.5%
I	2	$^{60}\text{Co}$ 2.4 kBq	0 cm	no shielding, energy threshold 1.1 MeV	$0.16 \cdot 10^6$	19.9%

### 2. BEGe in coincidence with Dario

Scattering angle	Preamp read-outs	Source	Source distance	Distance BEGe - Dario	Recorded events	Pile-up fraction
40°	2	$^{228}\text{Th}$ 250 kBq	23.6 cm	86.2 cm	$3.4 \cdot 10^6$	19.9%
50°	2	$^{228}\text{Th}$ 250 kBq	23.6 cm	17.5 cm	$0.29 \cdot 10^6$	21.7%
70°	2	$^{228}\text{Th}$ 250 kBq	23.6 cm	68.2 cm	$0.89 \cdot 10^6$	20.7%



# Bibliography

- 1 K.T. Knöpfle, “Search for neutrinoless double-beta decay of Ge-76 with GERDA”, (2008) arXiv:0809.5207v1 [hep-ex]
- 2 P. Berghaus for the IceCube Collaboration, “IceCube: Status and First Results”, (2008) arXiv:0812.2883 [astro-ph]
- 3 P. A. Rapidis for the KM3NeT consortium, “KM3NeT: a large underwater neutrino telescope in the Mediterranean Sea”, (2008) arXiv:0803.2478v1 [astro-ph]
- 4 The KamLAND Collaboration, “Experimental investigation of geologically produced antineutrinos with KamLAND”, *Nature* 436 (2005) 499-503
- 5 W. Winter, “Neutrino Tomography – Learning About The Earth’s Interior Using The Propagation Of Neutrinos”, *Earth, Moon, and Planets* 99 (2006) 285–307
- 6 F. Reines, “The neutrino: from poltergeist to particle”, *Rev. Mod. Phys.* 68 (1996) 317-327
- 7 B.T. Cleveland et al., “Measurement of the Solar Electron Neutrino Flux with the Homestake Chlorine Detector”, *Astro. J.* 496 (1998) 505–526
- 8 J. Bahcall, “Solar Neutrinos: Where We Are”, (1997) arXiv:astro-ph/9702057v2
- 9 Y. Fukuda et. al, “Solar Neutrino Data Covering Solar Cycle 22”, *Phys. Rev. Lett.* 77 (1996) 1683-1686
- 10 M. Altmann et al. (GNO Collaboration), “GNO solar neutrino observations: results for GNO I”, *Phys. Lett. B* 490 (2000) 16-26
- 11 F. Kaether, “Datenanalyse des Sonnenneutrinoexperiments GALLEX”, Dissertation, University of Heidelberg (2007)
- 12 R. Becker-Szendy et al. (IMB Collaboration), “The Electron-neutrino and muon-neutrino content of the atmospheric flux”, *Phys. Rev. D* 46 (1992) 3720- 3724
- 13 M. Nakahata, Proceedings of the International Europhysics Conference on High Energy Physics, Jerusalem, August 19 – 26 (1997)
- 14 Y. Fukuda et. al, “Atmospheric  $\nu_{\mu}/\nu_e$  Ratio in the Multi-GeV Energy Range”, *Phys. Lett. B* 335 (1994) 237-245
- 15 B. Pontecorvo, *J.E.T.P.* 53 (1967), 1717-1725
- 16 SNO Collaboration, “Direct Evidence for Neutrino Flavor Transformation from Neutral-Current Interactions in the Sudbury Neutrino Observatory”, (2002) arXiv:nucl-ex/0204008v2
- 17 Y. Fukuda et. al (Super-Kamiokande Collaboration), “Evidence for Oscillation of Atmospheric Neutrinos”, *Phys. Rev. Lett.* 81 (1998) 1562-1567
- 18 M. H. Ahn et al. (K2K collaboration), “Measurement of Neutrino Oscillation by the K2K Experiment”, *Phys. Rev. D* 74 (2006) 072003
- 19 P. Adamson et al., “Measurement of neutrino oscillations with the MINOS detectors in the NuMI beam”, *Phys. Rev. Lett.* 101 (2008) 131802
- 20 The KamLAND Collaboration, “Measurement of neutrino oscillation with KamLAND: Evidence of spectral distortion”, *Phys. Rev. Lett.* 94 (2005) 081801

- 21 M. Apollonio et al., “Limits on Neutrino Oscillations from the CHOOZ Experiment”, *Phys. Lett. B* 466 (1999) 415
- 22 B. Kayser, “Neutrino properties”, lecture at International School on Astro-Particle Physics (ISAPP) 2006, Munich, Germany (23-31 May 2006) URL: <http://www.mppmu.mpg.de/ISAPP06/pages/curriculum/kayser.html>
- 23 J. Schechter and J.W.F. Valle, “Neutrinoless double- $\beta$  decay in  $SU(2)\times U(1)$  theories”, *Phys. Rev. D* 25 (1982) 2951 - 2954
- 24 S.Y.F. Chu, L.P. Ekström, R.B. Firestone, “WWW Table of Radioactive Isotopes”, database version 2/28/99 from URL <http://nucleardata.nuclear.lu.se/nucleardata/toi/>
- 25 O. Chkvorets, “Search for Double Beta Decay with HPGe Detectors at the Gran Sasso Underground Laboratory”, Dissertation, University of Heidelberg (2008)
- 26 R. Arnold et al., “Measurement of double beta decay of  $^{100}\text{Mo}$  to excited states in the NEMO 3 experiment”, *Nucl. Phys. A* 781 (2007) 209-226
- 27 SuperNEMO collaboration, “SuperNEMO  $^{150}\text{Nd}$  statement”, (2007) URL: [http://nemo.in2p3.fr/nemodocs/nemo/public/SuperNEMO\\_150Nd\\_statement.pdf](http://nemo.in2p3.fr/nemodocs/nemo/public/SuperNEMO_150Nd_statement.pdf)
- 28 C. Arnaboldi et al., “Results from the CUORICINO neutrinoless double beta decay experiment”, (2008) arXiv:0802.3439v1 [hep-ex]
- 29 R. Ardito et al., “CUORE: A Cryogenic Underground Observatory for Rare Events”, (2005) arXiv:hep-ex/0501010v1
- 30 C. Hall for the EXO Collaboration, “Searching for double beta decay with the Enriched Xenon Observatory”, *AIP Conf. Proc.* 870 (2006) 532-535
- 31 C. E. Aalseth et al. (IGEX Collaboration), “Recent results of IGEX  $^{76}\text{Ge}$  double-beta decay experiment”, *Phys. of Atomic Nuclei* 63 (2000) 1225
- 32 A. Balysh et al., “Heidelberg-Moscow  $\beta\beta$  experiment with  $^{76}\text{Ge}$ : Full setup with five detectors”, *Phys. Rev. D* 55 (1997) 54
- 33 H.V. Klapdor-Kleingrothaus, A. Dietz, L. Baudis et al., “Latest results from the Heidelberg-Moscow double beta decay experiment”, *Euro. Phys. J. A* 12 (2001) 147–154
- 34 S. M. Bilenky, A. Faessler, T. Gutsche et al., “Neutrinoless double beta-decay and neutrino mass hierarchies”, *Phys. Rev. D* 72 (2005) 053015
- 35 V. A. Rodin, A. Faessler, F. Simkovic et al., “Uncertainty in the  $0\nu\beta\beta$  decay nuclear matrix elements”, *Phys. Rev. C* 68 (2003) 044302
- 36 H.V. Klapdor-Kleingrothaus and I.V. Krivosheina, “The evidence for the observation of  $0\nu\beta\beta$  decay: the identification of  $0\nu\beta\beta$  events from the full spectra”, *Euro. Phys. J. A* 12 (2001) 147–154
- 37 S.R. Elliott, for the MAJORANA Collaboration, “The Majorana Project”, (2008) arXiv:0807.1741v1 [nucl-ex]
- 38 W. Maneschg, A. Merle, W. Rodejohann, “Statistical Analysis of future Neutrino Mass Experiments including Neutrino-less Double Beta Decay”, (2008) arXiv:0812.0479v1 [hep-ph]
- 39 G. Gilmore and J. Hemingway, “Practical gamma-ray spectrometry”, Wiley, New York (1995) ISBN 0-471-95150-1
- 40 G.F. Knoll, “Radiation detection and measurement”, second edition, Wiley, New York (1989) ISBN 0-471-81504-7

- 41 R.M. Castro, V.R. Vanin, N.L. Maidana, P.R. Pascholati, M.S. Dias, M.F. Koskinas, “Efficiency loss in HPGe detectors due to beta and gamma sum coincidence”, *Braz. J. Phys.* 35 (2005) 754-756
- 42 W. Miller, J.W. Motz and C. Cialella, “Thick Target Bremsstrahlung Spectra for 1.00-, 1.25-, and 1.40-MeV Electrons”, *Phys. Rev.* 96 (1954) 1344-1350
- 43 C. Jacoboni, F. Nava, C. Canali and G. Ottaviani, “Electron drift velocity and diffusivity in germanium”, *Phys. Rev. B* 24 (1981) 1014-1026
- 44 Z. He, “Review of the Shockley–Ramo theorem and its application in semiconductor gamma-ray detectors”, *Nucl. Inst. Meth. A* 463 (2001) 250–267
- 45 S. Schönert for the GERDA collaboration, “The GERmanium Detector Array (Gerda) for the search of neutrinoless  $\beta\beta$  decays of  $^{76}\text{Ge}$  at LNGS”, *Nucl. Phys. B (Proc. Suppl.)* 145 (2005) 242–245
- 46 H. Simgen, G. Zuzel, “Analysis of the Rn-222 concentration in argon and a purification technique for gaseous and liquid argon”, *Appl. Radiat. Isot.* (2009), doi:10.1016/j.apradiso.2009.01.058
- 47 W. Maneschg, M. Laubenstein, D. Budjáš, W. Hampel, G. Heusser, K.T. Knöpfle, B. Schwingenheuer, H. Simgen, “Measurements of extremely low radioactivity levels in stainless steel for GERDA”, *Nucl. Inst. Meth. A* 593 (2008) 448-453
- 48 I. Abt et al. (GERDA collaboration), “GERDA: The GERmanium Detector Array for the search of neutrinoless decays of  $^{76}\text{Ge}$  at LNGS”, Proposal to LNGS P38/04 (2004) arXiv:hep-ex/0404039
- 49 G. Heusser, “Low-radioactivity background techniques”, *Ann. Rev. Nucl. Part. Sci.* 45 (1995) 543
- 50 I. Abt et al., “Characterization of the first true coaxial 18-fold segmented n-type prototype detector for the GERDA project”, *Nucl. Instr. Methods A* 577 (2007) 574 – 584
- 51 P. Peiffer, “Liquid argon as active shielding and coolant for bare germanium detectors: A novel background suppression method for the Gerda  $0\nu\beta\beta$  experiment”, Dissertation, University of Heidelberg (2007)
- 52 D. Budjáš et al., “Gamma-ray spectrometry of ultra low levels of radioactivity within the material screening program for the GERDA experiment”, *Appl. Radiat. Isot.* (2009), doi:10.1016/j.apradiso.2009.01.019
- 53 A. Caldwell, J. Janicsko-Csathy, V. Kornoukhov, “Report on reduction of dep-GeO<sub>2</sub> and zone-refinement at PPM Pure Metals, Summary of 2007 activities”, GERDA Scientific/Technical Report GSTR-08-001 (2008)
- 54 H. Simgen, G. Heusser, G. Zuzel, “Highly sensitive measurements of radioactive noble gas nuclides in the Borexino solar neutrino experiment”, *Appl. Rad. Isot.* 61 (2004) 213-217
- 55 W. Rau, G. Heusser, “ $^{222}\text{Rn}$  emanation measurements at extremely low activities”, *Appl. Rad. Isot.* 53 (2000) 371-375
- 56 S. Nisi and A. di Vacri, “Determination of K, Pb, Th and U contamination in SI, PE, PEN, PET with ICPMS”, GERDA Scientific/Technical Report GSTR-06-017 (2006)
- 57 H. Neder, G. Heusser, M. Laubenstein, “Low level g-ray germanium-spectrometer to measure very low primordial radionuclide concentrations”, *Appl. Rad. Isot.* 53 (2000) 191-195

- 58 D. Budjáš, M. Heisel, M. Hult, A. Klimenko, M. Laubenstein, P. Lindahl, H. Simgen, A. Smolnikov, C. Tomei, S. Vasiliev, “A Comparison of Low-level Laboratories within GERDA”, *AIP Conf. Proc.* 897 (2007) 26-31
- 59 B. Philhour et al., “Simulations of pulse shape discrimination (PSD) techniques for background reduction in germanium detectors”, *Nucl. Instr. Methods A* 403 (1998) 136-150
- 60 Th. Kröll et al., “Analysis of simulated and measured pulse shapes of closed-ended HPGe detectors”, *Nucl. Instr. Methods A* 371 (1996) 489-496
- 61 J. Hellmig and H.V. Klapdor-Kleingrothaus, “Identification of single-site events in germanium detectors by digital pulse shape analysis”, *Nucl. Instrum. Meth. A* 455 (2000) 638
- 62 B. Majorovits, H.V. Klapdor-Kleingrothaus, “Digital pulseshape analysis by neural networks for the Heidelberg-Moscow-double-beta decay experiment”, *Eur. Phys. J. A* 6 (1999) 463
- 63 D. Gonzalez et al., “Pulse shape discrimination in the IGEX experiment”, *Nucl. Instrum. Meth. A* 515 (2003) 634
- 64 C.E. Aalseth, “Germanium spectrometer pulse shape discrimination for germanium 76 double beta decay”, UMI-30-06000
- 65 S.R. Elliott et al., “Pulse shape analysis in segmented detectors as a technique for background reduction in Ge double-beta decay experiments”, *Nucl. Instrum. Meth. A* 558 (2006) 504
- 66 W. Maneschg, “Low-Level-Gammaspektroskopie im Rahmen des GERDA-Experiments zur Suche nach dem neutrinolosen Doppel-Betazerfall in  $^{76}\text{Ge}$ ”, Diploma Thesis, University of Heidelberg (2007)
- 67 D. Budjáš et al., “Highly sensitive gamma-spectrometers of GERDA for material screening: Part 2”, Proceedings of the XIV International Baksan School "Particles and Cosmology-2007". INR RAS, Moscow (2008) ISBN 978-5-94274-055-9, pp. 233-238; arXiv:0812.0768v1 [physics.ins-det]
- 68 G. Heusser, “Studies of  $\gamma$ -ray background with a low level germanium spectrometer”, *Nucl. Instr. Meth. B* 58 (1991) 79-84
- 69 D. Budjáš et al., “Highly sensitive gamma-spectrometers of GERDA for material screening: Part I”, Proceedings of the XIV International Baksan School "Particles and Cosmology-2007". INR RAS, Moscow (2008) ISBN 978-5-94274-055-9, pp. 228-232; arXiv:0812.0723v1 [physics.ins-det]
- 70 M. Bauer et al., “MaGe: a Monte Carlo framework for the Gerda and Majorana double beta decay experiments” *J. Phys. Conference Series* 39 (2006) 362
- 71 Y.-D. Chan et al., “MaGe - a Geant4-based Monte Carlo framework for low-background experiments”, (2008) arXiv:0802.0860v1 [nucl-ex]
- 72 S. Agostinelli et al., “Geant4 - a simulation toolkit”, *Nucl. Instr. Meth. A* 506 (2003) 250-303
- 73 K. Amako et al., “Comparison of Geant4 electromagnetic physics models against the NIST reference data”, *IEEE Trans. Nucl. Scie.* 52 (2005) 910-917
- 74 E. Poon and F. Verhaegen, “Accuracy of the photon and electron physics in Geant4 for radiotherapy applications”, *Med. Phys.* 32 (2005) 1696-1711
- 75 D. Budjáš and L. Pandola, “Study of the  $\gamma$ -ray branching ratios of nuclear decays in Geant4”, GERDA Scientific/Technical Report GSTR-07-010 v2 (2007)
- 76 T. Vidmar et al., “An intercomparison of Monte Carlo codes used in gamma-ray spectrometry”, *Appl. Rad. Isot.* 66 (2008) 764-768

- 77 F. Salvat, J. M. Fernandez-Varea, J. Sempau, “PENELOPE-2006, A Code System for Monte Carlo Simulation of Electron and Photon Transport”, OECD ISBN 92-64-02301-1 (2006)
- 78 A. F. Bielajew, H. Hirayama, W. R. Nelson and D. W. O. Rogers, “History, overview and recent improvements of EGS4”, Report NRCC/PIRS-0436 (June 1994)
- 79 M.M. Bé, R. Helmer, V. Chisté, “The NUCLÉIDE database for decay data and the International Decay Data Evaluation Project”, *Journal of Nuclear Science and Technology*, Supplement 2 (August 2002) 481
- 80 R.G. Helmer, J.C. Hardy, V.E. Jacob, M. Sanchez-Vega, R.G. Neilson, J. Nelson, “The use of Monte Carlo calculations in the determination of a Ge detector efficiency curve”, *Nucl. Instr. Meth. A* 511 (2003) 360-381
- 81 M. Hissmann, “Simulationen des Heidelberger Germanium-Spektrometers mit Geant4”, Diploma Thesis, University of Heidelberg (2001)
- 82 P.N. Johnston, M. Hult, J. Gasparro, “Cascade summing effects in close geometry gamma-ray spectrometry”, *Appl. Rad. Isot.* 64 (2006) 1323-1328
- 83 J. Gasparro, M. Hult, P.N. Johnston, H. Tagziria, “Monte Carlo modelling of germanium crystals that are tilted and have rounded front edges”, *Nucl. Instr. Meth. A* 594 (2008) 196-201
- 84 S. Hurtado, M. García-León, R. García-Tenorio, “Geant4 code for simulation of a germanium gamma-ray detector and its application to efficiency calibration”, *Nucl. Instr. Meth. A* 518 (2004) 764-774
- 85 F. Ardellier et al., “Double Chooz, A Search for the Neutrino Mixing Angle theta-13”, Proposal (Proposal, 2006) arXiv:hep-ex/0606025v4
- 86 A. V. Harms, C. Gilligan, A. Arinc, S. Collins, S. Jerome, L. Johansson, D. MacMahon and A. Pearce, “Environmental radioactivity comparison exercise 2005”, NPL Report **DQL-RN 015** (June 2006) ISSN 1744-0629
- 87 A. V. Harms and C. Gilligan, “Environmental radioactivity proficiency test exercise 2007”, NPL Report **IR 8** (April 2008) ISSN 1754-2952
- 88 A. Shakhshiro, U. Sansone, A. Trinkl, M. Makarewicz, C. Yonezawa, C.K. Kim, G. Kis-Benedek, T. Benesch, R. Schorn, “Report on the IAEA-CU-2006-03 world-wide open proficiency test on the determination of gamma emitting radionuclides”, IAEA Report IAEA/AL/171 (May 2007)
- 89 D. Budjáš, M. Heisel, W. Maneschg and H. Simgen, “Optimisation of the MC-model of a p-type Ge-spectrometer for the purpose of efficiency determination”, *Appl. Radiat. Isot.* (2009), doi:10.1016/j.apradiso.2009.01.015
- 90 C. Buck, F.X. Hartmann, T. Lasserre, D. Motta, S. Schönert, U. Schwan and H. Simgen (for the Lens Collaboration), “The LENS Project”, *Nucl. Phys. B (Proc. Suppl.)* 118 (2003) 450
- 91 P. Peiffer, T. Pollmann, S. Schönert, A. Smolnikov and S. Vasiliev, “Pulse shape analysis of liquid argon scintillation signals for radioactive background identification and suppression”, *JINST* 3 (2008) P08007
- 92 K. Vetter, “Recent Developments in the Fabrication and Operation of Germanium Detectors”, *Annu. Rev. Nucl. Part. Sci.* 57 (2007) 363-404
- 93 A. Balysh et al. “Background recognition in Ge detectors by pulse shape analysis”, *Nucl. Instrum. Meth. A* 332 (1993) 107-112
- 94 P. N. Luke, F. S. Goulding, N. W. Madden and R. H. Pehl, “Low capacitance large volume shaped-field germanium detector”, *IEEE Trans. Nucl. Sci.* 36 (1989) 926-930

- 95 P.S. Barbeau, J.I. Collar and O. Tench, “Large-mass ultra-low noise germanium detectors: performance and applications in neutrino and astroparticle physics”, *JCAP* 09 (2007) 009
- 96 S. Schönert, J. Verplancke, private communication
- 97 Canberra Semiconductor NV, Lammerdries 25, B-2430 Olen, Belgium
- 98 D. Budjáš, M. Barnabé Heider, O. Chkvorets, S. Schönert, N. Khanbekov, “Pulse Shape Analysis with a Broad-Energy Germanium Detector for the GERDA experiment”, arXiv:0812.1735 [nucl-ex]
- 99 H. V. Klapdor-Kleingrothaus et al., “GENIUS-TF: a test facility for the GENIUS project”, *Nucl. Instr. and Meth. A* 481 (2002) 149-159
- 100 T. Kihm, private communication
- 101 H. V. Klapdor-Kleingrothaus, I. V. Krivosheina, I. V. Titkova, “Theoretical investigation of the dependence of double beta decay tracks in a Ge detector on particle and nuclear physics parameters and separation from gamma ray events”, *Phys. Rev. D* 73, 013010 (2002)
- 102 I. Abt, A. Caldwell, K. Kröniger, J. Liu, X. Liu, B. Majorovits, “Identification of photons in double beta-decay experiments using segmented germanium detectors—Studies with a GERDA phase II prototype detector”, *Nucl. Instrum. Meth. A* 583 (2007) 332–340
- 103 I. Abt, A. Caldwell, K. Kröniger, J. Liu, X. Liu, B. Majorovits, “Test of pulse shape analysis using single Compton scattering events”, *Eur. Phys. J. C* 54 (2008) 425–433
- 104 J. Hellmig, H. V. Klapdor-Kleingrothaus, F. Petry, “Background identification by digital pulse shape analysis”, *Nucl. Phys. B* 48 (1996) 254–256
- 105 I. Abt, A. Caldwell, K. Kröniger, J. Liu, X. Liu, B. Majorovits, “Pulse shapes from electron and photon induced events in segmented high-purity germanium detectors”, *Eur. Phys. J. C* 52 (2007) 19–27
- 106 International Decay Data Evaluation Project, Nucléide database version 16th February 2009, from URL: [http://www.nucleide.org/DDEP\\_WG/DDEPdata.htm](http://www.nucleide.org/DDEP_WG/DDEPdata.htm)

## Acknowledgements

First of all I would like to thank Prof. Wolfgang Hampel, Stefan Schönert and Hardy Simgen, for their guidance and countless amount of advice. Without them this thesis would never exist.

Parts of this thesis resulted from collaborative work, and here I would like to extend my thanks for fruitful teamwork to my colleagues. This includes Hardy, Gerd Heusser, Mark Heisel and Werner Maneschg, comprising the  $\gamma$ -ray screening team, and the "BEGe team", which included Stefan, Oleg Chkvorets, Marik Barnabé Heider and Nikita Khanbekov. Thanks to Grzegorz Zuzel for being always helpful when it was needed, to Florian Kaether for a lot of advice concerning logical problems and for proof reading, and to Alex Merle for helping me with the theoretical side of physics and for being the most outgoing theoretician that I know. Many thanks to Ute Schwan, Herbert Strecker, Michael Reisfelder, Reinhard Hofacker, Erhard Burkert, Thomas Kihm, Brigitte Villaumie and Anja Berneiser for their unlimited support. I am also thankful to Luciano Pandola for a lot of help with MaGe, and to Anatoly Smolnikov for many advice and for sharing with me often the lab equipment. Special thanks to Sergey Vasiliev for his first aid. I would like to thank also my colleagues, with whom I worked together on projects which finally did not make it into this dissertation, nevertheless I learned a lot from them: Andrey Vasenko, Alessio D'Andragora, Francesca Zocca, Alberto Pullia, Stefano Riboldi and Carla Cattadori.

Special thanks belongs to all my friends from the International Max-Planck School for Astronomy and Cosmic Physics, with whom I had a lot of great time during the years in Heidelberg. Especially, thanks to Christian Fendt for taking care of us, to Giulia and Steve for organizing all the fun, to Jamie for many good discussions concerning life matters, and to Marie-Helene for the great parties! I owe a big *Ďakujem* to my family for their remote but everlasting support, and un grand *Merci* to Marik for helping me keep my sanity during the long weeks of writing despite having to write her own thesis. It was more than three years since I started with this work and I can't mention all the many people that directly or indirectly helped me during this time, but I would like to express my thanks to all of them.